Exploiting the Interplay of Acoustic Waves and Fluid Motion for Particle Manipulation

by

Yuyang Gu

Department of Mechanical Engineering and Materials Science
Duke University

Date:_____
Approved:

_____
Tony Jun Huang, Advisor

_____
Steven A. Cummer

_____
Pei Zhong

_____
Gowthami M. Arepally

Dissertation submitted in partial fulfillment of
the requirements for the degree of Doctor
of Philosophy, in the Department of
Mechanical Engineering and Materials Science in the Graduate School
of Duke University

[2021]

ABSTRACT

Exploiting the Interplay of Acoustic Waves and Fluid Motion for Particle Manipulation

by

Yuyang Gu

Department of Mechanical Engineering and Materials Science
Duke University

Date:_____
Approved:

_____
Tony Jun Huang, Advisor

_____
Steven A. Cummer

_____
Pei Zhong

_____
Gowthami M. Arepally

An abstract of a dissertation submitted in partial
fulfillment of the requirements for the degree
of Doctor of Philosophy in the Department of
Mechanical Engineering and Materials Science in the Graduate School of
Duke University

[2021]

Copyright by
Yuyang Gu
[2021]

Abstract

Acoustofluidics is an emerging research field that combines both acoustics and fluid dynamics. With acoustic tweezers technique being developed for years, it is featured for its contactless, noninvasive, and biocompatibility which makes the method suitable for various applications in the field of biology, material sciences, and chemistry. Especially when handling small objects, e.g., cells, nanoparticles, C. elegans, and zebrafish larvae, the native environment involved is mainly liquid. During the acoustic propagation inside the liquid, fluid motion will also be initiated and will influence the object movement in addition to the acoustic radiation forces. This brings up the multidisciplinary study combining the acoustic wave and fluid motion for object manipulation within liquids. This technical development has revealed huge potential for applying acoustofluidic studies into different applications. However, there are still several technical bottlenecks that must be overcome for acoustofluidic technology to provide maximum impact. For example, cell patterning using standing acoustic waves commonly has the regular grid-like shape and sees the fluid motion as an unwanted side effect without an effective way to minimize it. The current target particle size that can be controlled using acoustics is between ~mm to μm, thus hindering the exploration of nanoscale objects. In this dissertation, I explored the combined effect of acoustics and fluid dynamics, and validated that the interplay of both effects can derive new research insights and can be applied to

particles with a smaller size range (i.e., nanometer). Specifically, I studied the synergetic effect of acoustics and flow in three classic fluid systems: bulk fluids, droplets, and continuous flow.

For bulk fluids, we designed an acoustofluidic holography platform that can initiate and utilize fluid motion with arbitrary designed acoustic fields. With the design and implementation of the holographic acoustic lens, our method can pattern cells into an arbitrary shape that can potentially benefit tissue engineering or cell mechanics studies. Besides patterning, we also demonstrated that, with the same experimental configuration, we can utilize vortex acoustic streaming to achieve different functions, e.g., particle rotation, concentration, and separation.

For droplets, we observed a new physics phenomenon which can drive the spin of a liquid droplet using surface acoustic wave. With this external angular momentum and Stokes drift effect, we found the nanoparticles can be rapidly concentrated or differentially concentrated in one spinning droplet. Furthermore, we demonstrated that the single spinning droplet can serve as one unit that possesses a specific function and we can assemble the units for a more flexible manipulation function. We built a dual droplet acoustofluidic centrifuge system that can achieve nanoparticle separation and transport and utilized the platform for exosome subgroup separation.

For continuous flow, as acoustic separation technique has been developed for years, we have explored two directions that may be utilized for small animal blood

apheresis study. One direction is the high-throughput platelet separation using a plastic device. This method significantly increased the throughput and moved one step towards clinical usage. Another direction is building the integrated system for plasma separation. Built around the surface acoustic wave separator, we assembled the fluid driving unit, temperature control unit, and separation unit into a prototype-like system. We then performed the proof-of-concept experiment to identify the feasibility of applying the acoustofluidic separation method to small animal models (i.e., mice).

Contents

Abstract iv

List of Tables x

List of Figures xi

Acknowledgements xv

Chapter 1: Introduction 1

1.1 A brief history of acoustofluidics 1

1.2 Basic theory of acoustofluidics 4

1.3 Acoustic holography 7

1.4 Acoustic droplet system 11

1.5 Acoustic separation in continuous flow 15

1.6 Dissertation outline 18

Chapter 2: Acoustofluidic holography for particle manipulation 20

2.1 Motivation 20

2.2 Materials and methods 27

2.2.1 Experimental setup and materials 27

2.2.2 Cell preparation 30

2.3 Theoretical model and working mechanism 30

2.3.1 Acoustic hologram 30

2.3.2 Fluid dynamics induced by acoustic waves 37

2.3.3 Particle force analysis 43

2.3.3.1 Acoustic radiation force of standing wave field 43
2.3.3.2 Acoustic radiation force of travelling wave field 44
2.3.3.3 Spherical isotropic scattering 45
2.3.3.4 Hydrodynamic force 46
2.4 Cell patterning using acoustofluidic holography 49
2.4.1 Two-dimensional cell pattern 49
2.4.2 Three-dimensional layer-by-layer cell pattern 59
2.5 Other functions using acoustofluidic holography 69
2.5.1 Single particle rotation 69
2.5.2 Particle concentration and separation 71
2.6 Discussion and future work 78
Chapter 3: Acoustofluidic centrifuge for nanoparticle enrichment and separation 82
3.1 Motivation 82
3.2 Materials and methods 87
3.2.1 Device design, fabrication and operation 87
3.2.2 Droplet generation and sample preparation. 88
3.2.3 Small EV preparation procedure 89
3.2.4 Image acquisition and analysis 90
3.3 Theoretical model and working mechanism 90
3.3.1 Droplet spinning motion 90
3.3.2 Particle motion in spinning system 100
3.4 Single droplet spinning 117

3.5 Dual droplet spinning 122

3.6 Discussion and future work 132

Chapter 4: Acoustofluidic blood components separation for apheresis 136

4.1 Motivation 136

4.2 Materials and methods 141

4.2.1 Platelet separation device 141

4.2.2 Plasma separation device 143

4.3 Theoretical model and working mechanism 145

4.4 Platelet separation 148

4.5 Plasma separation 158

4.6 Discussion and future work 164

Chapter 5: Conclusion 168

5.1 Summary 168

5.2 Future works 171

Bibliography 176

Biography 193

List of Tables

Table 3.1: Detailed parameters for numerical simulations. 113

Table 3.2: Force characterization for particle motion in a spinning droplet. 117

List of Figures

Figure 1.1: The schematic showing the target outputs that can be obtained using the acoustofluidic technology. 4

Figure 1. 2: Schematic showing two classic acoustic holography configurations. 10

Figure 1. 3: Schematic of the SAW droplet interaction system. 13

Figure 1. 4: General illustration of acoustic based particle separation in continuous flow. 18

Figure 2. 1: Schematic of the configuration and mechanism of cell/particle patterning *via* acoustofluidic holography.. 27

Figure 2. 2: Illustration of the 3D printed container. 29

Figure 2. 3: Theoretical calculated liquid-air interface deformation and experimental realization. 33

Figure 2. 4: The function of the interface deformation. 34

Figure 2. 5: Acoustic field and flow field within the deformed space.. 38

Figure 2. 6: Force analysis of immersed particle. 48

Figure 2. 7: Acoustic radiation force and drag force analysis. 48

Figure 2. 8: Schematic showing the differences in the experimental setups and underlying mechanisms for patterning particles. 52

Figure 2. 9: Cell and particle patterning *via* acoustofluidic holography. 53

Figure 2. 10: The feature width comparison. 56

Figure 2. 11: Cell patterning in the petri dish. 57

Figure 2. 12: Disk shape cell pattern using acoustofluidic holography. 58

Figure 2. 13: Binary acoustofluidic holography for high-resolution cell patterning. 59

Figure 2. 14: Operating mechanism of the 3D acoustofluidic virtual scaffolds (AVS). 61

Figure 2. 15: Binary acoustic lens design and characterization. 64

Figure 2. 16: Two-layer prescribed, arbitrary cell patterning *via* AVS. 66

Figure 2. 17: Single particle rotation *via* acoustofluidic holography..... 70

Figure 2. 18: Particle rotation speed analysis. 71

Figure 2. 19: The principle of the double phase holography calculation. 74

Figure 2. 20: Particle/cell concentration *via* acoustofluidic holography. 75

Figure 2. 21: Particle/cell separation *via* acoustofluidic holography..... 76

Figure 2. 22: Particle separation using acoustofluidic holography. 77

Figure 2. 23: 3D flow field characterization..... 77

Figure 3. 1: Operating mechanism of the acoustofluidic centrifuge platform……..……. 87

Figure 3. 2: Schematic showing the side view of the droplet spinning motion. 93

Figure 3. 3: Characterization of droplet spin and particle movement in the acoustofluidic centrifuge device.. 93

Figure 3. 4: The influence of the acoustic frequency on the droplet spin speed in an acoustofluidic centrifuge..... 95

Figure 3. 5: The influence of the acoustic power on droplet spin in an acoustofluidic centrifuge. 96

Figure 3. 6: Photos (left) and outline comparisons (right) between the droplet (blue circle) and a fitted line (red line) for different droplet spin modes. 97

Figure 3. 7: The droplet contact angle and spinning speed with a SU-8 ring as container. droplet volume. 99

Figure 3. 8: The droplet deformation ratio characterization. 100

Figure 3. 9: Microparticle trajectory inside a spinning droplet. 102

Figure 3. 10: Characterization of the internal streaming and shear rate. 104

Figure 3. 11: Experimentally observed particle trajectories within the droplet in an acoustofluidic centrifuge. 105

Figure 3. 12: Particle trajectory changing with the input voltage increasing. 106

Figure 3. 13: Particle motion comparison between non-spinning and spinning droplets. 108

Figure 3. 14: Simulation result showing the particle concentration due to the droplet spin and periodic boundary deformation. 109

Figure 3. 15: Rapid nanoparticle enrichment *via* acoustofluidic centrifuge. 119

Figure 3. 16: Demonstration of the DNA molecules concentration for fluorescence signal amplification. 121

Figure 3. 17: Differential nanoparticle concentration *via* acoustofluidic centrifuge. 122

Figure 3. 18: Schematic of the procedure of the particle transport and separation in dual-droplet acoustofluidic centrifuge. 127

Figure 3. 19: Particle separation and transport *via* a dual-droplet acoustofluidic centrifuge. 128

Figure 3. 20: The separation and enrichment of particles with diameters of 500 nm and 970 nm *via* a dual-droplet acoustofluidic centrifuge. 129

Figure 3. 21: Exosome subpopulation separation and transport in an acoustofluidic centrifuge. 132

Figure 4. 1: Schematic of the platelet separation device 144

Figure 4. 2: Acoustic field characterization. 145

Figure 4. 3: Acoustic radiation force and particle trajectory. 150

Figure 4. 4: Platelet separation performance. 152

Figure 4. 5: The flow cytometry results. 153

Figure 4. 6: Device performance under different parameters. 155

Figure 4. 7: Evaluation of the quality of the isolated platelets by our acoustic platelet separation technique and the centrifugation. 156

Figure 4. 8: A photograph of acoutofluidic apheresis chip. 160

Figure 4. 9: Separation of blood cells and plasma by acoustophoresis. 163

Figure 4. 10: Plasma separation with the acoustofluidic apheresis system. 164

Acknowledgements

First of all, I would like to express my deepest gratitude to my Ph.D. advisor, Prof. Tony Jun Huang, for his constant supervision and support. His guidance and passion make my Ph.D. journey such a precious experience. He influenced and inspired me in almost every aspect of my life.

I would like to thank my dissertation committee, Prof. Steven A. Cummer, Prof. Pei Zhong, Prof. Gowthami M. Arepally for their valuable suggestions on my dissertation work in so many ways. I would also like to acknowledge Prof. Luke P. Lee, Prof. Yoel Sadovsky, Prof. Yun Jing, Prof. David T.W. Wong, Prof. Jean Kwun, Prof. Eileen T. Chambers, Prof. Xiasheng Guo, and Dr. John D.H. Mai for their insightful suggestions and strong support to my research.

My dissertation work was done in collaborations with so many great people within and outside of Acoustofluidic research group. My sincere thanks to Dr. Po-Hsun Huang, Dr. Zhenhua Tian, Dr. Zhangming Mao, Dr. Mengxi Wu, Dr. Yuchao Chen, Dr. Feng Guo, Dr. Adem Ozcelik, Dr. Peiran Zhang, Dr. Hunter Bachman, Dr. Nanjing Hao, Dr. Chen Shen, Dr. Junfei Li, Dr. Yangbo Xie, Dr. Yingshi Ouyang, Hai Fu, Shujie Yang, Zeyu Wang, Shuaixiang Zhao, Jinxin Zhang, Haodong Zhu, Geonsoo Jin, Jianping Xia, Zhehan Ma, Kaichun Yang, Ruoyu Zhong, Ty D. Naquin, Ryan Becker, Joseph T. Rich, Ye

He, and Defei Liao for their help in different ways, and special thanks to Chuyi Chen and Joseph Rufo for their immense support to each of my project.

I want to thank my Department--Mechanical Engineering and Materials Science for offering me this precious opportunity to work and study here. I also want to thank various funding agencies for my research.

Lastly, I would like to thank my beloved family for their love, caring, and support that has made this dissertation possible. I would also like to thank my friends who have always been there for me.

Chapter 1: Introduction

1.1 A brief history of acoustofluidics

Acoustic waves can propagate through a certain medium (e.g., gas, liquid, and solid) by means of continuous compression and decompression(Wikipedia contributors, 2020). Acoustofluidics, as a rapidly growing research field, generally can be referred to as the phenomenon with the interaction between acoustic waves and fluid (e.g., gas, liquid). Broadly, the acoustofluidic technique involves various topics spanning from audio research to ultrasonic therapy. As life science research gradually emerging, acoustofluidic method development becomes more focused on the interaction between acoustics and liquid where most of the bio-related particles/fluids exist (Figure 1.1). With the success of optical tweezers that exploded the development of tweezer-like technology for bioparticle handling, acoustic tweezers featuring for its compact setup, larger force, extensive working environment, started to bring a lot of research interests(Ozcelik et al., 2018).

The early development of acoustic tweezers initiated the method of trapping the particles using standing wave, this classic mechanism can provide stable trapping force and be applied to the particles with different properties(M Baudoin & Thomas, 2020; King, 1934). Then, with the fabrication technique development, researchers started to scale down the device configuration in order to study the small objects that possess deeper implications in the field of biology, materials, and chemistry. This progress brings up the on-chip manipulation that can be applied to numerous practical applications for life

science(Ding et al., 2012). The most common usage of this technique is to provide a sample in sample out a workflow that can narrow down the focus to the target of interest, for example, cell separation, pattern, sorting. With the development of this pathway, researchers have invented different setups that can provide ideal resolution and flexibility.

On the other hand, the classic standing wave method usually precludes any selectivity in terms of the trapping, which may confine the usage when a specific target is embedded in a relatively large and complex environment(M Baudoin & Thomas, 2020). The intuitive method for this purpose is to mimic the optical tweezer and utilize the focused beam. However, it was found that the majority of the particles of interest have denser and stiffer property compare to the surrounding fluid, which makes the particles pushing away from the focused area and can only be trapped at the pressure nodes(Gor'kov, 1962). Thus, researchers developed an acoustic vortex beam, which makes the wave propagating along a helical path and spinning around a phase singularity(Baresch et al., 2016; M Baudoin & Thomas, 2020). The acoustic vortex beam has a minimum pressure intensity in the middle which can be utilized to trap single particles. With this method development, it can be applied to single object manipulation in a different range of area, from large mid-air space to a miniature microfluidic channel, to even inside the body of animals(Drinkwater, 2016; Ghanem et al., 2020; Marzo et al., 2015b). Meanwhile, researchers have also devoted to the design of the active transducer

array which can provide higher flexibility during the manipulation and achieve real-time 2D/3D manipulation(Ghanem et al., 2020; Marzo et al., 2015b; Marzo & Drinkwater, 2018; Y. Yang et al., 2021). This specific direction makes acoustic manipulation a tool that can provide certain functions to the target without the need of a specific sample out.

Furthermore, with the development of microfluidic techniques and the increasing interest in Point-of-Care and health monitoring, researchers also started to investigate the workflow of generating digital readout (image, electric signal, quantitative numbers) using the acoustofluidic method. This can provide both the qualitative and quantitative analysis that towards the statistical study and trend evaluation for cells, organism, small animal or human being(Ahmed et al., 2016; C. Chen et al., 2021; J. H. Kang et al., 2019). While more and more techniques are getting crossed-over (imaging methods, computer sciences, material science, chemistry, biology), the initial concept of this workflow can be traced back to acoustic imaging and acoustic sensing technique. As object manipulation is barely involved, these methods can directly provide the message through acoustic waves, and with the progress of the beamforming, nanofabrication, machine learning, and computer vision, the higher spatial resolution, higher sensitivity, and more complex information can be derived. And the acoustic manipulation can also be combined with these workflows with specific advantages, e.g., contactless alignment, multi-view imaging, sample pre-handling.

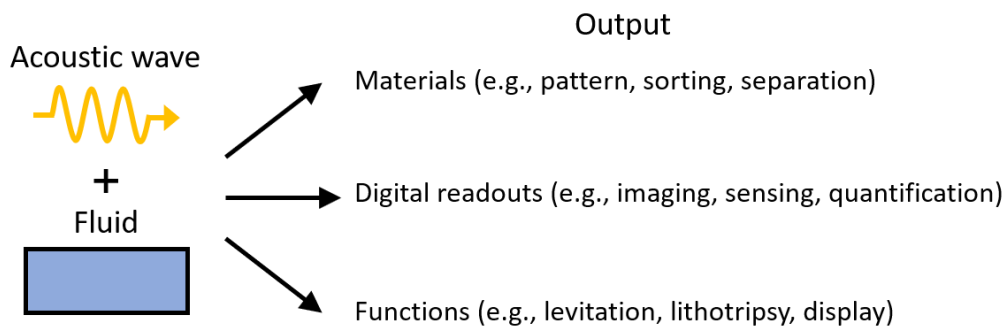

Figure 1.1: The schematic showing the target outputs that can be obtained using the acoustofluidic technology.

1.2 Basic theory of acoustofluidics

The classic acoustic equation can be derived by the combination of the simple force equation (Euler's equation, Newton's secondary law), the equation of continuity (mass conservation), and the equation of state(Kinsler et al., 1999). The commonly used linear acoustic equations are based on certain assumptions in order to simplify the theory. For example, the force equation ignored the viscosity, the equation of continuity assumes the fluid is incompressible, and the equation of state can be obtained by assuming the adiabatic process.

$$\rho_0 \frac{\partial \boldsymbol{v}}{\partial t} = -\nabla p \tag{1.1}$$

$$\rho_0 \nabla \cdot \boldsymbol{v} = 0 \tag{1.2}$$

$$c = \sqrt{\frac{p}{\rho_0}} \tag{1.3}$$

And these three governing equations indicate the relationship between the fluid particle velocity, pressure, and density. With the combination of these three equations, we can obtain the linear wave equation.

$$\nabla^2 p = \frac{1}{c^2}\frac{\partial^2 p}{\partial t^2} \tag{1.4}$$

With the variable separation, we can derive the Helmholtz equation and the harmonic solution of the acoustic wave, and further expand to different acoustic field calculation methods (e.g., angular spectrum).

Meanwhile, when acoustic waves propagating in the liquid, acoustic streaming will be generated due to the acoustic wave attenuation and resulting momentum flux transferred from the wave to the fluid. For many of the current studies, in order to simulate the acoustic streaming motion with a numerical method, the process usually is simplified by different assumptions. The governing equation can be indicated as:

$$\frac{\partial \rho}{\partial t} + \nabla \cdot (\rho \boldsymbol{v}) = 0 \tag{1.5}$$

$$\rho \frac{\partial \boldsymbol{v}}{\partial t} + \rho(\boldsymbol{v} \cdot \nabla)\boldsymbol{v} = -\nabla p + \mu \nabla^2 \boldsymbol{v} + \left(\mu_b + \frac{1}{3}\mu\right)\nabla(\nabla \cdot \boldsymbol{v}) \tag{1.6}$$

Noting that the first equation can correspond to the continuity equation used in the acoustic equation with nonlinear terms involved. And the second equation (Navier-Stokes Equation is another format of the force equation/ Newton's secondary law). With the development of the theory and numerical simulation method, three mainly three methods to simulate the acoustic streaming that can cover the range from microfluidic to

bulk fluid. For the classic microfluidic device, as the fluid layer is relatively thin, the thermal effect and viscous effect usually cannot be neglected. Thus, a perturbation theory is usually used to solve the equations. With the perturbation approximation, the equation can be divided into the first-order equation for the acoustic field, and time-averaged second-order equations for steady acoustic streaming. And during the practical solving process, the first-order equation should be solved first and then the second-order equation to cover both the acoustic and fluid effect. However, when dealing with a relatively larger fluid domain, the simulation (e.g., finite element method) will need a very large computation cost while the result may not fit well with the exact experimental result due to some unknown effect. To solve this, researchers also developed other simplification methods in order to effectively solve the equation. One method is the boundary driven streaming method(C. Chen et al., 2018; Wiklund et al., 2012a). While the thermal and viscous effect mainly have a major effect in the boundary layer (with a thickness relate to the kinematic viscosity and angular frequency $\delta_\nu = \sqrt{2\nu/\omega}$), and the upper fluid motion can be driven by the boundary layer streaming, the calculation can be simplified by calculating the boundary layer streaming using perturbation theory first in a relatively small domain, and then calculate the streaming in the upper larger domain. This method can significantly reduce the computation cost and be suitable especially when dealing with the large fluid domain with high frequency acoustic excitation. On the other hand, researchers also studied another method that directly applies the acoustic induced volume

force to the Navier-Stokes equation as an external force, so that the need for knowing the exact acoustic pressure distribution can be simplified(Alghane et al., 2010; Lighthill, 1978). With this method, the importance of the Reynolds stress for mean momentum flux is revealed. And the volume force generated by the acoustic waves can be calculated through the Reynold stress:

$$-F_j = < V_j \cdot \nabla V_j > + V_j < \nabla \cdot V_j > \tag{1.7}$$

With this method, the nonlinear acoustic induced volume force can be directly calculated when the wave velocity is known, and can be served as another method to simplify the calculation of acoustic streaming when dealing with large fluid domain (e.g., droplet, bulk fluid). This method specifically can be useful to investigate the individual effect of acoustic and fluid (although these two effects should be generated and considered together when practical use), or the smaller particle movement mainly dominant by acoustic streaming (e.g., nanoparticles in fluid). With the aforementioned theory, the acoustic field and streaming field can be calculated, used for deriving the acoustic radiation force and drag force that acted on the particles and further predict the trajectory of the particles inside the acoustofluidic domain.

1.3 Acoustic holography

The holography concept was first brought up in the field of optics by Dennis Gabor who won the Nobel Prize for related work in 1971, and gradually became famous for its powerful capability for imaging(Gabor, 1961; Sapozhnikov et al., 2015). The basic

principle of holography is the 3D wave field can be reconstructed from a 2D distribution of the phase and amplitude of the wave field. Besides the visualization function, with the development of optical tweezers, holography technique was also introduced as the holographic optical tweezers which can be used for dynamic control of the small particles(Spalding et al., 2011). As a classic wave format, the acoustic waves can also fit with the underlying mechanism and calculation of holography. While the acoustic wave information (i.e., phase, amplitude) can be directly measured by the detector e.g., microphone and hydrophone without the need of holography technique, acoustic holography experienced a unique path during the development(Sapozhnikov et al., 2015; J. Zhang et al., 2020). Traditionally, acoustic holography was used for the characterization and visualization of the acoustic field and the evaluate the complex structure that acoustic wave propagates through, e.g., nondestructive evaluation, acoustic imaging(R. K. Mueller, 1971). This traditional workflow was utilizing the obtained acoustic field to reversely derive the wave distribution in a relatively complex environment. With the manipulation technique development, researchers started to actively generate the desired acoustic field in the space using acoustic holography, as the flexibility of the wave modulation can also increase the flexibility of the manipulation. There are mainly two methods for generating acoustic holography: One is using the active transducer array, another is utilizing the passive material that can modulate the phase/amplitude when acoustic waves propagate through (Figure 1.2).

For the active method, Marzo et al firstly demonstrate an acoustic transducer array with the excitation frequency of 40 kHz for 3D particle manipulation in the air(Marzo et al., 2015b). By modulating the phase delay of each element, a single particle can be levitated and controlled translational and rotational in the mid-air. Building upon this concept, Marzo et al further demonstrated the holographic acoustic tweezers which formally bring up the acoustic version of the holographic tweezers(Marzo & Drinkwater, 2018). They built a phased array with 256 emitters with 40 kHz, and successfully demonstrated the real-time manipulation of multiple particles with the maximum size of 25 mm in the air. This system greatly shows the capability of manipulation of the acoustic waves and indicates the potential of using holographic acoustic tweezers for non-contact object control. Meanwhile, recent research also developed the phased array for 3D particle manipulation in the liquid. Yang et al demonstrated a self-navigated 3D acoustic tweezer that can achieve the real-time alignment of the particle(Y. Yang et al., 2021). Furthermore, with the combination of the time-reversal correction, the desired acoustic field can be formed through the complex material (e.g., skull) and effectively control the particle. Ghanem et al also demonstrated that by using the underwater phased array, a single particle can be arbitrarily manipulated in the bladder of a big(Ghanem et al., 2020). This study moves one step forward applying the acoustofluidic manipulation technique to practical in vivo application.

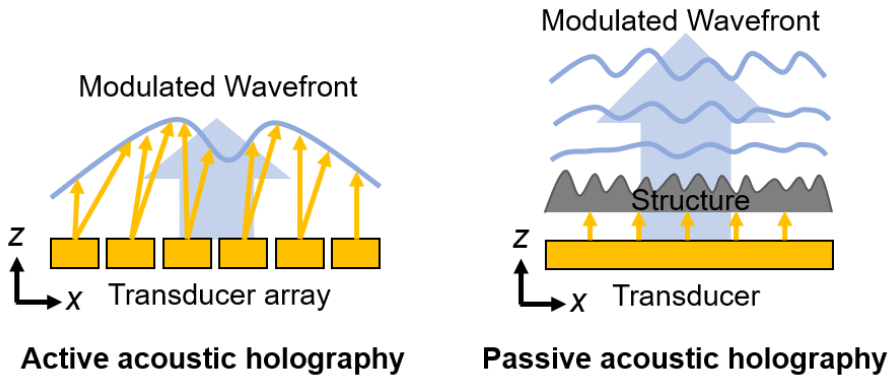

Figure 1.2: Schematic showing two classic acoustic holography configurations.

For the passive structure to generate the acoustic holography, different methods were designed that can modulate the phase of the incidence acoustic wave. Generally, by designing the passive structure that has specific modulation for each unit, the desired acoustic field can be generated. Xie et al designed a metamaterial with each unit set as a subwavelength pixel, the arbitrary pressure field can be rendered by using a single transducer(Xie et al., 2016). This method opens up a new direction that can modulate the acoustic wave in a high resolution and cost-efficient way. Memoli et al also developed a new method that separated the kinoform into multiple units, and can generate the desired acoustic field in a reconfigurable manner by assembling the units(Memoli et al., 2017). They applied an image compression method to reduce the need for the numbers of different phases. Thus, the field can be generated with multiple units that corresponding to several digits. This method compressed the required information that needed to generate the holography and further reduced the fabrication requirement and cost. While

the aforementioned methods have different advantages, the carried information (i.e., pixel numbers of the holography) is still limited to generate more complex acoustic field. Melde et al developed an underwater acoustic holography method that utilizes the 3D printed kinoform to control the acoustic wave while the phase information is embedded directly in the thickness of the structure(Melde et al., 2016a). With this method, the kinoform contains over 100,000 pixels that can generate a much more complex acoustic field. They also demonstrated that this method can be applied to pattern the PDMS particles to arbitrary shapes or trap them to move to follow a certain path. This study made a breakthrough for underwater acoustic holography. Furthermore, Melde et al also demonstrated that acoustic holography can be used as a fabrication method, with which the pattern can be gelated to a certain shape(Melde et al., 2018). The 3D printed thickness-based phase hologram is a very effective and cost-efficient way to generate an arbitrary acoustic field in the liquid. Based on this technique, Jiménez-Gambín et al show the formation of acoustic fields of complex spatial distribution inside the skull(Jim, 2019). This potentially opens up the new direction of applying holography for biomedical applications in a low-cost way.

1.4 Acoustic droplet system

Droplets are a classic fluidic system, where not only the motion of the droplet itself but also particle manipulation inside the droplet has drawn great research interest for different fields spanning from physics to biology. The dynamics of the liquid droplet were

firstly studied by Rayleigh who also derived the approximation of the oscillation frequency of the droplet with external excitation(Rayleigh, 1879). As the acoustic levitation technique developed, Shen et al studied the droplet vibration motion using acoustics in the air(Shen et al., 2010). They identified the nonaxisymmetric sectorial oscillation of the liquid droplet with an amplitude-modulated acoustic wave. Foresti et al also demonstrated that the droplet can be deformed during the rotation using airborne acoustics(Foresti & Poulikakos, 2014). Surface acoustic wave also serves as an effective way to drive the fluid motion as the wave can propagate through the substrate and leak into the fluid. While the droplet is commonly sitting on top of the substrate, various interesting phenomena were observed with the interaction between surface acoustic wave and droplet (Figure 1.3). Tan et al observed that by using the high frequency surface acoustic wave to drive the droplet, a capillary wave can be formed on the free surface of the droplet(Tan et al., 2010). Meanwhile, they provided a detailed theoretical study and numerical simulation to explore the droplet acoustic field and characterization of the capillary wave. Brunet et al presented that with the surface acoustic wave excitation, the droplet can generate a creeping-jumping oscillation motion, and with higher input power, the droplet may move along the direction of the surface acoustic wave propagation(Brunet et al., 2010). They also indicated that the surface deformation of the droplet is related to the combined effect between the acoustic streaming and radiation pressure generated by the acoustic waves. Manor et al demonstrated an extensive study

and revealed that the droplet vibration motion and streaming motion under the high-frequency excitation can be tightly connected with the contact angle when sitting on the different substrate material(Manor et al., 2011). Meanwhile, Baudoin et al showed that the modulated acoustic signal can generate higher droplet oscillation amplitude and promote droplet mobility(Michael Baudoin et al., 2012). Rezk et al also demonstrated an interesting acoustowetting phenomenon showing that the droplet can form a thin liquid film along the opposite direction of surface acoustic wave propagation(Rezk et al., n.d.).

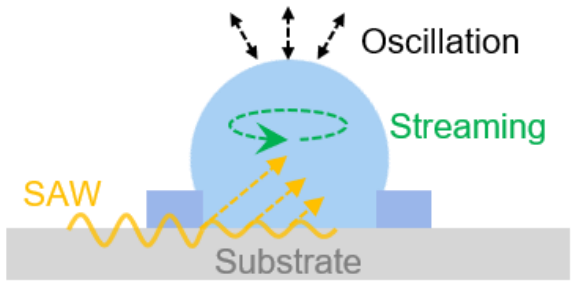

Figure 1.3: Schematic of the SAW droplet interaction system.

With the surface acoustic wave exciting, particles inside the droplet also experience various forces that can guide them to a certain position in the drop. Li et al demonstrated that with the asymmetric SAW propagation, azimuthal acoustic streaming can be generated, which can rapidly concentrate the microparticles due to the shear-induced migration(H. Li et al., 2007). Shilton et al further demonstrated that with a focused surface acoustic wave, the particle concentration efficiency and speed can be

improved due to the increased wave intensity(Shilton et al., 2008). Bourquin et al also introduced a novel method to drive the fluid motion and particle manipulation on a disposable chip(Bourquin et al., 2010). In their study, the slanted interdigital transducer is used which can generate different frequencies from various spatial locations on the transducer. Thus this method can provide a more flexible way to manipulate the fluid and particles with the tuning of the acoustic parameters. He continued to prove that with this setup, particles can be separated with the same size but different densities in a blood droplet(Bourquin et al., 2014). Since particles with different sizes or other mechanical properties will experience different acoustic radiation forces and drag forces, they can be separated with different acoustic parameters. Destgeer et al demonstrated that the microparticles can be concentrated to different spatial locations in the droplet under the excitation of surface acoustic wave, and for different contact angle, the position of the particles although may be different, can still be distinguishable and leads to the separation(Destgeer et al., 2017). Following this work, Destgeer et al continued exploration of the particle trajectory inside the droplet(Destgeer et al., 2016). They indicated that the particle balanced position in the droplet is connected with two ratios, one is the surface acoustic wave attenuation length compare to the droplet size, another is the particle size compare to the wavelength. These two ratios can divide the particle positions into four regions where particles may be focused in the middle, or distributed near the boundary, or follow certain circular trajectories. With the development of

transducer design and separation theory, Zhang developed an acoustic based centrifuge system for size based cell separation(N. Zhang et al., 2021). In their design, an omnidirectional spiral surface acoustic wave can be generated by a novel interdigital transducer design, and the particles can be separated and directly extracted using a syringe.

1.5 Acoustic separation in continuous flow

Acoustic-based particle separation in continuous flow has been studied for a relatively long time. Well-established theory and device design make this method suitable for variable practical applications in the field of biology, chemistry, and material sciences(M. Wu et al., 2019). The basic principle of the method is based on the different acoustic radiation forces and drag forces acting on particles of different sizes. With the force difference, the particle displacement along the cross flow direction can be varied and larger particles can be separated from the small particles in a continuous flow (Figure 1.4). Following the standing wave based mechanism, the acoustic separation can be achieved using either bulk acoustic wave and surface acoustic wave. Generally, as surface acoustic wave based device usually has a higher frequency, the attenuation length of the acoustic wave in the liquid will be smaller. Thus, a microfluidic channel is usually used to cooperate with the device. The advantages of the surface acoustic wave based device are the separation efficiency and resolution can reach a very high value, while on the other hand, the throughput is relatively low. The bulk acoustic wave based device is commonly

more inexpensive, and the fluid channel can be engineered with a larger dimension thus may lead to higher throughput. However, due to the larger scale and lower frequency, the separation efficiency and resolution may not be as same as the surface acoustic wave device. Overall, the acoustic based separation features for its biocompatibility and non-labeling property and has broad application potential. For example, Petersson et al demonstrated a BAW based device that can separate the blood cells from human blood(Petersson et al., 2005), and this capability can be used to transfer the blood cells from their original plasma environment to the new plasma solution. Following this study, Lenshof et al further demonstrated the whole blood plasma separation using acoustic waves (Lenshof et al., 2009). On the other hand, Adams et al showed a method to separate the blood cells in high throughput and temperature-controlled manner(Adams et al., 2012). Nam et al demonstrated a platelet separation device using surface acoustic waves (Nam et al., 2011). With the measurement of the collected sample, the purity of the platelet can reach ~98% while the blood cell removal rate can reach over 99%. Chen et al further demonstrated a platelet separation method using bulk acoustic wave, which can reach a 10 mL/min throughput(Y. Chen et al., 2016a). Besides the blood components, cancer cells and bacteria were also demonstrated to be separated from the blood sample. For example, Wu et al demonstrated a SAW based method for high throughput CTC (circulating tumor cell) separation and phenotyping(M. Wu et al., 2018). Ai et al indicated a SAW based method that can separate the E. Coli from the blood cells(Ai et al., 2013). Besides the

microscale particle separation, various nanoscale bioparticles can also be separated using surface acoustic wave. For example, Wu et al showed that they can separate the exosome sample directly from the whole blood(M. Wu, Ouyang, et al., 2017). In their design, two units were utilized with the tilted angle setup, the blood cells and relatively large vesicles can be separated sequentially and leave the exosome in the plasma sample. Different from the classic standing wave based separation, Collins et al demonstrated a micro-vortex-based nanoparticle separation/differential concentration of the nanoparticles with different sizes(Collins et al., 2017). With a high frequency focused IDT, a strong vortex streaming can be formed in the microchannel, and particles can be pushed along the vortex streamline and have different cross flow displacement with different sizes. Collins et al also demonstrated a novel method that combines both acoustic radiation force and dielectrophoretic force to separate the nanoparticles(Collins et al., 2014). With the IDT electrodes embedded under the microchannel, particles can move along the tilted electrodes and being separated out. While substantial efforts have been developed for acoustic separation, more progress can be envisioned in order to push the technology toward the practical usage.

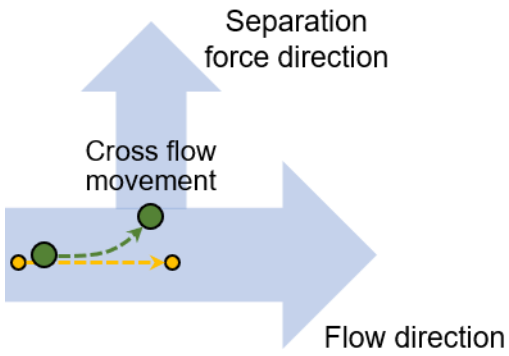

Figure 1.4: General illustration of acoustic-based particle separation in continuous flow.

1.6 Dissertation outline

This dissertation describes our research efforts on exploring the underlying mechanism of acoustofluidic particle manipulation and the utilization of the techniques for biomedical applications. A series of works are introduced to demonstrate the interplay effect between the acoustic wave and fluid motion based on three classic fluid models including bulk fluid, droplet, and continuous flow. Chapters 1-5 are expanded versions of published, submitted, or prepared research or review manuscript. A short motivation and a brief literature review are firstly discussed at the beginning of each chapter in order to indicate the innovation and features of our works.

In chapter 2, we introduce the acoustofluidic holography technique which can be utilized for micro- to nanoscale particle manipulation. We have discussed how the complex acoustic field can interact with the fluid motion and cooperate with each other.

This technology can form the 2D or 3D arbitrary shape cell pattern with a fine resolution and complexity. Meanwhile, with the same experimental configuration, multiple functions can be achieved including single particle rotation, particle concentration, and separation with a broad size range.

In chapter 3, we present an acoustofluidic centrifuge system that is based on an acoustic driven spinning droplet. We discuss the underlying physics and how this method can be applied to biomedical applications. With the spinning droplet, nanoparticles with the size down to 28 nm can be rapidly concentrated. Also, the particles with different sizes can be differentially concentrated. By building the dual-droplet acoustofluidic centrifuge system, we can separate and transport the smaller particle from one droplet to another, which also enables the separation of the exosome subpopulation.

In chapter 4, we report two acoustic based separation methods that can be used for blood components separation including the platelet and plasma. For platelet separation, a plastic device based acoustic resonator is built with high throughput. For plasma separation, surface acoustic wave is utilized while multiple other units are added with the acoustic separator and form an integrated prototype. We have demonstrated this system can be applied to small animal (i.e., mice) plasma separation, and potentially be utilized for plasmapheresis or plasma exchange in the future.

Chapter 5 summarizes this dissertation and presents perspectives for future study.

Chapter 2: Acoustofluidic holography for particle manipulation

In this chapter, we describe an acoustofluidic holography technique that utilizes both arbitrary acoustic fields and collabrative fluid motion to provide an efficient approach for particle manipulation. This method was employed for arbitrary cell patterns with a controllable resolution as well as multiple other functions including particle concentration, separation, and rotation. Section 2.1 introduces the motivation of this work. Section 2.2 indicates the materials and methods used for the experiment. Section 2.3 details the theoretical model and working mechanism including the acoustic hologram, fluid dynamics induced by arbitrary acoustic waves, and particle force induced by the acoustic waves and fluid motion. Section 2.4 and 2.5 describes the major application: cell patterning, and some other applications. Lastly, section 2.6 is given on the discussion and future works. The major work presented in this chapter is published on ACS Nano.

2.1 Motivation

With the development of particle manipulation technique, various particle handling platforms have been explored, experiencing extensive attention to various areas such as protein folding(Dobson, 2003) and enzyme kinetics(Svoboda et al., 1994). These technologies indicate a new capability that can trap individual object for example viruses, bacteria, and cells, in a "tweezing" format. Specifically, these methods include optical(Grier, 2003), magnetic(Lipfert et al., 2011), plasmonic(K. Wang et al., 2011), and optoelectronic tweezers(Chiou et al., 2005), and each of them indicates unique advantages

for certain senarios. For example, optical tweezers are able to provide the best spatial resolution, thus can be applied to studies ranging from single molecule to cellular manipulation(Ashkin, 1999). While it shows extreme potentials for force spectroscopy and biomolecular manipulation, optical tweezers usually require complex optical configuration, including high-powered lasers and high numerical aperture objectives, and potentially could damage the biological samples(Rasmussen et al., 2008). Acoustic based manipulation techniques, namely, acoustic tweezers, have emerged over the past decade as a non-contact, non-invasive and label-free alternative to optical tweezers(Collins et al., 2015; Guo et al., 2016; Ozcelik et al., 2018; Reboud et al., 2012; J. R. Wu, 1991; M. Wu, Ouyang, et al., 2017; S. P. Zhang et al., 2018). Although it would be difficult for acoustic manipulation techniques to achieve the spatial resolution as high as the optical tweezers, they possess other unique advantages, e.g., able to perform manipulations in a large working area and can control particles with the size over a broader range, from nanometers to millimeters(Bourquin et al., 2010; Destgeer & Sung, 2015; Naseer et al., 2017).

Various acoustic tweezers platforms have been demonstrated revealing different capbilities. The most widespread design is the standing wave fields based manipulation which can provide stable trapping force (Glynne-Jones et al., 2012; Ozcelik et al., 2018). For standing wave, the interference between two acoustic beams propagating in opposite directions generates a periodic, grid-like pressure distribution, enabling particles of

different properties to be trapped at the pressure nodes or antinodes (Armstrong et al., 2018; Bruus, 2012; B. Kang et al., 2018; Lenshof et al., 2012; Schmid et al., 2014). The standing wave generation usually needs pairs of acoustic transducers or reflectors. And due to its simplicity and stable performance, the standing wave based acoustic manipulation have been utilized for various applications, e.g., cell separation, sorter, and study of cell properties(Gu et al., 2020; Ozcelik et al., 2018). While the experimental configuration is simple, the capability it shows also possess relatively simple feature. It is difficult for the classic standing wave based manipulation to form the customized, arbitrary patterns of particles that could be necessary for various applications. As an alternative, single beams (*e.g.*, Bessel beams) can provide an optical tweezer format manipulation in which a single trapping point exsist that can be used for controlling individual particles (Baresch et al., 2016; J. Lee et al., 2010). With this method, single objects can be levitated and dynamically controlled in three dimensional spaces. This method potentially could be very useful for contactless object manipulation in the air or in vivo, which benefits various applications for human life science(Drinkwater, 2016; Gu et al., 2020; Y. Yang et al., 2021). While this method enables the forces act on individual particles to be well controlled; this property will have insufficient capability dealing with high-throughput applications where multiple particles involved. Furthermore, the optical tweezers can utilize a spatial light modulator to efficiently change the location of the trapping point, the spatial acoustic modulator is still a technology barrier and under

development. Thus, for current single beam acoustic tweezers, it usually require a relatively large and complex experimental space and configuration in order to change the position of the transducer or provide phase modulation for various transducers.

Various extensive efforts have been made to generate more complex acoustic fields through acoustic metamaterials(Cummer et al., 2016), phononic crystals(Fuhrmann et al., 2011), and phased arrays(Marzo et al., 2015a). However, most current research still focuses on the object manipulation in air as a proof-of-concept demonstration, which may not be suitable for biomedical applications; most cells or related bioparticles are contained in their native liquid environment. Several most current studies demonstrate the dynamic acoustic tweezers for underwater manipulation using a phased array. While this is a breakthrough for the acoustic tweezer technique, the complex experimental setup and high expense still limit the common use at this stage, and the resolution is still insufficient for high-resolution manipulation. Recently, acoustic holography has shown great potential for particle manipulation(Marzo & Drinkwater, 2018). The acoustic holography was originally proposed for real-time image reconstruction of physical objects(Veronesi & Maynard, 1987), with which a hologram image can be reconstructed by illuminating the interface with a coherent light source and recording the deformation pattern. And it has recently experienced renewed attention for acoustic imaging and acoustic manipulation. There are two commonly used configurations for acoustic holography in the ultrasound regime: 1. a phased array composed of multiple transducers and each element within the

array can be modulated(Marzo et al., 2015a), 2. an acoustic kinoform which can be placed in the beam propagation path, the kinoform containing the phase information can discretize and reconstruct the desired wavefront(Melde et al., 2016b). While results have been promising, one important problem that the current method has specifically for underwater manipulation is: the current acoustic holographic technologies target at manipulation of relatively large (hundreds of micrometers), low-density particles which have negative acoustic contrast factors. While for cells or other bioparticles, due to the diffraction limit, insufficient force, and fluid turbulence(Melde et al., 2016b, 2018), it still has difficulty providing effective manipulation. And due to this property, many particles of interest, including most cell types, extracellular vesicles, metals, and many polymers have not been explored to be manipulated as most of these particles have positive acoustic contrast factors and are physically smaller than 100 μm(Ai et al., 2013). In general, most solid particles suspended in aqueous solutions have positive acoustic contrast factors(Ai et al., 2013), meaning that current systems possess insufficient capability for practical biomedical applications. Furthermore, the recent works mainly rely on acoustic radiation force and neglect fluid motion initiated by the acoustic waves, which also contribute to particle movement, especially for small particles that have small responses to the traveling acoustic wave radiation force(Friend & Yeo, 2011; Wiklund et al., 2012b). Thus, the holographic acoustic particle manipulation still needs further development and technology innovation in order to be applied to practical biomedical applications.

In order to deal with these problems and explore new capabilities of the holographic acoustic manipulation, we demonstrate an acoustofluidic holography (AFH) platform that addresses the limitations of previous approaches and enables precise manipulation of micro/nano particles, such as cells, polymers, and metals, with different physical properties (Schematic as shown in Figure 2.1). Moreover, the combined acoustic and hydrodynamic physics utlized in the platform enables the manipulation of particles with a wide size range, as well as the high-resolution patterning of cells. We infused the complex acoustic modulation and fluid motion controlling into a simple 3D printed container with a kinoform bottom. Thus it leads to the experimental configuration to be one acoustic transducer and one plastic structure. The kinoform can modulate the phase of the acoustic wave and then initiate the controllable three-dimentional acoustic field and fluid motion.

The acoustofluidic holography, as its term stated, is the synergetic effect of the acoustic holography and induced fluid motion. With the acoustic wave propagate in the liquid, it will also generate acoustic streaming that can guide the movement of particles. On the other hand, the the acoustic wave can interact with the liquid-air interface and triger the interface deformation and create the local pressure field that can trap the particles. With this method, particles inside the bulk fluid will experience both a drag force by fluid motion and an acoustic radiation force by acoustic waves. As the container is a confined space with one open side (i.e., liquid-air interface), a circulating flow can be

generated within the space and utilized for particle manipulation. Specifically, the small particle can be guided move along with the flow through out the whole fluid domain. With the specific acoustic fields, the particles can be trapped at certain pressure nodes when it pass through the position. Different from previously proposed holographic based manipulation techniques(Melde et al., 2016b, 2018) which usually perform the manipulation in an unbounded medium, the AFH configuration limits the working area in a confined space and utilize the non-slip boundary conditions caused by the container side walls. The container shows a very small impact on acoustic wave propagation, thus can be utilized to coordinate between the acoustic wave and fluid motion. With our AFH configuration (transducer and container setup), multiple functions can be realized including cell patterning, single particle rotation, and particle concentration/separation. Furthermore, it is also capble of generating certain tunable function as multiple acoustic fields can be encoded into single structure and triggered by different frequencies. This work indicates an useful methodology applying the acoustofluidic holography manipulation method into practical applications such as bioprinting, tissue engineering, cell separation, and micro/nanomaterial synthesis and assembly.

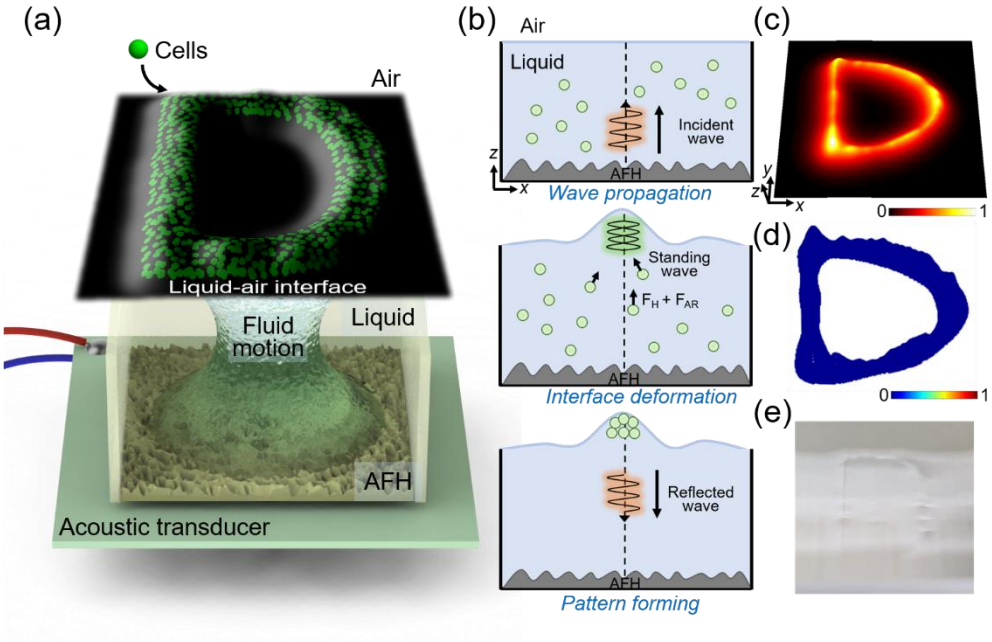

Figure 2.1: Schematic of the configuration and mechanism of cell/particle patterning *via* acoustofluidic holography. (a) Illustration of the AFH experimental setup. (b) Description of the AFH pattern function. In the figure, F_H indicates the hydrodynamic force (drag force); F_{AR} indicates the acoustic radiation force. (c-e) An example of the designed liquid-air interface deformation with the pattern of letter "D". The calculated deformation pattern (c), pressure distribution (d), and photo of the experiment (e) are shown.

2.2 Materials and methods

2.2.1 Experimental setup and materials

The experimental configuration consists one 3D printed box with the kinoform structures at the bottom, a rectangular transducer (STEMiNC, USA), with a layer of couplant gel (Couplant D, Olympus, Japan) between them for acoustic wave transmission as shown in Figure 2.2 (Gu et al., 2020). A function generator (AFG 3011, Tektronic, USA) and an amplifier (25A100A, Amplifier Research, USA), were used for acoustic transducer

exicitation. The particle and fluid motion (e.g., streaming) were observed under an upright microscope (BX51WI, Olympus, Japan) and the pictures and videos were captured by the camera under bright field or fluorescent field. 1 μm polystyrene particles was used to indicate the flow field by capturing the motion and analyzing use the PIVLab toolbox(Thielicke & Stamhuis, 2014) in Matlab, or ImageJ (NIH, USA). This method can lead to the analysis of the flow field velocity distribution and streamlines. The acoustic field is measured using a hydrophone (HNC0100, Onda Corporation, Sunnyvale, CA) connected to an oscilloscope (DPO4104, Tektronix, USA). A custom 3-D scanning platform controlled by LabVIEW software (NI Corporation, TX) is used to move the hydrophone and scan the field.

For the particle/cell patterning experiment, HeLa S3 cells, NIH3T3 cells (fibroblast), and 10 μm polystyrene particles were used(Gu et al., 2020). For small-area particle patterning, 1 g/L Pluronic F68 (Sigma-Aldrich, USA) is used as the surfactant to decrease the surface tension. 5% w/v Gelatin methacryloyl (Sigma-Aldrich, USA) is used for the fixation of the cell pattern. Both HeLa cells and NIH3T3 cells were cultured in DMEM (Gibco, Life Technologies) containing 10% fetal bovine serum (Gibco, Life Technologies) and 1% penicillin-streptomycin (Mediatech). Cells were maintained in a cell culture incubator (Nu-4750, NuAire) with a temperature of 37°C and a CO_2 level of 5%.

For single particle rotation experiments, 100 μm, 300 μm, and 500 μm polyethylene particles (Cospheric, USA) are tested. For particle/cell concentration experiments, HeLa

cells, *E. coli* bacteria (ATCC, VA, USA), PLGA, polystyrene (Sigma-Aldrich, USA), and metal particles (nanoComposix, USA) with sizes of 1 μm, 530 nm, 400 nm, and 80 nm, respectively, are tested in the AFH configuration. In the particle separation experiment, 10 μm, 4.19 μm, 3 μm, 1 μm, 970 nm, and 530 nm polystyrene particles (Sigma-Aldrich, USA, Bangs Laboratories, USA) with different fluorescence tags are tested in pairs, in order to explore the capability of particle separation with different size difference (Gu et al., 2020).

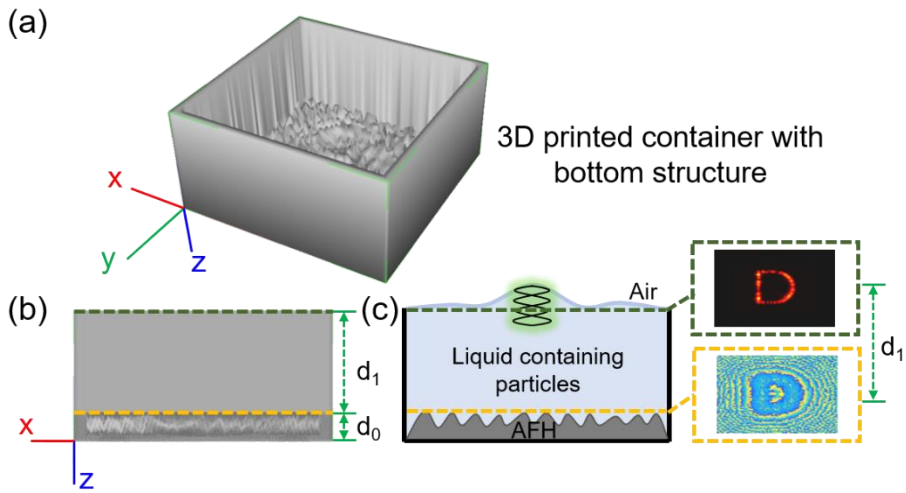

Figure 2.2: Illustration of the 3D printed container. (a) The 3D model of the container with the structure as the bottom. (b) The side view of the 3D model, the height of structure and container are defined as $\boldsymbol{d_0}$ and $\boldsymbol{d_1}$, respectively. (c) The 2D schematic of the experimental setup. A liquid domain containing particles are between the bottom structure and liquid-air interface and has the thickness of $\boldsymbol{d_1}$ which also is the designed distance between the bottom phase map and image plane.

2.2.2 Cell preparation

For the HeLa S3 cells (ATCC, USA) staining, 1mL of calcein AM (0.5 mmol L^{-1}, Life Technologies, USA) was added to 1 mL of cells suspended in phosphate buffer saline (PBS), followed by incubation at room temperature for 30 min(Gu et al., 2020). Stained cells were then centrifuged and resuspended in 1 mL of PBS, the *E. coli* bacteria (ATCC, USA) is stained using a BacLight Live/Dead viability kit (Thermo Fisher, USA), 50 μL of HeLa S3 cells are collected after AFH treatment(Gu et al., 2020). The cells are double-stained with calcein AM (CAM) and propidium iodide (PI) after the 20 min incubation. The viability is measured by counting CAM-positive and PI-negative cells under the microscope. For the confocal images of the cultured NIH3T3 cells, Alexa Fluor 488 (Thermo Fisher, USA) is used for the cells, and 7-Aminoactinomycin D (Thermo Fisher, USA) is used for the cell nucleus(Gu et al., 2020).

2.3 Theoretical model and working mechanism

2.3.1 Acoustic hologram

Multiple acoustic hologram algorithms are complemented and tailored for this study. The most common algorithm is the iterative angular spectrum method based acoustofluidic hologram. The iterative angular spectrum method(Mellin & Nordin, 2001) is combined with the liquid-air interface deformation calculation, where the surface deformation can be obtained by knowing the intensity distribution and the transfer

function derived from the pressure equilibrium equation(R. K. Mueller, 1971). The surface deformation can be expressed as:

$$\mathrm{H}_s(\mathrm{k}_x, k_y; z_s) = \mathrm{P}_r(k_x, k_y; \mathrm{z}_s)\mathrm{G}(k_x, k_y; \mathrm{z}_s) \tag{2.1}$$

Where $\mathrm{k}, \mathrm{k}_x, \mathrm{k}_y$ indicate the wavenumber in join, x, y directions, respectively, $\mathrm{z}_s, \mathrm{z}_b$ are the vertical coordinates of the liquid surface plane and bottom plane, respectively. And the calculated transfer function $\mathrm{G}(k_x, k_y; \mathrm{z}_s)$ is:

$$\mathrm{G}(\mathrm{k}_x, \mathrm{k}_y; z_s) = \frac{1}{\rho_0 g + \gamma({k_x}^2 + {k_y}^2)} \tag{2.2}$$

where ρ_0 is the density of the liquid, g is the gravity acceleration, and γ is the surface tension of the liquid (See Figure 2.4 for the characterization of the transfer function). $\mathrm{P}_r(k_x, k_y; \mathrm{z}_s)$ is the Fourier Transform of the acoustic radiation pressure map:

$$\mathrm{P}_r(k_x, k_y; \mathrm{z}_s) = \mathcal{F}\left(\frac{p(x, y; z_s)^2}{\rho_0 {c_0}^2}\right) \tag{2.3}$$

where $p(x, y; z_s)$ is the pressure distribution on the z_s plane.

Based on the angular spectrum method, we have:

$$P(\mathrm{k}_x, k_y; z_s) = \mathrm{P}(k_x, k_y; \mathrm{z}_b)e^{j(z_s - z_b)\sqrt{k^2 - {k_x}^2 - {k_y}^2}} \tag{2.4}$$

This can reveal the relationship between the bottom pressure and the interface deformation through the following relationship:

$$\mathcal{F}\left\{\sqrt{\mathcal{F}^{-1}\left[\frac{\mathrm{H}_s(\mathrm{k}_x, k_y; z_s)}{\mathrm{G}(\mathrm{k}_x, \mathrm{k}_y; z_s)}\right]\rho c^2}\right\} = P(\mathrm{k}_x, k_y; z_s) = \mathrm{P}(k_x, k_y; \mathrm{z}_b)e^{j(z_s - z_b)\sqrt{k^2 - {k_x}^2 - {k_y}^2}} \tag{2.5}$$

Thus, by designing the liquid-air interface deformation, we can directly calculate the phase distribution at the bottom structure and generate the thickness map for the 3D printed kinoform structure (See Figure 2.3 for comparison between theoretical calculated interface deformation and experimental results).

The detailed design strategy is introduced in the publication(Gu et al., 2020). Generally, a random field distribution is split into multiple spatial frequency components by a 2D Fourier Transform and used to calculate the field distribution at a target plane. Then, transfer functions are used to translate the acoustic field to interface deformation. The deformation then will be changed to the desired pattern and backpropagte to obtain the bottom phase map. Several iterative processes are needed to minimize the erroneous components.

Also, as $\sqrt{{k_x}^2 + {k_y}^2}$ approaches k, the spectral transfer function $\mathrm{h}(\mathrm{k}_x, k_y; \mathrm{z}) = e^{j(z_s - z_b)\sqrt{k^2 - {k_x}^2 - {k_y}^2}}$ is inherently under-sampled which may cause aliasing errors. The spatial frequency truncation is applied and the cut-off spatial frequency is given by(Zeng & McGough, 2008):

$$k_{cut-off} = k\sqrt{\frac{D^2}{D^2 + 2(z_s - z_b)^2}} \tag{2.6}$$

where D is the length of the bottom structure. This spatial frequency cut-off can deal with the under-sampled angular spectra and minimize the influence of higher spatial frequency components.

Figure 2.3: Theoretical calculated liquid-air interface deformation and experimental realization.

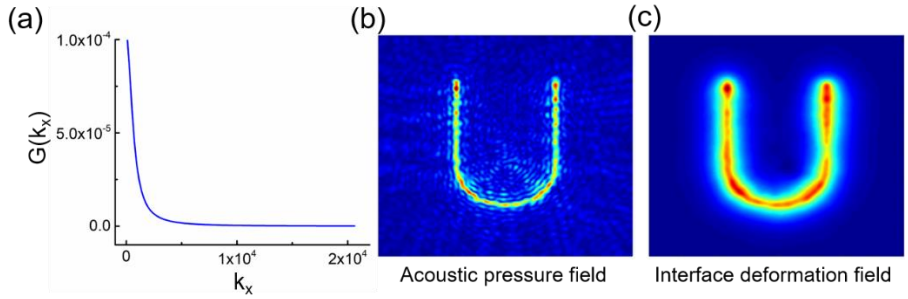

Figure 2.4: The function of the interface deformation. As the transfer function showing a spatial frequency low-pass effect (a), the interface deformation pattern shows a clearer image and pattern effect (b) compare to the generated acoustic pressure field (c).

The multiple frequency acoustofluidic holography provides more freedom for the field modulation. Specifically, this methods exploits the chromatic variation within the Fresnel focal depth for multiple frequencies. When two different pressure distributions are encoded into one bottom phase, both of the fields exist simultaneously as acoustic wave excited(M. D. Brown et al., 2017; Teo & Reid, 1986). The pressure field will be in-plane with one corresponding excitation frequency while the field respective to another frequency will be out-of-plane as the wavelength dependence of the phase offsets during propagation. The relationship between the frequencies and distances of the imaging plane can be approximated as:

$$f_{ac}d_{ac} = f_c d_c \tag{2.7}$$

where f_{ac}, f_c, d_{ac}, d_c are the frequency designed for first pressure field, the frequency designed for second field, the imaging distance of the first field, and the imaging distance of the second field, respectively.

For binary acoustic hologram, an acoustic lens composed of a high-resolution pixel array encoded with binary digits (i.e., two distinct phase values) is developed. The digit values at all the array pixels are calculated via a direct binary search method (Leportier et al., 2015; J.-P. Liu et al., 2019). At the beginning of this method, a random binary phase distribution $L_0(m,n)$ is used as the initial input and encoded in the acoustic lens, where m and n are the pixel indices along with x and y directions of the lens. Then, transmission acoustic fields with certain distances away from the acoustic lens plane is calculated and further compared with the target acoustic fields. On the one hand, to calculate the acoustic fields on the target plane, the angular spectrum method was used, as:

$$p(\mathrm{m}',\mathrm{n}';z_i) = \mathcal{F}^{-1}{}_{2D}(\mathcal{F}_{2D}\left(p(m,\mathrm{n};\mathrm{z}_0))e^{j(z_i-z_0)\sqrt{k^2-{k_x}^2-{k_y}^2}}\right) \tag{2.8}$$

where $p(\mathrm{m}',\mathrm{n}';z_i)$ is the acoustic field of the i th target plane with the distance of z_i away from the lens plane. $p(m,\mathrm{n};\mathrm{z}_0)$ is the acoustic field of the lens plane. k, k_x, and k_y are the wavenumbers in joint, x, and y directions, respectively. On the other hand, to perform acoustic field comparison, the mean square error (MSE) between the calculated and target acoustic fields is derived by:

$$MSE = \frac{1}{N}\sum_{i}\sum_{m,n}\left(p(\mathrm{m}',\mathrm{n}';z_i) - p(m,\mathrm{n};\mathrm{z}_0)\right)^2 \tag{2.9}$$

where N is the total number of pixels in the acoustic lens. During the process of the direct binary search method, each pixel value will experience the flip and compare pipeline. This means the phase value at that pixel will flip to the other binary digit value

(i.e., “0” to “1”, or “1” to “0”), and the corresponding acoustic fields will be recalculated and then compared to the target fields. If the MSE becomes lower, the new phase value will be selected; otherwise, it will be flipped back to its original value. Once all the pixels experience the flipping and comparison process, one searching cycle is completed. After multiple searching cycles (~10 cycles), the MSE will gradually converge to the minimum, which means the generated acoustic fields will have the least difference compared to the target acoustic fields.

During the vortex calculation, differing from the common phase-only or amplitude-only holography calculation, we encoded both amplitude and phase information into a single structure in order to arbitrarily control the wavefront. The double-phase holography method(Davis et al., 1999; Hsueh & Sawchuk, 1978) is used here which decomposes the complex value into two phase quantities, so that any complex wavefront inside the unit circle can be expressed by:

$$\mathrm{p(x,y)e}^{i\emptyset(x,y)} = \frac{1}{2}e^{i(\emptyset+\tau)} + \frac{1}{2}e^{i(\emptyset-\tau)} \tag{2.10}$$

where

$\tau = \cos^{-1} p(x,y),\ and\ 0 \leq \tau \leq \frac{\pi}{2}$

By adding the extra term related to the amplitude to the original phase term, we successfully shaped the spectrum and encoded amplitude information onto a phase-only kinoform with a single structure. Thus, not only can angular momentum be transferred to the fluid, but the pressure field can also induce vortex streaming near the interface.

After the holographic kinoform is finalized, the pressure field at the target plane can be calculated and validated using the Rayleigh-Sommerfeld integration(M. Brown et al., 2017; Sheppard et al., 2013):

$$\mathrm{p}(\mathrm{x}_T, \mathrm{y}_T)|_{z=z_T} = \frac{1}{2\pi}\iint p(x_b, y_b)|_{z=z_0} e^{i\Delta\phi(x_b,y_b)}\left(-\frac{ik}{r}+\frac{1}{r^2}\right)e^{ikr}\,\mathrm{dS} \qquad (2.11)$$

where S is the target plane area and $\mathrm{r} = \sqrt{(x_T - x_b)^2 + (y_T - y_b)^2}$ is the distance between the points at the bottom plane and the target plane.

2.3.2 Fluid dynamics induced by acoustic waves

When an acoustic wave impinges on the interface between liquid and air, the radiation pressure causes the interface to deform. Engineering the acoustic wavefront through the use of a 3D printed acoustic holographic kinoform offers precise control over the deformation of the interface. A hologram image can be reconstructed by illuminating the interface with a coherent light source and recording the deformation pattern(R. K. Mueller, 1971). This method, termed acoustic holography, is widely used for real-time object image reconstruction. At the same time, in a confined space, the deformation of the interface results in both an acoustic radiation force and induced streaming that can be harnessed to move particles in the fluid, enabling rapid particle patterning and cellular self-assembly (Figure 2.5). Through the use of acoustofluidic holography, the deformation of the interface is highly controllable, and arbitrary patterns can be formed. These deformation patterns give rise to pressure nodes and antinodes that are created by the reflection of the acoustic wave by the interface. Depending on the material properties of

particles inside of the fluid, they can potentially be trapped in these pressure nodes or antinodes. Meanwhile, the streaming flows continuously directs particles towards the nodes. Thus, particles in the fluid will flow into and be trapped in the nodes, creating the desired pattern. The deformation height is extracted from the calculation and a semicircle space is used to approximate the interface deformation. As the acoustic energy increases, the convex shape may become more salient and finally form a jet.

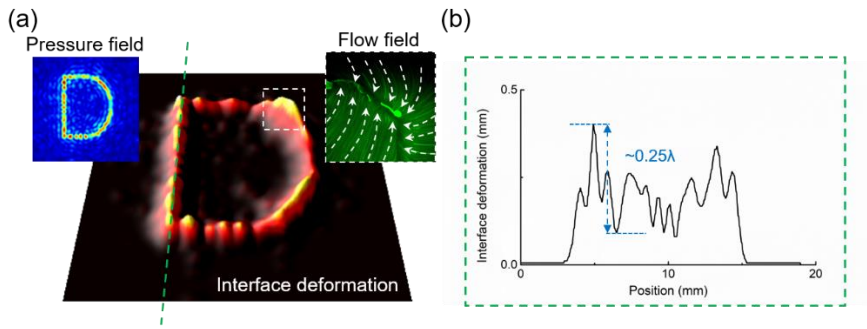

Figure 2.5: Acoustic field and flow field within the deformed space. (a) The simulated acoustic field and liquid-air interface deformation. Insets: left: the pressure distribution, right: zoomed-in particle trajectory showing the flow field (frequency: 1.65 MHz, particle: 2.07 μm PS particle). (b) The height of the interface deformation along the green dashed line.

Here, we will give a detailed introduction of the mechanism of interface deformation and further discuss the related phenomenon. The exact level of surface deformation consists of components proportional to the linear and quadratic terms in the acoustic amplitude(Bertin et al., 2012; Metherell et al., 1969). The deformation can be expressed in terms of the linear wave equation:

$$\left(\Delta - \frac{1}{c^2}\frac{\partial^2}{\partial t^2}\right)\mathrm{U} = 0 \tag{2.12}$$

Where U is the velocity potential and the velocity $\boldsymbol{v} = \nabla U$, the acoustic pressure can be derived as:

$$p = \rho_0 \frac{\partial U}{\partial t} \tag{2.13}$$

Thus the energy density in the field can be obtained:

$$\varepsilon = \frac{\rho_0}{2}(\nabla U)^2 + \frac{\rho_0}{2{c_0}^2}\left(\frac{\partial U}{\partial t}\right)^2 \tag{2.14}$$

The energy flux density f:

$$f = p \cdot \boldsymbol{v} \tag{2.15}$$

During the calculation, it is assumed that no acoustic energy is transmitted to the air, which means the normal component of energy flux vanishes at the interface(R. K. Mueller, 1971). And the interface deformation $\mathrm{d(x,y,t)}$ is derived from the hydrostatic state.

$$\mathrm{h(x,y,t)} = \mathrm{h}_i - h_0 \tag{2.16}$$

where h_i and h_0 are the deformed interface height and static height. The velocity of the liquid which is normal to the hydrostatic interface is:

$$\mathbf{v_z} = \frac{\partial \mathrm{h}}{\partial \mathrm{t}} \tag{2.17}$$

So that the deformation can be derived by:

$$\frac{\partial U}{\partial z}_{h=h_0} = \frac{\partial \mathrm{h}}{\partial \mathrm{t}} \tag{2.18}$$

Due to the energy flux is 0 at the interface, we can get:

$$(f_z)_{h=h_0} = \rho_0 \left(\frac{\partial U}{\partial t}\right)_{h=h_0} \left(\frac{\partial U}{\partial z}\right)_{h=h_0} = 0 \tag{2.19}$$

Since the $\frac{\partial U}{\partial z}_{h=h_0}$ is not 0, we can easily find that:

$$\left(\frac{\partial U}{\partial t}\right)_{h=h_0} = 0 \tag{2.20}$$

The equation $\frac{\partial U}{\partial z}_{h=h_0} = \frac{\partial \mathrm{h}}{\partial \mathrm{t}}$, relates the surface deformation to the acoustic field U, by the integration of it, we can obtain:

$$\mathrm{h}(\mathrm{x}, \mathrm{y}, \mathrm{t}) = \mathrm{h}_1(x, y) + \mathrm{h}_2(x, y, t) \tag{2.21}$$

with

$$\mathrm{h}_2(x, y, t) = \int \frac{\partial U}{\partial z}_{h=h_0} dt \tag{2.22}$$

And the time-independent function $\mathrm{h}_1(x, y)$ is an "integration constant" that we shall determine. In order to get this component, we firstly consider the interface at equilibrium conditions. Here, gravitation and surface tension are acting to restore the plane interface, while this restoration force is normal to the interface and can be indicated as an equivalent pressure p_s:

$$p_s = -\rho_0 g h + \gamma \nabla^2 h \tag{2.23}$$

Thus, the time-independent component on the interface can only exist if the acoustic field exerts a corresponding pressure that can balance p_s. This balancing pressure is equal to the time-average energy density differential across the surface. Since we assume zero energy transfers across the interface, the differential is equal to the energy density at the interface:

$$p_r = \frac{\rho_0}{2}\left(\frac{\partial U}{\partial z}\right)^2_{h=h_0} \tag{2.24}$$

Therefore, the equilibrium condition meets $p_s + p_r = 0$, and the time-independent component corresponds to the acoustic field. Thus, we can derive the relationship between the steady deformation and acoustic field:

$$\left(\nabla^2 - \frac{\rho_0 g}{\gamma}\right) h_1 = -\frac{\rho_0}{2\gamma}\overline{\left(\frac{\partial U}{\partial z}\right)^2_{h=h_0}} \tag{2.25}$$

which can also be applied to the pressure equilibrium equation (Eq. (1)). Then, through Fourier Transform, we can get:

$$\rho_0 \mathrm{g}\mathrm{H}(k_x, k_y; z_s) + \gamma({k_x}^2 + {k_y}^2)\mathrm{H}(k_x, k_y; z_s) = P_r(k_x, k_y; z_s) \tag{2.26}$$

where the $P_r(k_x, k_y; z_s)$ is the Fourier Transform of the acoustic radiation pressure. Using a transfer function to relate the acoustic radiation pressure to the deformation of the interface, we get:

$$\mathrm{G}(\mathrm{k}_x, \mathrm{k}_y; z_s) = \frac{1}{\rho_0 g + \gamma({k_x}^2 + {k_y}^2)} \tag{2.27}$$

where the radiation pressure $\mathrm{p}_r = \frac{p^2}{\rho_0 {c_0}^2}$ fits the air-water boundary condition.

The acoustic streaming is a fluid motion induced by viscous attenuation of acoustic energy during acoustic waves propagate in the bulk liquid(Friend & Yeo, 2011). Since the Reynolds numbers ($Re_{hydro} \equiv (\rho_0 v L)/\mu$, where ρ_0, v, L, and μ are density of the fluid, velocity of the fluid, characteristic linear dimension, and dynamic viscosity of the fluid, respectively) of the vortex streaming in this work do not satisfy the condition of $Re_{hydro} \ll 1$, the perturbation theory-based method is not applicable for solving the acoustic

streaming(Friend & Yeo, 2011). Instead, according to Lighthill's theory, the acoustic streaming is considered as driven by a steady body force **F** generated by acoustic wave propagation, which can be written as(Alghane et al., 2010; Lighthill, 1978):

$$F_x = -\rho_0 \left(\frac{\partial \overline{u_1 u_1}}{\partial x} + \frac{\partial \overline{v_1 u_1}}{\partial y} + \frac{\partial \overline{w_1 u_1}}{\partial z} \right) \tag{2.28a}$$

$$F_y = -\rho_0 \left(\frac{\partial \overline{u_1 v_1}}{\partial x} + \frac{\partial \overline{v_1 v_1}}{\partial y} + \frac{\partial \overline{w_1 v_1}}{\partial z} \right) \tag{2.28b}$$

$$F_z = -\rho_0 \left(\frac{\partial \overline{u_1 w_1}}{\partial x} + \frac{\partial \overline{v_1 w_1}}{\partial y} + \frac{\partial \overline{w_1 w_1}}{\partial z} \right) \tag{2.28c}$$

where ρ_0 is the density of the fluid, and u_1, v_1, and w_1 are the x, y, and z component of time-harmonic acoustic particle velocity ($\boldsymbol{v_1}$). The acoustic streaming can be simulated by considering this external force term when solving the governing equations of steady fluid motion, which are the continuity equation based on mass conservation and the Navier-Stokes equation based on momentum conservation:

$$\rho_0 \nabla \cdot \boldsymbol{v}_{dc} = 0 \tag{2.29}$$

$$\rho_0 (\boldsymbol{v}_{dc} \cdot \nabla) \boldsymbol{v}_{dc} = -\nabla p_{dc} + \mu \nabla^2 \boldsymbol{v}_{dc} + \left(\mu_b + \frac{1}{3}\mu \right) \nabla (\nabla \cdot \boldsymbol{v}_{dc}) + \boldsymbol{F} \tag{2.30}$$

where ρ_0, μ_b, and μ are the fluid density, bulk viscosity, and shear viscosity, $\boldsymbol{v_1}$ is the time-harmonic acoustic particle velocity, and $\boldsymbol{v_{dc}}$ is the steady acoustic streaming as variables of spatial position (x, y, z), and $\boldsymbol{F}$ is the external body force in Eqn. 2.28 relative to $\boldsymbol{v}_1$. One can solve the acoustic streaming $\boldsymbol{v}_{dc}$ based on the governing equations once the acoustic particle velocity $\boldsymbol{v}_1$ is known.

In this work, the acoustic pressure in the 3D fluid domain, p_1, is designed and prescribed. The fluid medium oscillation velocity, $\boldsymbol{v_1}$, can be approximated by $\boldsymbol{v_1} = -\nabla p_1/(j\omega\rho_0)$. The distribution of body force ($\boldsymbol{F}$) can be calculated by knowing the distribution of $\boldsymbol{v_1}$.

The FEM-based software package, Comsol Multiphysics 5.4 (the COMSOL group) was employed for the numerical simulation of acoustic streaming in the 3D fluid field. A predefined "Laminar Flow" physics was used to solve the governing equations of the acoustic streaming problem. The data matrix of body force was calculated by MATLAB as stated above and then imported to COMSOL model to be applied to the 3D calculation domain by adding a "volume force" condition. The boundary conditions on the water-solid interfaces and water-air interfaces were set to "no slip" ($\boldsymbol{u} = \boldsymbol{0}$) and "slip" ($\boldsymbol{u} \cdot \boldsymbol{n} = 0$), respectively. The problem was solved *via* a "Stationary" solver.

2.3.3 Particle force analysis

2.3.3.1 Acoustic radiation force of standing wave field

The acoustic radiation force generated by a standing wave field has been widely studied(Bruus, 2012; Meng et al., 2019). Here, we just simply show the formulas we used to calculate the radiation force in our studies.

The acoustic radiation force on a small spherical particle (ka ≪ 1) in an inviscid fluid can be indicated as the gradient of the Gor'kov potential(Gor'kov, n.d.) U^{rad}:

$$F_{rad_{sw}} = -\nabla U^{rad} \tag{2.31a}$$

$$U^{rad} = \frac{4\pi}{3}a^3\left[f_1\frac{1}{2}\beta_0\langle {p_{in}}^2\rangle - f_2\frac{3}{4}\rho_0\langle {v_{in}}^2\rangle\right] \tag{2.31b}$$

Where $f_1(\beta_p,\beta_0) = 1 - \frac{\beta_p}{\beta_0}$, $f_2(\rho_p,\rho_0) = \frac{2(\rho_p-\rho_0)}{2\rho_p+\rho_0}$.

As the wave reaches the liquid-air interface, the standing wave is formed along with the curved interface deformation. Since the acoustic field in the fluid domain can be considered as the integration of different incident plane wave components, and the liquid-air interface is nearly a perfect reflector due to the large acoustic impedance mismatch between air and liquid, the standing wave field near the interface can be approximately considered as ideal standing wave interference by the incidence wave and reflected wave with $\varphi_{re} = \varphi_{in} + \frac{\pi}{2}$. The acoustic radiation force is found by(Bruus, 2012):

$$F_z^{rad_{sw}} = \frac{\pi k a^3 {p_a}^2}{\rho_0 {c_0}^2}\emptyset(\beta,\rho)\sin(2kz) \tag{2.32}$$

where $\emptyset(\beta,\rho) = \frac{1}{3}f_1(\beta_p,\beta_0) + \frac{1}{2}f_2(\rho_p,\rho_0) = \frac{1}{3}\left(\frac{5\rho_p-2\rho_0}{2\rho_p+\rho_0}\right) - \frac{\beta_p}{\beta_0}$

and the $F_{rad_sw} \propto a^3$

2.3.3.2 Acoustic radiation force of travelling wave field

The acoustic radiation force of travelling wave field is studied firstly by King et al.(King, 1934; Yasuda & Kamakura, 1997) where when ka ≪ 1, the force can be shown by:

$$F_{rad_{tw}} = \frac{2\rho_0 {p_a}^2\omega^6 a^2}{{c_0}^2}\left[\frac{1+\frac{2}{9}\left(1-\frac{\rho_0}{\rho_p}\right)^2}{\left(2+\frac{\rho_0}{\rho_p}\right)^2}\right] \tag{2.33}$$

Later, Yosioka and Kawasima (Yasuda & Kamakura, 1997) expanded this theory by considering the acoustic radiation force on a compressible, spherical particle in an inviscid fluid, which introduces the relationship between the speed of sound in the particle and its compressibility. The force can be shown and widely used by:

$$F_{rad_{tw}} = \frac{2\pi {p_a}^2 \omega^4 a^6}{9\rho_0 \left(2+\frac{\rho_0}{\rho_p}\right)^2 {c_0}^6} \left\{ \left[3 - \left(2+\frac{\rho_0}{\rho_p}\right)\frac{\beta_p}{\beta_0} \right]^2 + 2\left(1-\frac{\rho_0}{\rho_p}\right)^2 \right\} \tag{2.34}$$

where $F_{rad_tw} \propto a^6$

Since in the previous holographic particle pattern (Melde et al., 2016a), the particles are patterned and trapped by an acoustic transparent film on top of the image plane, the acoustic radiation force can also be indicated as considering the viscous fluids due to the top non-slip boundary(Johnson et al., 2016; Settnes & Bruus, 2012):

$$F_{rad_{tw}} = \frac{3\pi a^3 \omega {p_a}^2}{\rho_0 {c_0}^3} \left[\frac{\left(1-\frac{\rho_p}{\rho_0}\right)^2 \left(1+\frac{\delta_\nu}{a}\right)\frac{\delta_\nu}{a}}{\left(1+2\frac{\rho_p}{\rho_0}\right)^2 + 9\left(1+2\frac{\rho_p}{\rho_0}\right)\frac{\delta_\nu}{a} + \frac{81}{2}\left(\frac{{\delta_\nu}^2}{a^2} + \frac{{\delta_\nu}^3}{a^3} + \frac{{\delta_\nu}^4}{2a^4}\right)} \right] \tag{2.35}$$

Where $\delta_\nu = \sqrt{\frac{2\nu}{\omega}}$, and $\nu = \frac{\eta}{\rho_0}$, and $F_{rad_tw} \propto a^3$

2.3.3.3 Spherical isotropic scattering

Skowronek et al.(Skowronek et al., 2013) reported that the net acoustic radiation force applied by the traveling surface acoustic wave on a small particle vanished when $\kappa = ka < 1$ due to spherically isotropic scattering(Destgeer et al., 2014).

2.3.3.4 Hydrodynamic force

The hydrodynamic force on a small spherical particle is widely known as derived by solving the Stokes flow limit for small Reynolds numbers of the Navier-Stokes equations.

For our method, the typic fluid velocity is from 0.1 mm/s to 1 mm/s, and the height of the structure is from 5λ to 40λ. So that we can approximately get the Reynolds number, and the maximum Reynolds number of the different combination of distances and flow velocities is below 10, which is small enough to be considered as laminar flow (Batchelor & Batchelor, 2000; Lamb, 1993; Lighthill, 1978). And the typical Reynolds numbers in the experiment are below or comparable to 1.

Thus, we can calculate the hydrodynamic force by solving the equations:

$$\nabla \mathrm{p} = \mu \nabla^2 v = -\mu \nabla \times \omega \tag{2.36}$$

$$\nabla \cdot \mathrm{v} = 0 \tag{2.37}$$

Where the p, v, μ, ω are fluid pressure, flow velocity, dynamic viscosity, and vorticity, respectively.

For the particle in a far field flow, cylindrical coordinate system (r, φ, z) is used to calculate the force exerted on it (Batchelor & Batchelor, 2000; Lamb, 1993; Lighthill, 1978). Then the flow can be described with a Stokes stream function ψ, which depends on r and z:

$$v_z = \frac{1}{r}\frac{\partial \psi}{\partial r} \tag{2.38}$$

$$v_r = -\frac{1}{r}\frac{\partial \psi}{\partial z} \tag{2.39}$$

Since the z-axis is through the center of the particle and aligned with the mean flow direction, the origin is at the particle center, the flow is approximately considered as the axisymmetric around the z-axis. Here the only non-zero component of the vorticity vector ω is the azimuthal φ:

$$\omega_\varphi = \frac{\partial v_r}{\partial z} - \frac{\partial v_z}{\partial r} = -\frac{\partial}{\partial r}\left(\frac{1}{r}\frac{\partial \psi}{\partial r}\right) - \frac{1}{r}\frac{\partial^2 \psi}{\partial z^2} \tag{2.40}$$

$$\nabla^2 \omega_\varphi = \frac{1}{r}\frac{\partial}{\partial r}\left(r\frac{\partial \omega_\varphi}{\partial r}\right) + \frac{\partial^2 \omega_\varphi}{\partial z^2} - \frac{\omega_\varphi}{r^2} = 0 \tag{2.41}$$

Thus the solution can be found to be:

$$\psi = -\frac{1}{2}vr^2\left[1 - \frac{3}{2}\frac{a}{\sqrt{r^2+z^2}} + \frac{1}{2}\left(\frac{Ra}{\sqrt{r^2+z^2}}\right)^3\right] \tag{2.42}$$

The viscous force per unit area σ, exerted by the flow on the surface of the spherical particle, is in the z-direction everywhere:

$$\sigma = \frac{3\eta v}{2a} \tag{2.43}$$

Integration of the viscous force per unit area over the sphere surface can give the hydrodynamic force according to Stokes law:

$$\mathrm{F}_H = \iiint \sigma\, dr d\varphi dz = 4\pi a^2 \frac{3\eta v}{2a} = 6\pi\eta a v \tag{2.44}$$

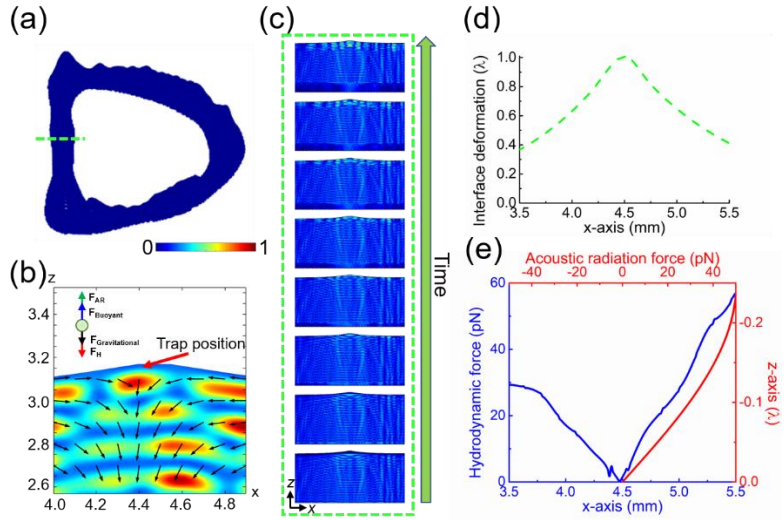

Figure 2.6: Force analysis of immersed particle. (a) The pressure distribution of the deformed space. (b) The Gor'kov potential below the dashed green line in (a), the black arrows show the acoustic streaming flowing toward the deformed space, and particles are trapped at the convex position. (c) The acoustic wave propagation with different time steps showing the wave focusing and localized standing wave. (d) The height of the deformation along the green dashed line in (a). (e) The vertical acoustic radiation force and lateral hydrodynamic force distribution. The two lines intersect at the trapping position where the force equals zeros.

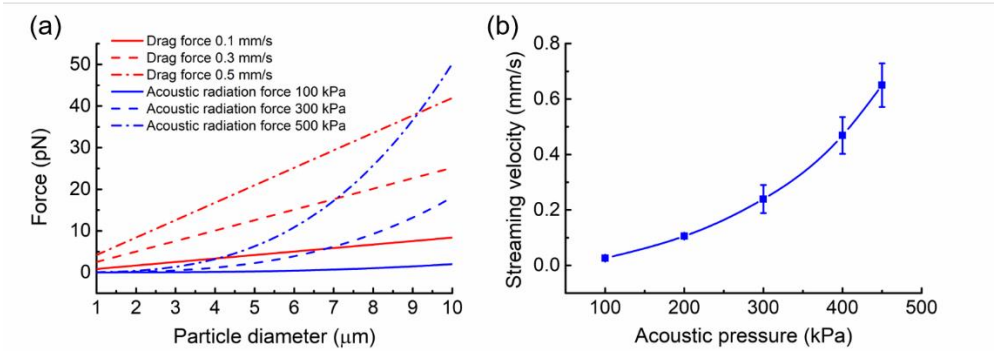

Figure 2.7: Acoustic radiation force and drag force analysis. (a) The typical lateral hydrodynamic force and acoustic radiation force with different measured lateral flow velocities and acoustic pressure. (b) The measured lateral flow velocity with different exciting acoustic pressure.

Meanwhile, the hydrodynamic force and acoustic radiation force of a standing wave are ~10^2-10^4 larger than the radiation force of a traveling wave (Figure 2.6 and Figure 2.7). The model used for calculating the radiation force of traveling wave is based on the M. Settnes and H. Bruus, Phys. Rev. E 85, 016327 (2012), in which the radiation force is proportional to a^3. For the classic model radiation force of traveling wave based on the K. Yosioka and Y. Kawasima, Acta Acustica united with Acustica 5, 167 (1955), the force is proportional to a^6, which will make the calculated force even smaller. Thus, the acoustic radiation force of standing waves and the hydrodynamic force are the two major forces that can provide enough force to manipulate small particles in the liquid.

2.4 Cell patterning using acoustofluidic holography

2.4.1 Two-dimensional cell pattern

As aforementioned mechanism, when the acoustic waves with a specific pressure distribution propagate to the liquid-air interface, it will create a convex space on the interface (See Figure 2.8 for configuration comparison between previous acoustic holographic particle pattern and our method). In this study, the deformation profile is designed to be the specific pattern and can be back derived to the pressure field, then the pressure field is set as the target field for the acoustic hologram. Within the convex space, a localized vertical standing wave can be formed as well as the acoustic streaming keeps flowing into space. Thus, due to the balanced force of acoustic radiation force, drag force,

and gravity, particles can be trapped into the convex area which has the desired shape. The vertical deformation of the water surface h fits the pressure equilibrium equation:

$$\rho_0 gh - \gamma \nabla^2 h = 2p_r \tag{2.45}$$

where ρ_0 is the density of the water, g is the acceleration due to gravity, γ is the surface tension of the water, and p_r is the acoustic radiation pressure. The acoustic radiation can be indicated using the expression given by Gor'kov(Gor'kov, n.d.):

$$F_{rad} = -\nabla\left\{V_p\left[\frac{f_1}{2\rho_0 {c_0}^2} < {p_1}^2 > - \frac{3\rho_0 f_2}{4} < \boldsymbol{v_1} \cdot \boldsymbol{v_1} >\right]\right\} \tag{2.46}$$

where $f_1 = 1 - \frac{\rho_0 {c_0}^2}{\rho_p {c_p}^2}$, $f_2 = \frac{2(\rho_p - \rho_0)}{2\rho_p + \rho_0}$, V_p, ρ_p, c_p, ρ_0, c_0 are the volume, density, acoustic velocity of the particle (with the subscript of p), density, and acoustic velocity of the liquid (with the subscript of 0), respectively. p_1 and $\boldsymbol{v_1}$ are the pressure and velocity of the acoustic field.

And the hydrodynamic force resulting from acoustic streaming can be calculated with the measured flow velocity v(Friend & Yeo, 2011):

$$F_H = 6\pi\eta a v \tag{2.47}$$

where η is the dynamic viscosity.

Relying on this mechanism, we have first tested the microparticle pattern using 10 μm polystyrene particles. With acoustic waves turning on, the particles can gradually form the desired pattern near the liquid-air interface with a narrow feature that indicates the high local particle concentration in the patterned area. With the successful particle demonstration, we continue to test the HeLa S3 cells with the same structure. The liquid-

air interface was designed with the shape of four different letters: “D”, “U”, “K”, “E”. After the acoustic waves excited, cells are also able to be patterned as the prescribed shape (Figure 2.9). During the experiment, we also observed that the formed pattern has a feature width smaller than the acoustic field resolution (~$\lambda/2$), which also indicates the cells are tightly concentrated in the deformed space. As the deformed space is a convex shape, cells may be trapped near the tip of the interface, so that the width of the pattern will be smaller (Figure 2.10). This result may indicate the advantages of utilizing the liquid-air interface to pattern the particles: the actual pattern resolution can be higher than the theoretical value, and the local cell concentration can reach a relatively high value as well. On the other hand, since acoustic wave can propagate through the solid structure, it allows us to pattern the cells in a different environment, e.g., petri dish which is commonly used for biological sample handling and also benefit to the follow-up study. Through the experiment, we observed that the modulated acoustic waves can penetrate the bottom of the petri dish and form the desired cell pattern in the petri dish (Figure 2.11). This finding pushes the study a step forward and may benefit the applications in the field of tissue engineering in the future as the arbitrary cell pattern can be formed directly in the petri dish in a contact-free manner. Thus, our next step was to find a way to fix the pattern, so that the cells can be cultured after the pattern. We utilized the 5% GelMa hydrogel which can be gelated using blue light. We have tested the cell pattern within the hydrogel putting in the petri dish. After the acoustic waves are turned on, cells can be still patterned

to the designed shape although the required input voltage will be larger as the hydrogel has a higher viscosity which may hinder the movement of the cells. With the blue light shining for several seconds, the hydrogel will be crosslinked and fix the pattern in the petri dish. And the patterned cells were observed to grow and form the clusters with the prescribed shapes (as shown in Figure 11 and Figure 12).

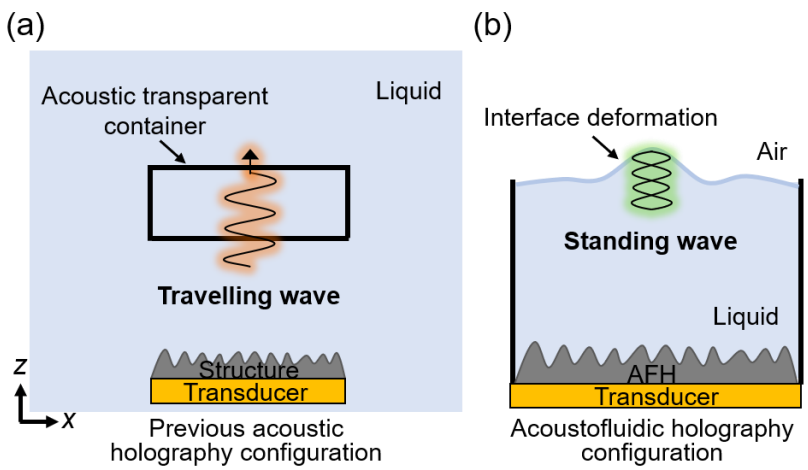

Figure 2.8: Schematic showing the differences in the experimental setups and underlying mechanisms for patterning particles using (a) previously demonstrated acoustic holography techniques and (b) acoustofluidic holography (AFH).

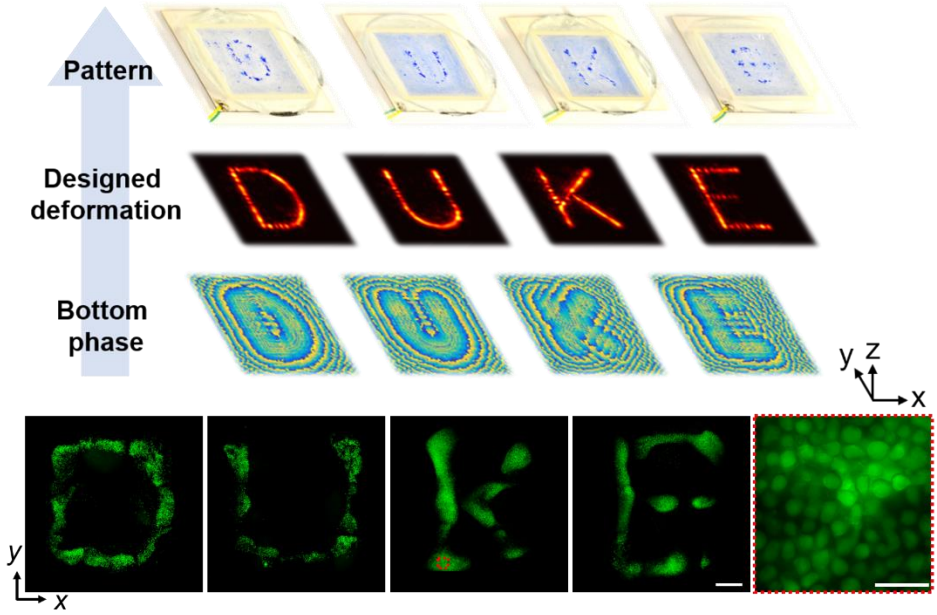

Figure 2.9: Cell and particle patterning *via* acoustofluidic holography. The process illustration and experimental result of the AFH based particle/cell patterning process. When acoustic waves pass through the structure and modulated to certain phase distribution, blue 10 μm PS particles (top row) and cells (bottom row) will be patterned at convex surface deformation positions. Scale bar: 600 μm for cell pattern and 50 μm for zoomed in image.

As the previously described work mainly focused on a large number of cells, we also explored if we could pattern the cells with higher resolution. One straightforward way to increase the resolution is to increase the frequency. We have tested different frequencies during the particle patterning experiment from 1 MHz to 7 MHz and the corresponding structures were designed. However, there is one limitation for high frequency acoustofluidic holographic structure fabrication: the 3D printing resolution

may be insufficient for higher frequency structure. The thickness map of the structure can be calculated by:

$$t(\mathrm{x},\mathrm{y}) = t_o - \frac{\Delta\varphi(x,y)}{k_s - k_l} \tag{2.48}$$

where t_o is the originally settled thickness, $\Delta\varphi(x,y)$ is the calculated phase map, k_s is the wave number of the structure, and k_l is the wave number of the liquid. Thus, with higher frequency, the thickness difference between the pixels that can generate the phase map to specific values becomes smaller. In other words, for higher frequency acoustofluidic holography, the error of the 3D printing especially in the z-axis will have a higher influence on the wave modulation. While for acoustofluidic holography, the phase information covering from 0 to 2π are encoded into the bottom structure, which translates to numerous different thickness steps. In order to generate the high frequency holographic structure, either a higher-resolution fabrication method should be explored, or find a way to simplify the phase information as well as lower the thickness resolution requirements. Thus, we explored a new method called binary phase acoustofluidic holography and demonstrated this method can be implemented to enable new capabilities in higher resolution cell patterning while keeping the simplicity of the fabrication. The detailed calculation procedure was introduced in the last section. Basically, for the binary acoustofluidic holography, the desired acoustic field can be generated using a kinoform that only contains two distinct "bits". These two bits correspond to an acoustic phase of -0.02π and π rad, which represents theoretical binary information of "0" and "1". Through

the simulation, we also found that the selection of the two phases in fact has relatively wide freedom, and the -0.02π is chosen by calculating the average phase value of a phase map derived from the angular spectrum method. The value of each binary pixel can also correspond to the thickness information and the current thickness map only contains two digits as well. Meanwhile, another advantage of using binary acoustofluidic holography is variations in the thickness of the design that shift the phase by multiples of 2π will maintain the bit value. Thus, a sufficiently large difference between two digits can be used to accommodate the 3D printing resolution while maintaining the phase information that can modulate high frequency acoustic waves. With this method, we are able to push the frequency to 15 MHz and fabricate the structure that can fit with this frequency. And in the experiment, a higher resolution cell pattern can be achieved with the width of the feature decreased to one cell. While the pixel width of the structure for 15 MHz is 50 μm ($\lambda/2$), it actually did not achieve the exact single-cell resolution. But as the aforementioned resolution improvement due to the interface deformation, the pattern of the letter "D" can be formed with a high resolution (Figure 2.13). This result indicates the fact that the acoustofluidic holography can possess the potential of the cell pattern with different on-demand resolutions while further development of the fabrication procedure is still needed in order to achieve higher resolution.

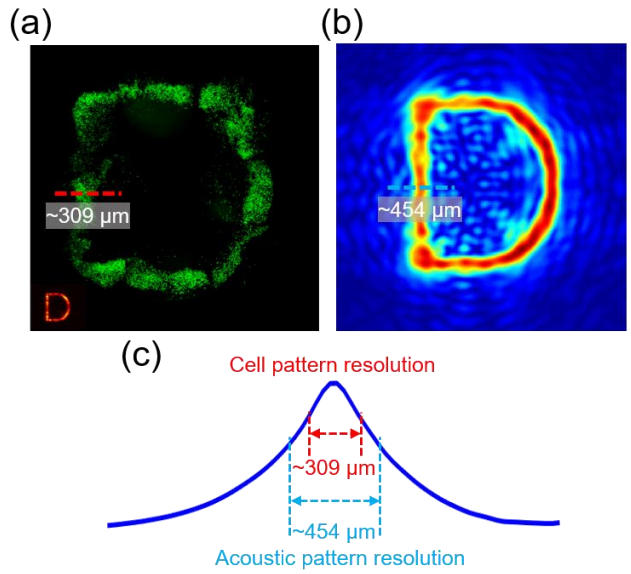

Figure 2.10: The feature width comparison between (a) the actual HeLa cell pattern and (b) the calculated corresponding acoustic field. (c) Comparison between the spatial resolution of the interface deformation and the acoustic pattern. With the interface deformation, cells can be patterned with a width of ~309 µm under an excitation frequency of 1.65 MHz, while for the acoustic field, the minimum feature resolution is half of the wavelength corresponding to ~454 µm.

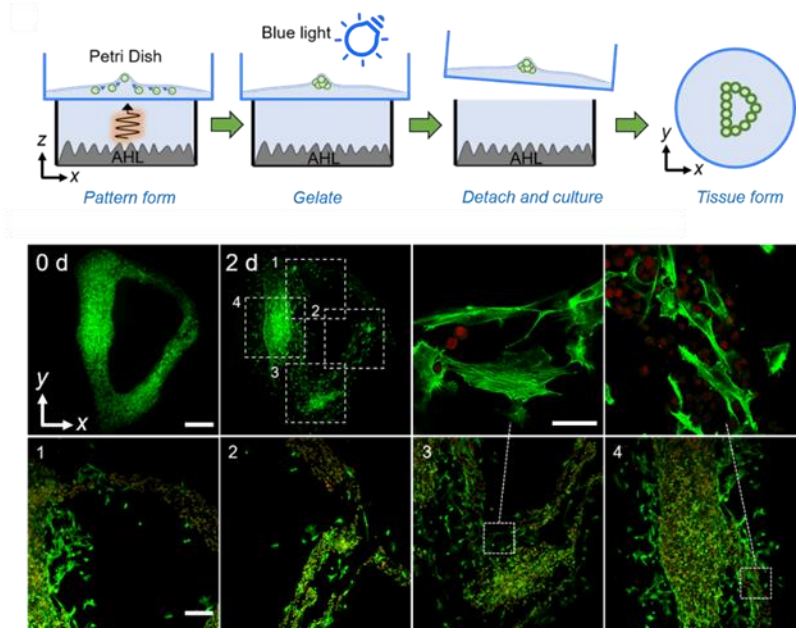

Figure 2.11: Cell patterning in the petri dish. (a) The flowchart of acoustofluidic holography-based cell patterning and culture in a petri dish. The cell sample is first randomly distributed in the hydrogel solution in a petri dish. After the pattern is formed, blue light (~410 nm) is used to gelate the hydrogel. Then the petri dish containing the cell pattern is detached from the structure and put into the incubator for cell growth. (b) The cell pattern right after acoustic wave treatment. (c) The cell pattern after 2 days of culture. Scale bar: 500 μm. Insets 1-4: The zoomed-in confocal images. Scale bar: 200 μm. (d)(e) The zoomed-in confocal images showing the detailed features of the cell pattern. Scale bar: 50 μm.

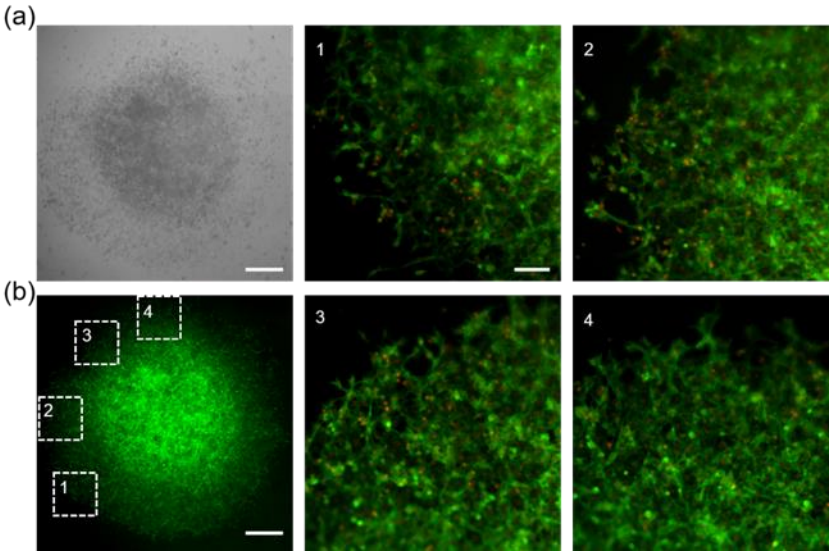

Figure 2.12: Disk shape cell pattern using acoustofluidic holography. (a) The bright-field image of the disk-shaped cell pattern formed by acoustic vortex after 2 days of culture. (b) The fluorescent image of the patterned cells. Insets 1-4: zoomed-in microscopic images showing the features of the pattern. Scale bar: (a)(b) 500 μm, insets: 100 μm.

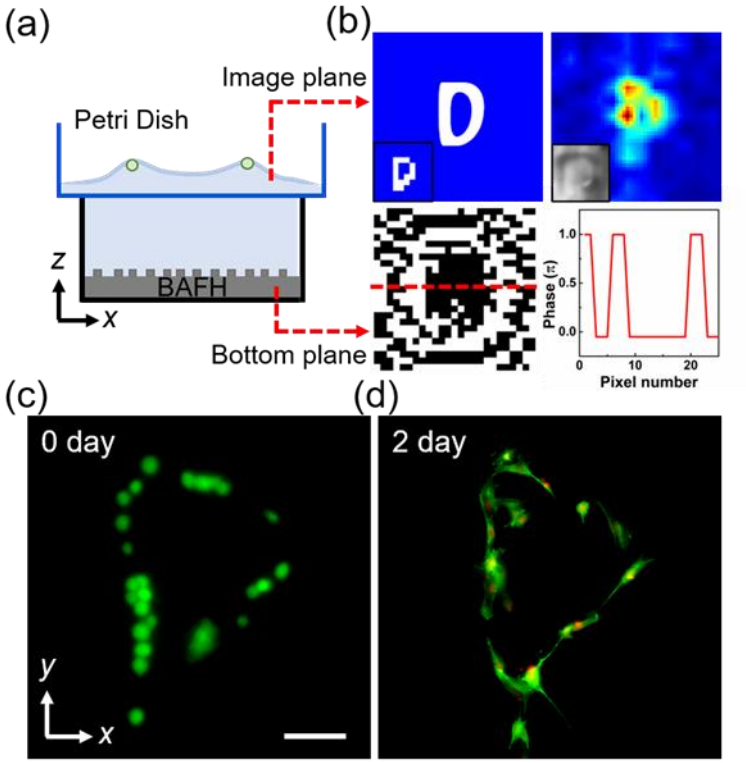

Figure 2.13: Binary acoustofluidic holography for high-resolution cell patterning. (a) Illustration of binary AFH based high-resolution cell patterning. (b) The designed pattern with the letter "D", the bottom phase map includes black and white area corresponding to binary digits. The calculated pressure distribution, binary bottom phase, and phase distribution along the red dashed line are shown respectively. Inset: pixelwise designed pattern (left), a microscopic image of the liquid-air interface (right). (c) The high resolution pattern of the NIH3T3 cells. (d) Cell growth after 2 days. Scale bar: 50 μm.

2.4.2 Three-dimensional layer-by-layer cell pattern

With the basis of the two-dimensional cell pattern, we further demonstrate a 3D cell patterning technology, termed acoustofluidic virtual scaffolds (AVS), that enables the fabrication of complex 3D cellular architectures in a contact-free and biocompatible manner. Using a binary acoustic lens on the path of the acoustic wave propagation, a

complex 3D acoustic field composed of multiple individual 2D patterns can be generated within a hydrogel. By harnessing both the localized acoustic radiation force and fluid motion, cells are patterned in the hydrogel within the convex space near the gel-air interface. As opposed to many current bioprinting methods that must first print the hollow hydrogel structure and subsequently inject cell solution afterwards (Gaebel et al., 2011), here, in our system, cells can be directly patterned with a highly localized concentration by acoustic induced virtual scaffolds. This approach provides a new platform for a 3D cell printing and culture system which will benefit a diverse set of applications in materials science, biology, and medicine.

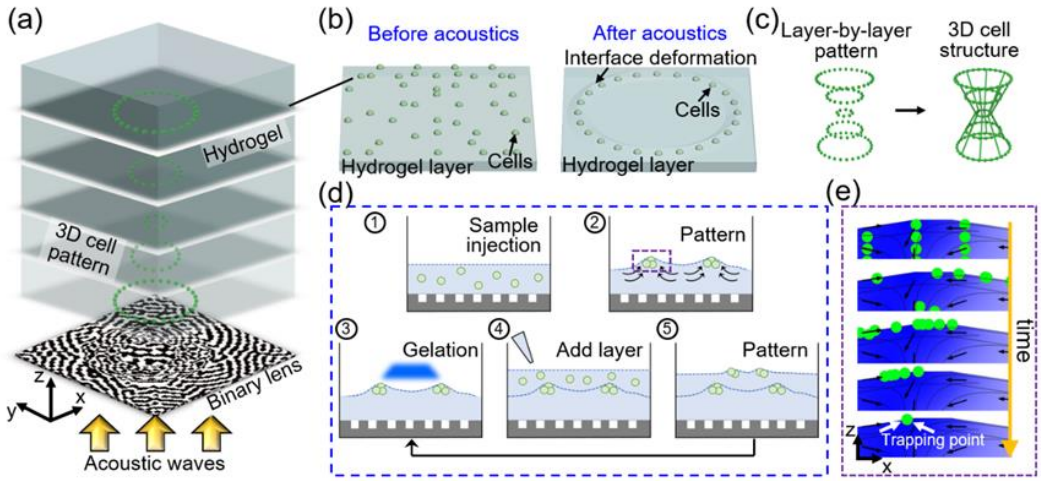

Figure 2.14: Operating mechanism of the 3D acoustofluidic virtual scaffolds (AVS). (a) Illustration of the acoustofluidic virtual scaffolds. The experimental system mainly consists of one acoustic transducer and a binary acoustic lens. A complex 3D acoustic field can be generated through acoustic wave modulation from the binary acoustic lens. Cells inside the pre-hydrogel solution can be patterned into prescribed, arbitrary shapes and form the 3D cell structure. (b) In a single hydrogel layer, before the acoustic patterning, the cells are randomly distributed in the liquid. As the acoustic waves are excited, the acoustic radiation pressure will create the liquid-air interface deformation which contains localized acoustic pressure nodes and fluid motion that can pattern the cells. (c) Schematic showing how the layer-by-layer patterning of multiple 2D cell patterns can generate and form the 3D structure after culture. (d) The operating procedure for 3D patterning *via* AVS. Cells in the pre-hydrogel solution will be injected into the system and patterned to a 2D shape. After the pattern is formed, blue light is used for the gelation of hydrogel solution and fixation of the cell pattern. Then, another layer is added and the next cell pattern is formed. By replicating this process, a layer-by-layer 3D cell structure is constructed. (e) The simulated flow field and particle trajectory in the deformed area, with the help of localized acoustic radiation force and streaming, particles/cells can be guided to the deformed space.

Figure 2.14 illustrates the mechanism of using AVS to construct 3D cell patterns in a hydrogel. A piezoelectric transducer is used to generate incident acoustic waves. As waves transmit through a binary acoustic lens, their phases will be modulated. Hence, the

interference of phase modulated acoustic waves will form complex 3D acoustic fields, which further enables acoustofluidic effects to pattern cells and construct 3D cellular structures. With the binary acoustic lens designed, a 3D acoustic field can be formed with the acoustic signal excitation through the lens. As various specific 2D acoustic fields are encoded into this 3D field with different distances along the z-axis, we are able to generate the 3D cell pattern pipeline in a layer-by-layer manner (Figure 2.14). Specifically, for each layer, the pre-hydrogel solution containing particles/cells is injected into the AVS system and the height of the fluid equals the distance between each target 2D plane. Then, with the acoustic waves, cells can be guided to form the pattern at the liquid-air interface (see Figure 1b for the schematic and Figure 2.14e for simulated particle tracing result). After the cell pattern is stably structured, blue light (405 nm wavelength) is utilized to gelate the pre-hydrogel solution and solidify the pattern layer. The next pre-hydrogel solution layer will be then added on top of the previous layer. While the gelated hydrogel is under the swelling status with the majority of the liquid inside, the bottom layer gel will barely influence the acoustic wave propagation and the cells can continue to be patterned within the newly stacked layers (Naseer et al., 2017; Y. Wang et al., 2018). With an accumulating number of layers, complex 3D cell patterns can be built, and the cells will retain their structure after culture (Figure 2.14c).

In this mechanism, the design of the binary acoustic lens is critical to the construction of the desired 3D cellular structure. Figure 2.15 shows the mechanism for

designing the binary acoustic lens. In order to construct a cellular structure whose architecture is analogous to a target 3D greyscale digital model, this model is discretized into a series of 2D greyscale images (slices) at gradient heights (*i.e.,* z coordinates). Then, by mapping the images' grayscale values to acoustic intensities, a set of 2D acoustic fields will be obtained (Figure 2.15a). Therefore, if our AVS device can generate these acoustic fields, we will be able to construct the desired cellular structure. To generate the target acoustic fields, an acoustic lens composed of a high-resolution pixel array encoded with binary digits (*i.e.,* two distinct phase values) is developed (Figure 2.15b). The digit values at all the array pixels are calculated *via* a direct binary search method (Leportier et al., 2015; J.-P. Liu et al., 2019).

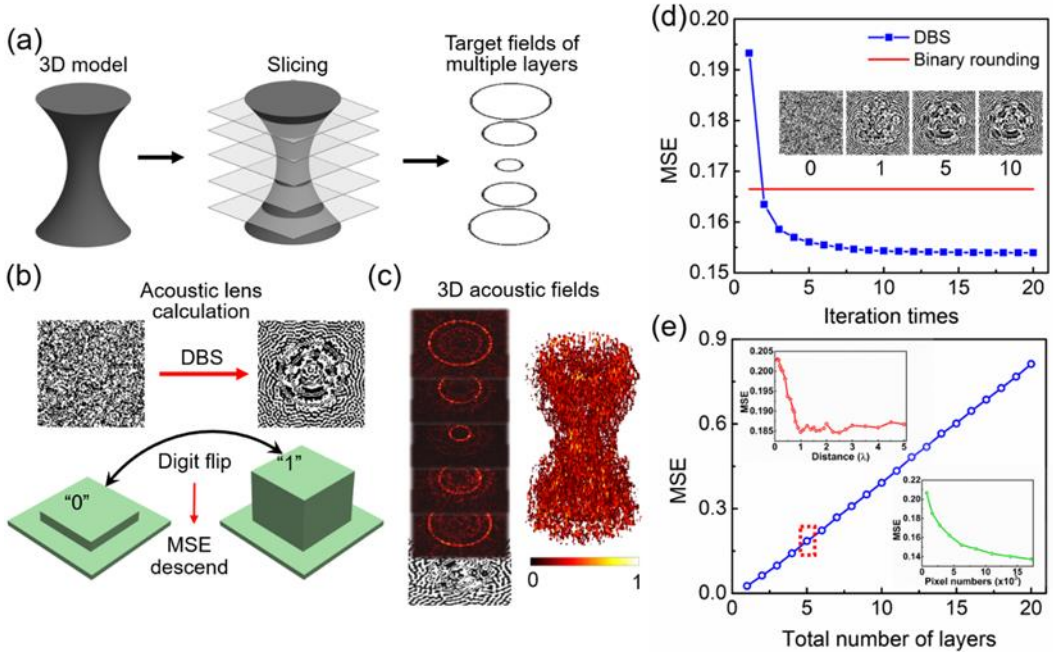

Figure 2.15: Binary acoustic lens design and characterization. (a) The process of the acoustic lens design. First, the desired digital 3D model is sliced with a fixed layer distance to obtain the stacked 2D patterns. Then, the 3D binary acoustic lens is designed with the pressure fields fitting to the generated 2D pattern along different z-planes. (b) The binary acoustic lens is generated by a direct binary search to form the desired 3D acoustic field. With each iteration, every pixel of the lens will go through the trial digit flip to guarantee the mean square error is minimized. (c) The 3D acoustic fields with multiple 2D sections along the z-axis. (d) The MSE calculated with different iteration times. The MSE will become convergent with the iteration times of ~10. The MSE of the direct binary search method is compared to the binary rounding method, the results show with multiple iteration times, the MSE will become smaller than the binary rounding method, which indicates a better fidelity of the acoustic field. Insets: the designed binary acoustic lens with different iteration times (*i.e.*, 0, 1, 5, and 10 iterations). (e) The MSE changing with the layer numbers, the distance between each layer, and the total pixel numbers.

We first investigated the relationship between the calculation cycle, the MSE, and the performance of the AVS system. As discussed above, with more computation cycles, the MSE will decrease and gradually approach the minimum value. As shown in Figure

2.15d, the descent speed of the MSE is decreasing along with the cycle number as well, and the first cycle can reduce ~70% MSE over the total reduced MSE, which shows a quick convergence speed. Meanwhile, we also compared our approach to another algorithm that is commonly used for generating binary holography: binary rounding (Stuart et al., 2014), which will first calculate the common phase distribution covering the phase range from 0 to 2π and then directly round the phase to its nearest binary digit value. Although this method shows a faster calculation process, the acoustic fields show a clear lower fidelity/MSE level compared to the results after two calculation cycles. We also studied the influence of the total numbers of the encoded layers, as shown in Figure 2.15e. For more encoded layers, the MSE will increase along with the number of layers with a nearly linear growth rate. This is understandable as the MSE of the single layer will be convergent to a minimum level, with more layers, the total MSE will accumulate with the number of the layers (*i.e.,* MSE is approximately linearly proportional to the layer numbers). Meanwhile, the settled distance between each layer (slicing interval) also impacts the MSE, while a distance less than one wavelength will have larger errors and the MSE will gradually decrease as the distance between layers increases. This fact highly connects the pattern performance of AVS and the thickness/volume of the fluid in each layer. Although a larger distance between the layers may induce better fidelity, a tradeoff should be made as a larger distance will also impact the cell connection and structure formation between the layers. Furthermore, with a higher number of total pixels, the MSE

can also be minimized as more information can be encoded into the bottom structure and contribute to the 3D acoustic fields.

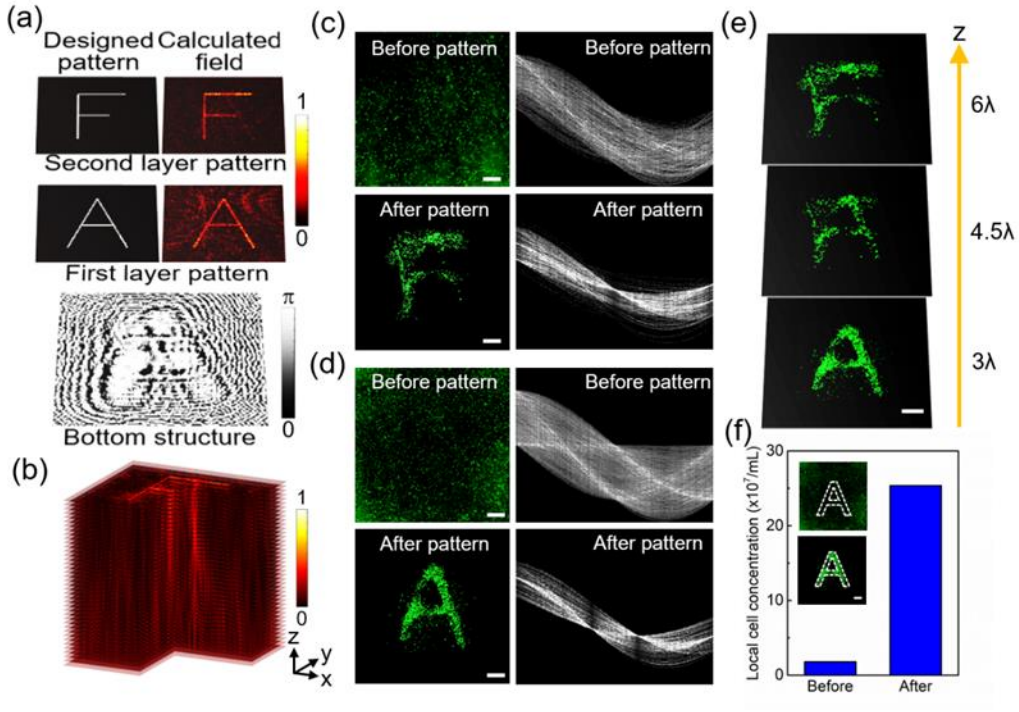

Figure 2.16: Two-layer prescribed, arbitrary cell patterning *via* AVS. (a) Letter patterns with "A" and "F" are designed at different z distances. The bottom structure is calculated and re-projected to the corresponding z-plane with the acoustic fields fitting to the designed pattern. (b) The calculated 3D acoustic fields and cross-section. (c) The fluorescence image and corresponding Hough transform before and after the acoustic patterning for the second layer (*i.e.,* closer to the observation plane). (d) The fluorescence image and corresponding Hough transform before and after the acoustic patterning for the first patterned layer. (e) Experimental results showing the microscopic cell images along different z-planes. Scale bar: 500 μm. (f) The estimated local cell concentration comparison between before and after the patterning. Inset: The fluorescent images with the mask used for local area determination. Scale bar: 500 μm.

With the aforementioned procedure, we validated the AVS patterning technique using a two-layer cell pattern. As shown in Figure 2.16a, we designed the acoustic fields with two target layers which have the intensity patterns of the letter "A" and "F", respectively. Thus, through the acoustic wave propagation, the acoustic fields will gradually change from one letter to another (Figure 2.16b). Within the acoustic lens design, the distance between the layers (also the distance between the lens and first layer) was set to be 3 wavelengths. For the first layer (the layer closer to the acoustic lens), as the fluid is injected into the system and the acoustic excitation is turned on, the acoustic waves impinge on the liquid-air interface and create a stable interface deformation that has the same pattern as the acoustic intensity pattern. Meanwhile, the liquid-air interface will reflect the acoustic waves, which will subsequently interfere with the incident wave. The interface deformation and the reflection form a steady state where a localized standing wave field is formed near the interface and creates the acoustic streaming flow towards the deformation space (Gu et al., 2020; Melde et al., 2016a; R. K. Mueller, 1971). Altogether, cells/particles inside the fluid will be pushed to the deformed space and patterned into the designed shape. In order to validate this mechanism, a theoretical model is developed with which the acoustic streaming induced drag force (F_d) and acoustic radiation force (F_{rad}) are considered in a fluid space.

With the time-domain simulation, particle tracing is conducted and showing the local concentration in the deformed space under the influence of both acoustic radiation

force and drag force (Figure 2.13e). Based on this mechanism, we demonstrated the two-layer cell pattern with the shape of "A" and "F" in the first and second layer respectively. HeLa S3 cells and 5% GelMa solution are used in the experiment. The patterning of the cells is observed under the fluorescence microscope and further analyzed through Hough transform which can identify the features of the fluorescent image. As shown in Figure 2.16c-d, before the acoustics are turned on, the cells in each layer are randomly distributed which corresponds to a Hough transform image with multiple wild curves. After the acoustic patterning, the designed cell shapes can be formed while the Hough transform shows a more organized pattern with multiple crossed curved corresponding to the specific features. We also observed fluorescence images of the cells along the z-axis which can better show the pattern transition from one layer to another as shown in Figure 2.16e. Furthermore, the AVS patterning also enables a higher local cell concentration (~1.78×10^7 cells/mL before the pattern and ~2.54×10^8 after the pattern) as shown in Figure 3f. Here, the "A" pattern scenario was used to calculate the cell concentration as an example. We calculated the mask area (i.e., "A" shape mask that can cover the cell pattern area) and cell counts within the mask. By comparing before and after the AVS process, we observed the local cell concentration has increased about 15 times. This could be beneficial to the cell-cell interaction and bonding after specific patterns are formed.

2.5 Other functions using acoustofluidic holography

2.5.1 Single particle rotation

Besides the cell patterning function we have demonstrated, there are also some other functions and phenomena we have explored with the acoustofluidic holography configuration. One example is single particle rotation/spinning (Figure 2.17). The basic experimental setup is similar to the one used for cell pattern, which includes a fluid container with a kinoform as the bottom, and one acoustic transducer. The pressure field is designed as a vortex shape and will induce a circular shape liquid-air interface deformation with a concave position in the middle. With the acoustic wave, the bulk acoustic streaming was observed to be generated and can drive a floating particle rotation when it is put on top of the liquid. The rotation velocity can be tuned by changing the amplitude of the acoustic wave (See Figure 2.18 for rotation speed analysis). During the experiment, we observe the rotation speed is roughly proportional to the input voltage from ~20 Vpp to ~45Vpp, and beyond this point, the precession of the particle inhibits further improvement of the rotation speed. Based on this interesting phenomenon, we also considered improving the flexibility of the rotation. With two distinct vortex shape pressure distribution encoded into a single structure (Figure 2.17), we may change the direction of the rotation. Specifically, we encoded two vortex shape pressure distribution with clockwise and anticlockwise directions into a single AFH structure by using multiple frequency holography. Thus, the desired pressure field can be excited by tuning the

frequency. In the experiment, 1.65 MHz and 1.75 MHz are used which are two resonance frequencies of one transducer. With 1.65 MHz, the particle can achieve clockwise rotation, while under the 1.75 MHz, the particle will rotate in the reversed direction due to the changed pressure and streaming field.

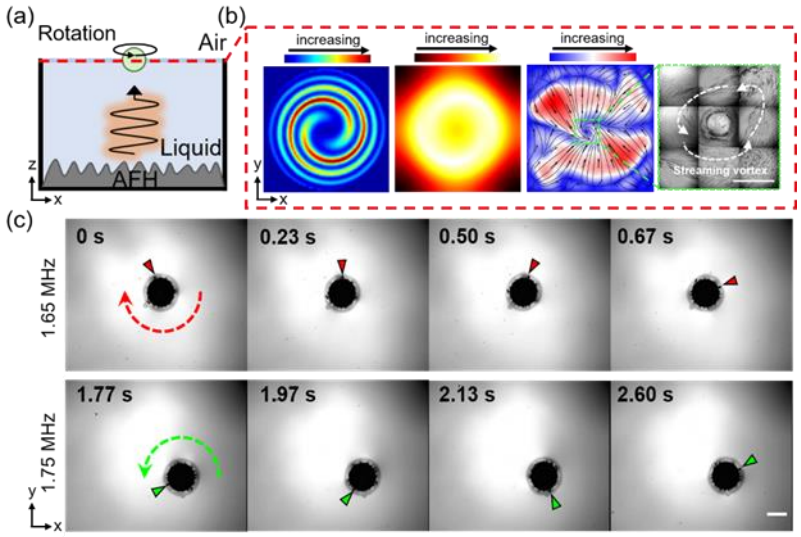

Figure 2.17: Single particle rotation *via* acoustofluidic holography. (a) Illustration of AFH-based single rotation. (b) The corresponding pressure field, interface deformation, and calculated and experimentally observed flow fields. Scale bars: 50 μm. (c) Two different pressure fields are encoded into one AFH structure for reversible rotation. With different frequency excitation, different rotation direction can be initiated. Scale bars: 250 μm.

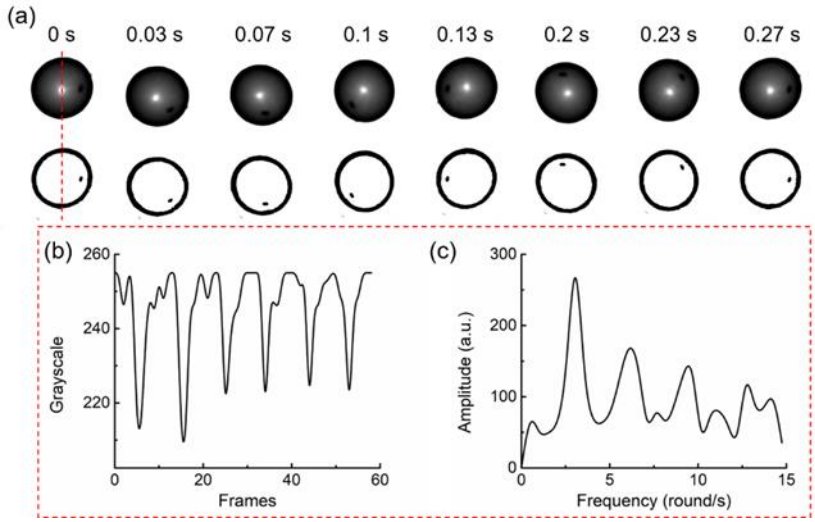

Figure 2.18: Particle rotation speed analysis. (a) The characterization of particle rotation through image processing. With image reslice of the middle line of particle, the rotation can be transferred to the periodic waveform (b), and then derive the RPM through Fourier transform (c).

2.5.2 Particle concentration and separation

Besides the single particle rotation, we were also seeking the opportunity to manipulate smaller particles. One demonstration we conducted is concentrating the particles in micro- and nanoscale in the bulk fluid to a single point. For this function, double-phase holography is used. The detailed calculation method is introduced in the previous section. Basically, both arbitrary phase and pressure distribution are encoded into one structure by decomposing the pressure term into the phase term. Thus, the calculation is transferred to double-phase holography which can modulate the phase term only. With this method, we were able to generate the acoustic vortex with both the vortex phase distribution and the vortex shaped pressure distribution (Figure 2.19). When the

fluid is put into the structure, a three-dimensional vortex streaming is observed in the bulk liquid with both horizontal and vertical streaming. The vertical circulating flow is generated due to the Ecakrt streaming while the angular momentum can also be transferred into the fluid due to the acoustic vortex. With this experiment configuration, two different phenomena can be observed for near field and far-field. With the image plane set in the near field (~5-10 λ), particles can be observed to form the vortex shape pattern. However, when the image plane is set to far-field (~ 40 λ), we found that instead of forming the pattern, particles tend to migrate to the top middle area of the bulk fluid. This phenomenon may be due to the increased attenuation of the acoustic wave at longer propagation distances, and subsequent transfer of energy and angular momentum to the surrounding fluid. Specifically, within the short distance, the acoustic wave can provide enough radiation force for the particle pattern, while for larger image plane distance, the acoustic wave has larger attenuation along the z-axis, and the streaming absorbed more energy from the acoustic waves and has a higher influence on the particle motion. With this effect, the acoustic streaming will bring the particles to the middle area of the liquid-air interface and show a concentration phenomenon. In this configuration, the acoustic waves are more like simulating a stick stirring the liquid. Thus, in order to maintain the curved path of the liquid motion, a centripetal force is needed to direct particles towards the center. Meanwhile, the acoustic radiation force although may not be sufficiently large to pattern the cell, may continuously help to trap the particles near the interface. Based on

this mechanism, we have explored the applications using different particles. We observed that we are able to concentrate or form a disk-shaped pattern with the particles of different sizes and materials, as well as the living matter (E. coli bacteria) which has a self-propulsive force (Figure 2.20). This result indicates the acoustofluidic holography may also be used for the applications such as biosensing, as well as tumor modeling, and cancer therapy as the cells can also be patterned into disk-like shapes and further form the network after the culture. In the experiment, 1.65 MHz acoustic waves were used for the particle concentration with a size larger than 1 μm, while 7.21 MHz was used for the sub-micron and nanoparticles. We have also tested the cell viability to study the influence of the acoustic wave and hydrodynamic effect. Both the concentrated and control cells were tested, showing over 95% viability in the concentrated sample. This result indicates that AFH could be a highly biocompatible manipulation method. On the other hand, as the particles with different sizes may be concentrated with different frequencies or amplitudes, we observed that we can utilize this effect to separate/differentially concentrate the particles as well. When the liquid contains a mixture of particles of different sizes, larger particles moving along the vertical circulating streaming and are able to reach the interface faster. On the other hand, smaller particles may be brought back to the bulk fluid by the circulating streaming, preventing the vertical migration. This trajectory difference creates room for us to separate the particles based on sizes (Figure 2.21 and Figure 2.22). By using different combinations of frequencies and amplitude, we

are able to separate the submicron particles, such as 970 nm and 530 nm, 1 μm and 3 μm, 4.19 μm and 10 μm. With the particles labeled by different fluorescence, we can observe the specific fluorescence getting stronger while the other fluorescence still randomly distributed in the bulk fluid, which indicating the separation/differential concentration happened. This result shows that the AFH may potentially separate the particles based on the size difference or other physical properties. It also opens up the possibility of selectively patterning the particles in a relatively complex medium containing multiple components.

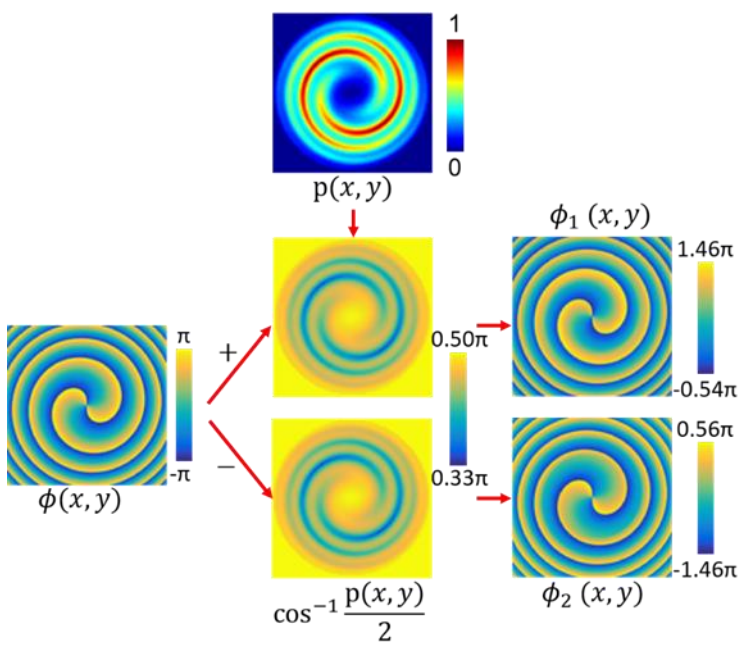

Figure 2.19: The principle of the double phase holography calculation. The desired acoustic field is indicated as: $\boldsymbol{p(x,y)e^{i\phi(x,y)}}$, the amplitude information is transferred to: $\boldsymbol{\cos^{-1}\frac{p(x,y)}{2}}$, then phase one information and phase two information are calculated as: $\boldsymbol{\phi_1(x,y) = \phi(x,y) + \cos^{-1}\frac{p(x,y)}{2}}$, $\boldsymbol{\phi_2(x,y) = \phi(x,y) - \cos^{-1}\frac{p(x,y)}{2}}$.

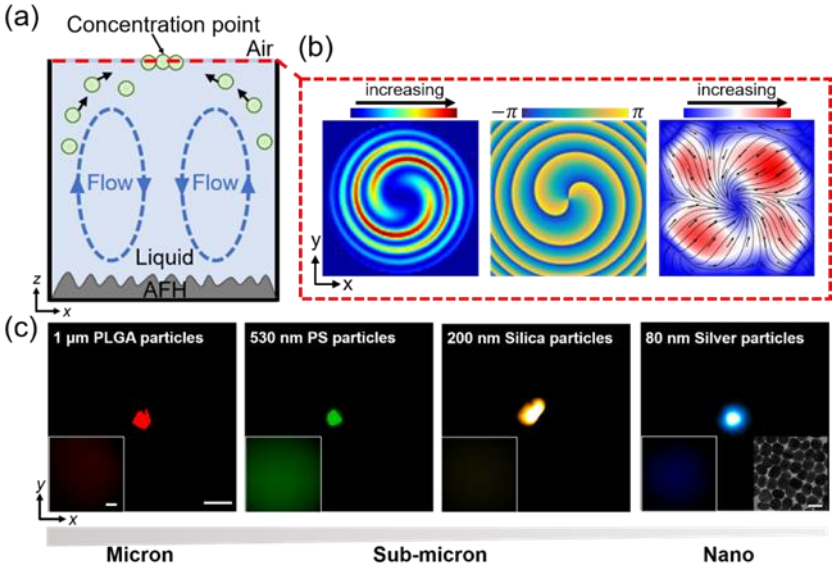

Figure 2.20: Particle/cell concentration *via* acoustofluidic holography. (a) Illustration of the particle/cell concentration mechanism. (b) The corresponding pressure distribution, phase, and flow field of the designed image plane. (c) Fluorescent images showing particles with different physical properties and sizes can be concentrated *via* AFH. Insets: initial states of the particles before the acoustic signal is turned on (left), TEM image of the extracted silver nanoparticles (right). Scale bars: 100 μm for fluorescent images and 100 nm for TEM images.

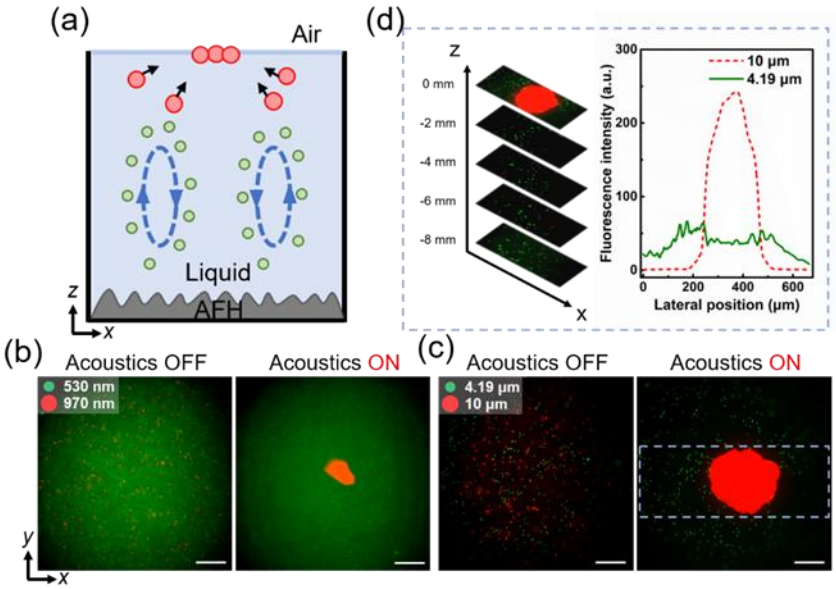

Figure 2.21: Particle/cell separation *via* acoustofluidic holography. (a) Illustration of the selective concentration mechanism. The acoustic radiation force and drag force will applied to the particles based on the size. And larger particles can be differentially concentrated to the middle of the interface. (b) Experimental results showing the separation of 970 nm and 530 nm particles. Scale bar: 100 μm. (c) Separation of 4.19 μm and 10 μm particles. Scale bar: 200 μm. (d) Fluorescent images at different z planes and fluorescent intensity distribution along the lateral axis.

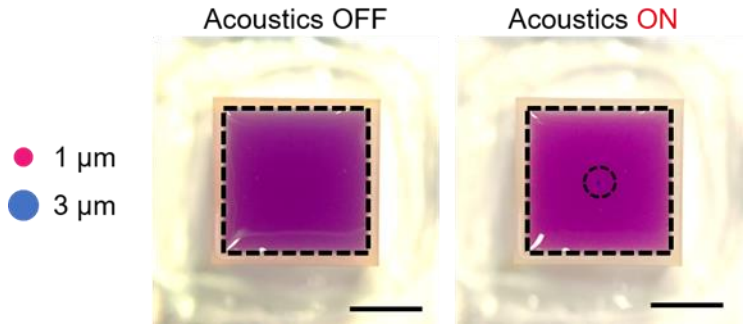

Figure 2.22: Particle separation using acoustofluidic holography. (a) Separation of 1 μm particles and 3 μm particles. Before the acoustic waves are turned on, both 3 μm (blue) and 1 μm (red) particles are evenly distributed in the fluid (left). After the acoustic waves are applied, blue particles are concentrated in the middle area, while the surrounding fluid becomes redder due to the absence of blue particles. Scale bar: 5 mm.

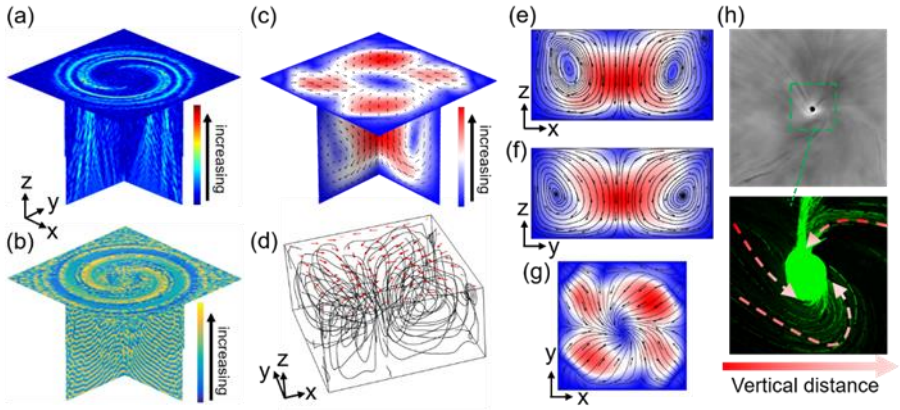

Figure 2.23: 3D flow field characterization. (a) The pressure distributions of x-y, x-z, y-z planes. (b) The corresponding phase distribution. (c) The calculated flow field. (d) The simulated 3D flow field. (e)The flow field of the x-z plane at y/2. (f) The flow field of the y-z plane at x/2. (g) The flow field of the x-y plane at the image plane and simulated particle trajectory. (h) The stacked particle trajectory and zoomed-in fluorescent particle trajectory showing particles moving from lower z-planes to the image plane.

2.6 Discussion and future work

In this study, a multifunctional acoustofluidic holography platform is discussed. Different from the conventional acoustic-based particle manipulation, which utilizes the standing wave fields or complex configurations to manipulate objects, the AFH device has a relatveily small working area with confined boundary conditions, which enables the fluid motion coordinates with complex acoustic fields, and benefit to the particle manipulation in translation and rotation. (See Figure 2.23 for an example of 3D acoustic field and corresponding fluid motion). The combination of acoustic radiation forces by acoustic wave and drag forces by fluid motion provide the capability of manipulating particles with different material properties and sizes, thus can be applied to different potential applications in various fields. Furthermore, with the same configurations, different holography incoorperated fluid motion was explored that may trigger different phenomenon. These techniques include the classic phase holography, which is used for single pre-designed pressure or phase distribution generation, as well as multiple-frequency holography, which is used to initate different acoustic fields with certain frequencies. Meanwhile, double-phase holography is introduced to modulate both the pressure and phase simultaneously, which could potentially bring a higher degree of freedom during the manipulation(M. D. Brown, 2019). Finally, binary holography is utilized to achieve higher frequency holography as well as high-resolution cell patterning. Techniques for high-resolution cell patterning typically require a high standard

fabrication method or complex equipment; however, the binary acoustofluidic holography we presented enables a high frequency wave modulation and high-resolution cell patterning using an easily accessible, low-cost fabrication technique (i.e., 3D printing). As different binary holography studies have been conducted in optics (M. D. Brown et al., 2016, 2014), it has been previously unexplored in acoustic manipulation scenarios. One reason for this discrepancy is that optics can be relatively easily modulated by a photomask or spatial light modulator as they can provide a binarized modulation; however, acoustics face technical challenges specifically due to its strong transmission performance in different medium, thus, leading to difficulties in fabricating a binary amplitude kinoform for underwater acoustics. In our study, we applied a binary phase holography method that focuses on phase modulation and simplifies the fabrication method, thus, shortening the bridge between high-resolution particle manipulation and cost efficient devices.

In addition to the modulation of the acoustic wave using holography technique, the resulting modulated fluid motion (i.e., liquid-air interface deformation and acoustic streaming) is equally important to the performance of AFH. For example, we have demonstrated that liquid-air interface deformation can benefit to the cell patterning. As the liquid-air interface deformation can provides a stable convex space that consist local trapping points where cells can be trapped. Moreover, the interface serves as a natural barrier that prevents the vertical migration of cells away from the patterned area while

the deformation provides a specific geometry that can further aggregate the particles. As a result, the actual cell pattern formed near the interface shows a narrower feature width than the designed acoustic resolution due to the small tip width of the deformation space, leading to a "resolution breakthrough" phenomenon. On the other hand, the interface deformation can also be seen as a type of low-pass filter(R. K. Mueller, 1971) that is able to remove noise from the acoustic field pattern, which, without filtering, typically exhibits roughness in its 2D projection. As such, cell patterns formed in the deformation space are significantly clearer in visualization compared to the acoustic field and particle patterns dominated by radiation forces. Furthermore, the AFH technology has advantages in its ability to not only pattern particles, but also rotate, concentrate, and separate particles. As a result, AFH can be more easily implemented as a robust experimental platform.

For future directions, as 3D cell culture and manipulation are getting more attention, 3D arbitrary cell pattern could a direction that possess great potential in the field of tissue engineering. while much progress has been made over the past decade improving the resolution of extrusion, inkjet, and laser-based bioprinting technologies, each of these approaches faces a fundamental constraint: cells are randomly distributed throughout printed voxels. Without a mechanism for controlling the precise position of individual cells within bioinks, it is difficult to achieve the necessary resolution in the spacing and/or alignment between cells that is critical to ensuring proper tissue functions from the cellular level without using micro-manufactured scaffolds. This microscale level

alignment is critical to the development of functional tissue constructs because architecture and directionality provide the basis for many key tissue functions, such as interwoven sheets of myocardial syncytia and collagen in a laminar architecture of the heart's ventricular wall and rectilinear grids formed by brain's cerebral fiber pathways. An additional challenge facing many 3D bioprinting methods that rely on cells in bioinks is cell sedimentation over time as a result of gravity. This can lead to non-uniform cell distributions and low-resolution features. One way to overcome this issue is through the addition of high-density solutions, such as Percoll, to achieve a state of neutral buoyancy between the cells and the ink; however, these solutions have been shown to influence the cross-linking behavior of the ink, which negatively impacts feature resolution and complicates the calibration of the system. The acoustic method will provide a contactless and biocompatible way to pattern the cells in three-dimensions, which may address the current problems and provide an alternative method for 3D bioprinting.

Chapter 3: Acoustofluidic centrifuge for nanoparticle enrichment and separation

In this chapter, we describe an acoustofluidic centrifuge that leverages the acoustically-driven droplet spinning and enables nanoparticle enrichment and separation. As an example of the proof-of-concept demonstration, this system was employed for DNA molecule concentration and exosome subpopulation separation. The methods and materials, including the device fabrication, sample preparation, and analysis, presented in this chapter sets the foundation for the following chapters. Section 3.1 outlines the motivation of this chapter. Section 3.2 listed the detailed device fabrication, experiment configuration, and sample preparation procedures. Section 3.3 explains the mechanism and theoretical model including the droplet spinning motion and particle motion analysis. Section 3.4 and 3.5 are given on the studies and applications of the single spinning droplet and dual spinning droplet systems. Section 3.6 gives the discussion and further studies. The major work presented in this chapter has been reported in Science Advances.

3.1 Motivation

Nanoparticle manipulation is of great importance in different biomedical and biochemical applications, e.g., gene/drug delivery (H. Lee et al., 2012; Y.-H. Lee & Peng, 2005; Newman & Bettinger, 2007), precision bioassays (Sun et al., 2014; Zhu et al., 2016), cancer diagnosis (Fan et al., 2012; Huang & El-Sayed, 2010; Nash et al., 2012), and catalyzing reactions (Prieto et al., 2013; Stratakis & Garcia, 2012; Zhao et al., 2016). Thus, the capability of conducting concentration or separation, or achieve self-assembly of

nanostructures, has emerged as a prominent interdisciplinary need in various fields. While there is a strong desire to control nanoscale objects (smaller than 100 nm), only a handful of methods can achieve manipulation at this level. Conventional techniques for nanoparticle manipulation include ultracentrifugation (Bekdemir & Stellacci, 2016), nanopore filtration (S. Liu et al., 2013), dielectrophoresis (Xu et al., 2010), magenetopheresis (Kunze et al., 2015), optical tweezing (A. H. J. Yang et al., 2009), and plasmonic tweezing (Roxworthy et al., 2012). While for given applications, each method possess certain advantages, there are still many unsolved issues that arise during their routine use. For example, ultracentrifugation and filtration-based manipulation usually require a long process time while relatively low yields can be obtained; optical and plasmonic tweezers can reach an ultra-high precision, but on the other hand, the throughput would be restricted to manipulating a relatively small number of particles, thus limiting some of the practical applications.

Acoustofluidics (*i.e.*, the fusion of acoustics and microfluidics) based techniques, as an emerging platform, have advantages such as high biocompatibility, versatility, and simple device configuration (Ozcelik et al., 2018). Acoustofluidic methods mainly rely on the acoustic radiation force and acoustic streaming for particle manipulation. Both of the mechanisms can be useful in different applications, especially when dealing with microparticles (Armstrong et al., 2018; Collins, Devendran, et al., 2016; Collins, Ma, et al., 2016; P. Li et al., 2015; Melde et al., 2016a; Patel et al., 2012). However, for nanoscale

objects, there is a fundamental limitation; namely, the acoustic radiation is far insufficient to fully control the nanoparticles (Barnkob et al., 2012; H. Li et al., 2007). One instinctive strategy for dealing with this issue is to find ways to increase the magnitude of the acoustic radiation force. Various previous studies have demonstrated that the acoustic radiation force can be amplified by increasing the frequency or by constructing specialized acoustic resonators. These methods show the capability of sub-micron particle controlling (Limaye et al., 1996; M. Wu, Mao, et al., 2017). Meanwhile, another strategy that is successfully complemented is to increase the secondary acoustic radiation force by seeding the relatively larger microparticles into the fluid, relying on the interactions between the seeding microscale particle and target particles, sub-micron scale control can also be achieved (Antfolk et al., 2014; Hammarström et al., 2012). However, the amplification of the acoustic radiation usually has a limit and would need to explore more advanced and elaborated fabrication procedure. Thus, besides the radiation force improvement, researchers have also shown that harnessing by the acoustic streaming can further improve the manipulation capabilities which adds another controllable force on top of the acoustic radiation forces (Collins et al., 2017; Mao et al., 2017). Although these aforementioned methods can overcome a certain degree of mismatch between acoustofluidic techniques and nanoscale manipulation, most methods remain focused on sub-micron scale (>100 nm) manipulation, and limited studies have been performed on acoustic-based manipulation of nanoscale (<100 nm) bioparticles.

Here, we present an acoustofluidic centrifuge system that leverages acoustically driven spinning droplets to manipulate particles with sizes down to a few nanometers. Various functionalities of this system are demonstrated including nanoparticle concentration, separation, and transport. The idea of this system was originated from the observation of a droplet spinning motion driven by the surface acoustic waves. And the motivation of this study can be divided into two parts: 1. Explore the new physics findings. The liquid droplet study has been utilized as the simplified physical model for numerous fields from the cell nucleus to stellar black holes. While several works demonstrated the droplet spinning using electrical, magnetic, acoustical forces, few studies are indicating the internal particle motion along with the spinning system. 2. Utilize this spinning motion for nanoparticle manipulation. The interaction between acoustics and a sessile droplet has been studied for a long period, most of these works mainly focused on the periodic liquid-air interface deformation or the micro-scale particle manipulation within the droplet. With the spinning motion, the size limit of the manipulated particle can be potentially pushed to the nano-scale, which is of great importance in various biomedical and biochemical applications.

The basic system includes a pair of slanted interdigitated transducers (IDTs) and a circular polydimethylsiloxane (PDMS) containment ring to encapsulate a portion of the droplet and to define its shape (Figure 3.1). We observed an interesting physical phenomenon where surface acoustic waves (SAWs) can drive droplets to spin along their

central axis. This spinning motion initiates Stokes drift along a circular closed path that transfers momentum to the fluid in a manner that significantly increases the inner streaming velocity and shear rate within the droplet by 10 to 100 times. Particles within this "rotational vortex field" are identified to follow a helical trajectory and can be rapidly concentrated to the center of the droplet. Through numerical simulations and experimental investigations, we demonstrate that the liquid droplet spinning can be initiated with a variable sample volume (from nanoliters to microliters), and the nanoparticles of various sizes (from a few nanometers to a few micrometers) can be influenced. Our technology, termed as "acoustofluidic centrifuge", leverages both the acoustically driven droplet spinning and the internal vortex streaming, and achieves the manipulation of the particles with the size down to a few nanometers. Different biosamples are used for the demonstration of the capability, including DNA segments and exosome samples. The theoretical modeling and matching experimental results performed using this new acoustic-mediated nanoparticle manipulation platform can potentially simplify and accelerate various applications e.g., liquid biopsies, vesicle cargo loading, and transfection.

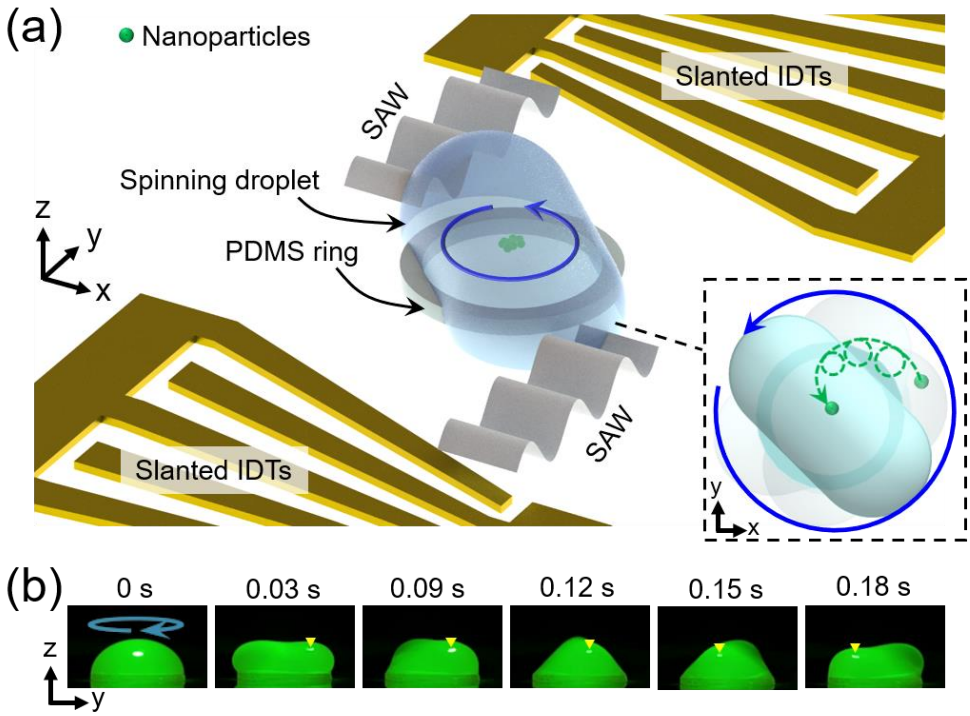

Figure 3.1: Operating mechanism of the acoustofluidic centrifuge platform. (a) Illustration of the acoustofluidic centrifuge system. The droplet is placed on a PDMS ring which confines the fluid boundary and is positioned between two slanted interdigitated transducers (IDTs). Particles inside the spinning droplet will follow helical trajectories (inset) under the influence of both induced vortex streaming and the spinning motion. (b) A sequence of images showing the side view of a 30 μL rotating droplet. The SAW is activated at 0 s. The sequence shows that as the droplet starts spinning, it stretches out to a concave ellipsoid shape, as illustrated in (a). Yellow arrow indicates the reference position that rotates along with the spinning droplet.

3.2 Materials and methods

3.2.1 Device design, fabrication, and operation

The slanted IDTs (5-nm Cr and 50-nm Au) were fabricated on a 128° Y-cut lithium niobite ($LiNbO_3$) wafer (Precision Micro-Optics, USA) using standard photo lithography

followed by electron beam evaporation and a lift-off process. Silver epoxy (MG Chemicals, USA) was used to connect wires to the IDT electrodes. The microchannels were fabricated by standard soft-lithography and a mold-replica procedure. The PDMS rings were cut to the desired size from a 0.55 mm-thick PDMS film using punches (Robbins Instruments, USA). The PDMS parts and $LiNbO_3$ substrate were bonded together after 3-mins of treatment in an oxygen plasma cleaner (Harrick Plasma, USA). Three slanted IDT configurations were used in our setup corresponding to different droplet volume ranges (~10 μL, ~1 μL, and ~100 nL). The first has an electrode finger width and spacing gap which decreases linearly from 140 μm to 70 μm, corresponding to SAW frequencies from 7 MHz to 14 MHz. The second has finger widths from 75 μm to 35 μm, corresponding to 13 MHz to 28 MHz. The third has widths from 32.5 μm to 17.5 μm, corresponding to 30 MHz to 56 MHz. Two function generators (DG 3012C, Teletronics Technology Corporation, USA) and two amplifiers (25A250A, Amplifier Research, USA) were used to activate a pair of slanted IDTs and to generate SAWs. For the acoustofluidic centrifuge system with dual spinning droplets, the microchannel was designed with a width of 200 μm and height of 100 μm(Gu et al., 2021).

3.2.2 Droplet generation and sample preparation.

The micro droplets were generated using a pipette and the nano droplets were generated using 1 μL and 0.5 μL microvolume liquid syringes (SEG, AU). 10 μm, 5 μm, 1 μm, 970 nm, 530 nm, 100 nm, 51 nm, and 28 nm diameter polystyrene particles (Sigma-

Aldrich, USA, Bangs Laboratories, USA) with different fluorescence tags are utilized in the experiments. Deoxyribonucleic acid chains from herring sperm in solution (Sigma-Aldrich, USA) were tested after staining with SYTOX orange dye (Thermo Fisher, USA)(Gu et al., 2021).

3.2.3 Small EV preparation procedure

The exosome sample was isolated from human plasma (Zen-Bio, USA) with a concentration of ~10^6 /mL using differential ultracentrifugation. The general procedure is(Gu et al., 2021):

1. Thaw plasma in a 37ºC water bath until all the crystals of ice in the tubes have disappeared. After thawing is complete, mix the samples by gentle vortexing for 10 sec.
2. Centrifuge 45 mL of plasma at 3,000 g for 10 mins at 8 ºC.
3. Dilute cleared plasma with PBS and spin at 10,000 g for 30 min at 8 ºC. Resuspend and collect 10K pellet in 1.0 ml PBS per tube.
4. Wash resuspended pellets using a 30 min spin at 10,000 g at 8ºC.
5. Spin supernatant at 103,745 g for 4.5 h at 8ºC. Resuspend and collect 100K pellet in 0.5 ml PBS per tube.
6. Combine resuspended plasma 100K pellets (2ml total), add 4 ml PBS, and place on top of a 3-part OptiPrep cushion (2ml 50%/2ml 30%/2ml 10%). Centrifuge at 178,000 g, 2h at 4ºC. Collect 1ml of the 30%/10% interface (ρ=1.06-1.16 g/ml).

7. Dilute OP 30%/10% interface to 12 ml with PBS and spin at 120,000 g for 2 hrs at 8ºC.
8. Resuspend pellets in 200 μl PBS and analyze using NTA for confirmation.

3.2.4 Image acquisition and analysis.

The microscope images and videos were acquired using an inverted microscope (TE2000-U, Nikon, Japan) equipped with a fast camera (Photron, Japan). The droplet spinning motion is captured with a frame rate of 3,000 fps and analyzed using ImageJ (NIH, MD, USA) and MATLAB R2016b (MathWorks, USA). The side view of the droplet spinning was captured using the Slow-Mo mode of a cell phone with a frame rate of 240 fps. The post-processed exosome sample was collected and visualized using transmission electron microscopy (TEM, FEI Tecnai G^2 Twin, FEI Company, USA) and a negative staining method. The nanoparticle size distribution and concentration pre- and post-processing were analyzed using the Malvern Zetasizer (Malvern Instruments, UK) and nanoparticle tracking analysis (NTA) with a NanoSight LM10 apparatus (Amesbury, UK).

3.3 Theoretical model and working mechanism

3.3.1 Droplet spinning motion

The basic experimental configuration of the acoustofluidic centrifuge system consists of a pair of slanted interdigital transducer (IDTs) with a circular thin layer fluid container in the middle. The fluid container is made of polydimethylsiloxane (PDMS) which can hold the bottom part of the fluid. And the resting part of the droplet can form the equilibrium hemispherical shape due to the aligned boundary, surface tension, and

gravity. As the electrical signal is applied to the IDTs, two traveling surface acoustic waves will propagate from two different directions and enter the two flanks of the droplet. Then, the droplet will start to slightly oscillate while the vortex streaming is formed as well inside the drop. With the angular momentum accumulating and the surface tension tends to remain in balance with the centrifugal force, the droplet will enter the stable spinning motion (Figure 3.2). In this stable spinning motion, the droplet gradually deforms into a concave ellipsoid shape and the shape is maintained with a spin speed. Unlike the rigid body rotation, the droplet spinning appears to be a periodic rotational boundary deformation while a "rotational capillary wave" propagating along the free surface of the droplet. Compared to the equilibrium droplet shape before the spin, the spinning droplet appears to be stretched with a lower height and higher maximum equatorial radius. When observing from the top view, the 2D projection of the droplet forms a spinning, two-lobed, elliptical shape and the spinning speed can be obtained via microscopic image processing. Specifically, one line can be drawn along the radial axis in the ImageJ, and through recording the grayscale value of the line, we can obtain a waveform that indicates the fluctuation of the grayscale value. And by compiling the Fourier transform of the waveform, the accurate spinning speed can be obtained. Noting the frequency calculated from the Fourier transform corresponding to twice the actual spinning speed since the two lobes of the droplet will cross the detection line two times each cycle (Figure 3.3). With the measured spinning speed of the droplet with different radius, it is found that the

relationship between the spinning PRM (rotation per minute) and the droplet radius can fit with the classic droplet oscillation model:

$$\omega_n{}^2 = n(n+1)(n-1)(n+2)\frac{\sigma}{r^3\left[(n+1)\rho_{liquid} + n\rho_{air}\right]} \tag{3.1}$$

where n is the spherical harmonic degree which corresponds to the lobe number during the spin, r is the droplet's radius (e.g., the radius of the spherical cap), σ is the surface tension, and ρ_{liquid} and ρ_{air} are the density of the liquid and air, respectively. While this equation was originally derived for free oscillation of a spherical droplet whose shape is repeatedly stretch and contract without spinning, this fitting may result from the similarity between the droplet spinning and standard oscillatory motion: droplet is forced from its equilibrium state and confined mainly by the surface tension for both cases. It is also worth noting that for droplet spinning, part of the droplet stays in the fluid container. Thus, the radius of the droplet can be calculated using the equation:

$$V - \pi a^2 h = \frac{\pi}{3}\left(r + \sqrt{r^2 - a^2}\right)^2 \left[3r - \left(r + \sqrt{r^2 - a^2}\right)\right] \tag{3.2}$$

Where V, a, and h represent the total volume of the droplet, the radius of the PDMS ring, and the height of the PDMS ring, respectively.

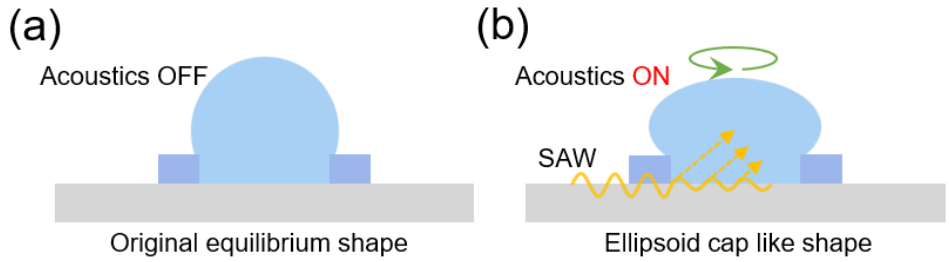

Figure 3.2: Schematic showing the side view of the droplet spinning motion. (a) The droplet stays in its original equilibrium shape when the acoustic is off. (b) When the surface acoustic wave is on, the droplet starts to spin and form the ellipsoid cap like shape.

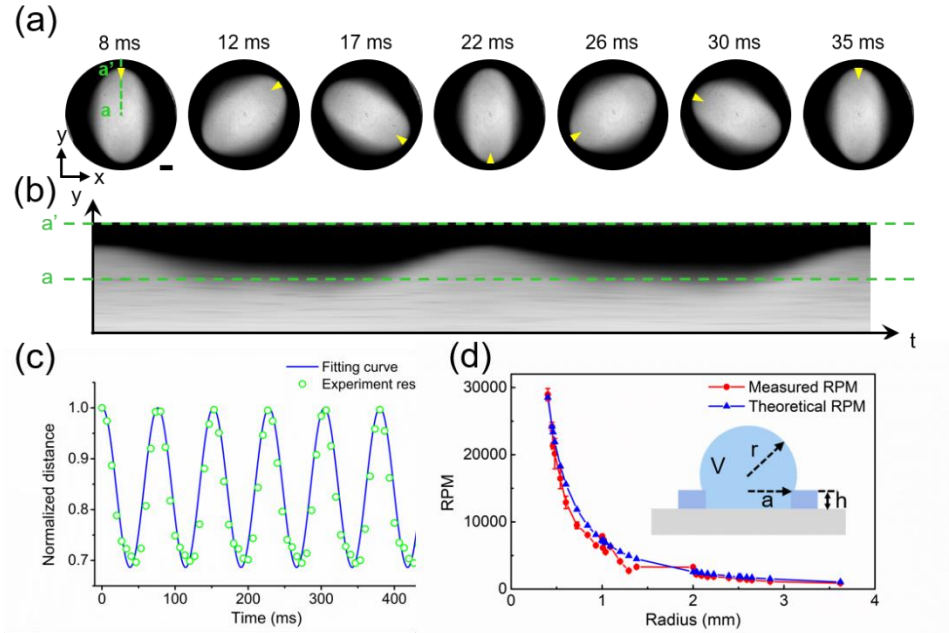

Figure 3.3: Characterization of droplet spin and particle movement in the acoustofluidic centrifuge device. (a) A sequence of images showing the top view of a spinning droplet under a microscope. Yellow arrow indicates a point that spin along the droplet. (b) Corresponding time sequence of stacked images along the line a-a' which shows the periodic grayvalue change of the ellipsoid droplet. (c) The instantaneous velocity at a point on the spinning droplet can be extracted from this normalized fit of the distance change versus time (b). (d) Theoretical and experimental droplet rotation speed (rotations per minute, RPM) versus the change in droplet radius. The volume (V) of the droplet refers to the volume above the PDMS ring.

Meanwhile, we have also studied the potential factors that may influence the droplet spin motion. The first factor is the acoustic frequency, we applied different frequencies from 7.5 MHz to 11 MHz to drive the spin of a 30 μL droplet (Figure 3.4). The results showed that the spin motion can be excited over a wide range of frequencies if the wave can enter the droplet from two directions that have a shift distance with the droplet center axis. And the spin speed (RPM) response is merely influenced by the acoustic frequency. The observation is reasonable, as from the equation of the droplet oscillation, the spin speed is mainly determined by the properties of the droplet (e.g., radius, surface tension). On the other hand, the acoustic power will not influence the spin speed either while the shape of the droplet will be influenced (Figure 3.5). With the increased acoustic power, the droplet will firstly maintain its equilibrium shape and then gradually deforms to the concave ellipsoid shape. While the power further increasing, the droplet will be further stretched and tend to have a larger difference between the major and minor axis. It is also observed that for larger droplet volume, higher-order spin mode may appear during the rotation (Figure 3.6). During the experiment, four- and six-lobed shape droplets are observed during the spinning, while when the power increased, the shape will finally be reverted to two-lobed shapes. The outline of the four spin modes (i.e., 1, 2, 4, 6 lobed) can fit the theoretical model given by:

$$r(\varphi, t) = a[1 + \varepsilon_l(t)\cos(l\varphi + \varphi_0)] \tag{3.3}$$

where $\varepsilon_l(t) = \varepsilon_0 \cos(\omega_l t)$, and a is the equatorial radius of the droplet at its initial equilibrium state, $\varepsilon_l(t)$ and ε_0 are the transient deviation amplitude and its oscillation amplitude, respectively.

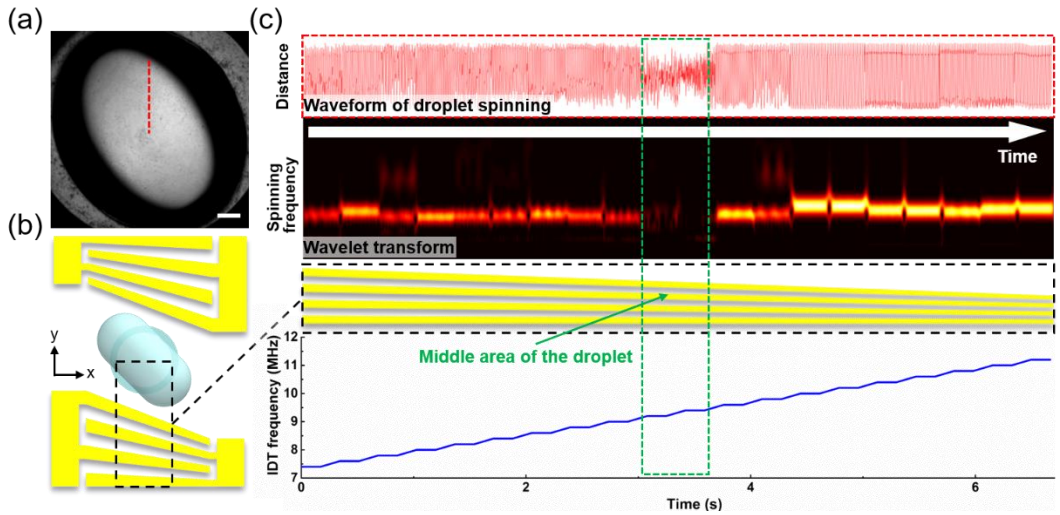

Figure 3.4: The influence of the acoustic frequency on the droplet spin speed in an acoustofluidic centrifuge. (a) The top view of the rotating droplet captured under a microscope. (b) Schematic of the experiment setup, where the slanted IDTs were excited with different frequencies corresponding to different spatial locations along the width of the black frame. (c) From top to bottom: the extracted waveform; the wavelet transforms of the waveform; the enlarged slanted IDT area; and, a plot of the excitation frequency versus time. The results show that frequency tuning has little influence on the droplet spin speed, except when the acoustic wave propagates into the droplet along the central area of the droplet. When the SAW enters the center of the droplet, very little rotation was observed due to a lack of rotational inertia being imparted into the flanks of the droplet.

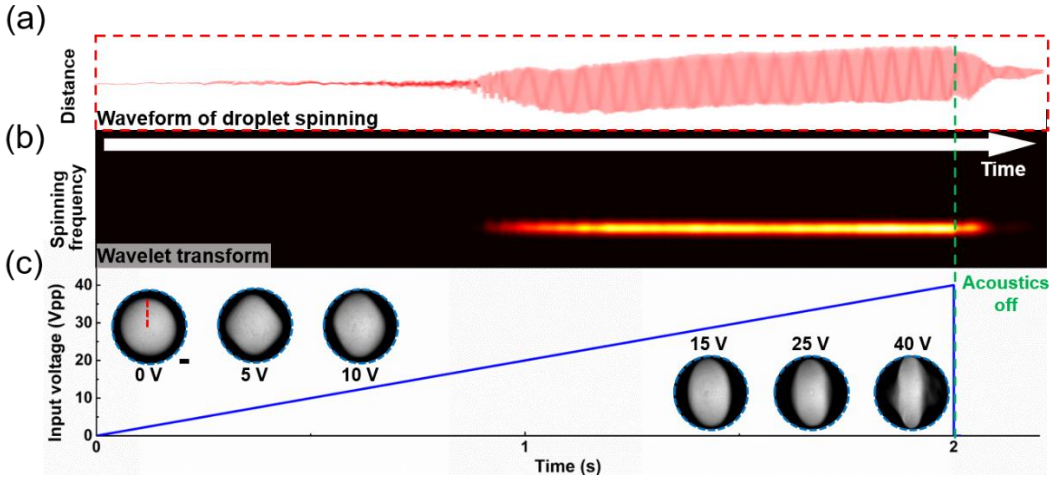

Figure 3.5: The influence of the acoustic power on droplet spin in an acoustofluidic centrifuge. The frequency is set to be 11 MHz, the excitation Vpp is tuned from 0 V to 40 V. (a) The waveform extracted from the spinning droplet. (b) The wavelet transforms with respect to changes in time. (c) Plot showing how the input voltage was varied as a function of time. At different voltages, the droplet starts to rotate from its equilibrium state and forms multiple lobes. As the voltage increased, both the acoustic radiation pressure and the centrifugal force increases, and the droplet gradually becomes a 2 lobed shape while maintaining its spin. Although there is a gradual shape change as the droplet starts to spin, the rotational velocity remains constant.

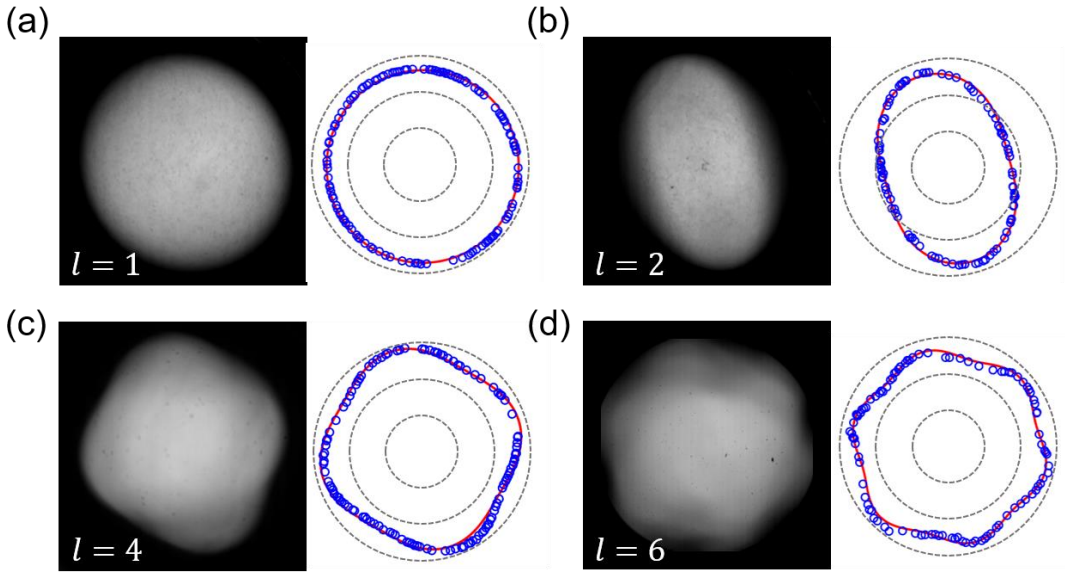

Figure 3.6: Photos (left) and outline comparisons (right) between the droplet (blue circle) and a fitted line (red line) for different droplet spin modes in an acoustofluidic centrifuge. (a) The initial equilibrium shape, (b) 2-lobed shape, (c) 4-lobed shape, and (d) 6-lobed shape, respectively. Red lines show the theoretically calculated outline, and blue circles indicate the experimental results extracted *via* image processing.

Besides the proposed setup in the publication, we have also tested the influence of the material of the fluid container (Figure 3.7). We used the SU-8 to change the original PDMS ring and tested the spinning motion. It is observed that since the SU-8 is more hydrophilic than PDMS, the droplet shape when putting into the container is actually slightly changed. The boundary is self-aligned with the SU-8 ring outer boundary which causes the contact angle larger than the contact angle when the droplet directly contacting the SU-8 layer. Due to the gravity, the droplet shape will be also slightly different from the spherical shape and tending to be flatter. For this case, when fitting with the spinning

PRM with the theoretical oscillation frequency, the radius that being put into the equation can be estimated from the fitting of the droplet top curve. And as measured, the contact angle is positive correlated with the droplet volume while the slop is gradually decreasing due to gravity. Meanwhile, we have also measured the deformation ratio by calculating the ratio between the maximum axis length and the radius of the equilibrium shape (Figure 3.8). With the experiment, it is found that although the deformation ratio will increase along with the input voltage, the increment will gradually decrease. This fits to the intuitive that the deformation extent of a single droplet has a limit and is confined by the surface tension. Another parameter we have explored is the droplet radius. Basically, we put the droplet with different volumes into the same ring, with higher volume, the fitted radius of the droplet will also be larger. And we have measured the deformation ratio along with the droplet radius. It is identified that with a larger droplet radius, the deformation will decrease with an approximate exponential curve. Since the bottom ring has the same size, the surface acoustic wave attenuation on the substrate will be the same. However, the streaming velocity with the same input voltage will be different for different droplet volumes. This result may indicate the spinning motion and the deformation ratio are tightly connected with the internal streaming velocity.

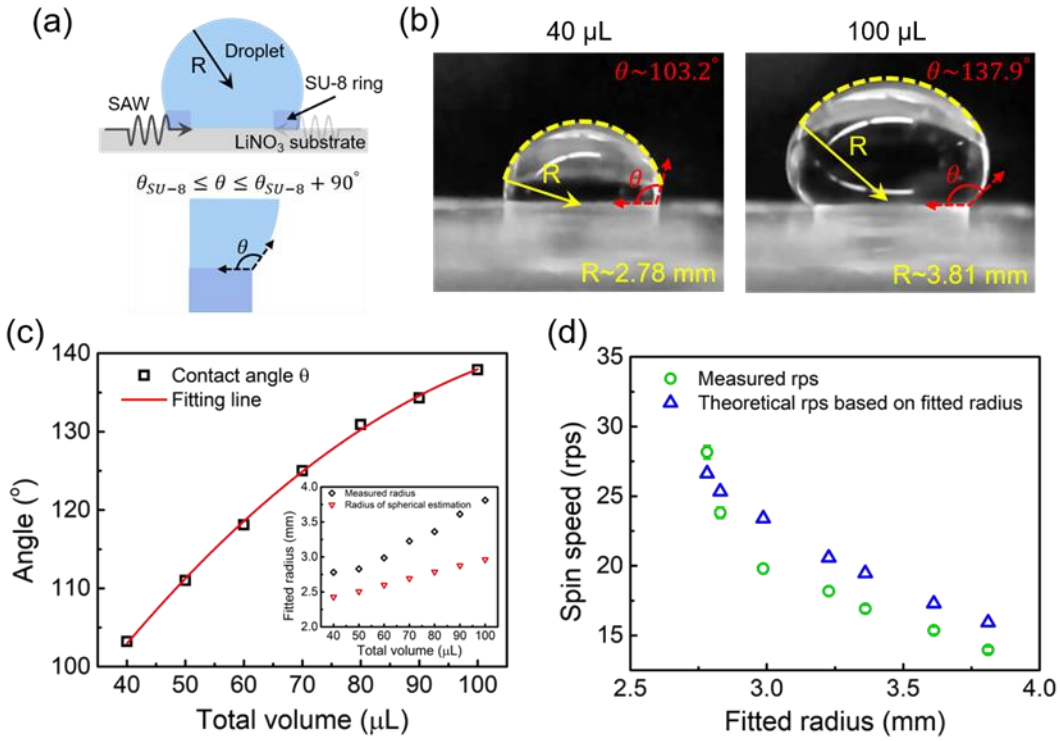

Figure 3.7: The droplet contact angle and spinning speed with a SU-8 ring as the container. (a) The schematic of the boundary-aligned droplet. The contact angle is between the angle for the SU-8 material and the angle for SU-8 plus ninety degrees. (b) Photos showing the droplet contact angle estimation based on the curve of the outline for two different volumes. (c) The relationship between the estimated contact angle and the droplet volume. (d) The comparison between the measured spinning speed and theoretical speed with the estimated radius.

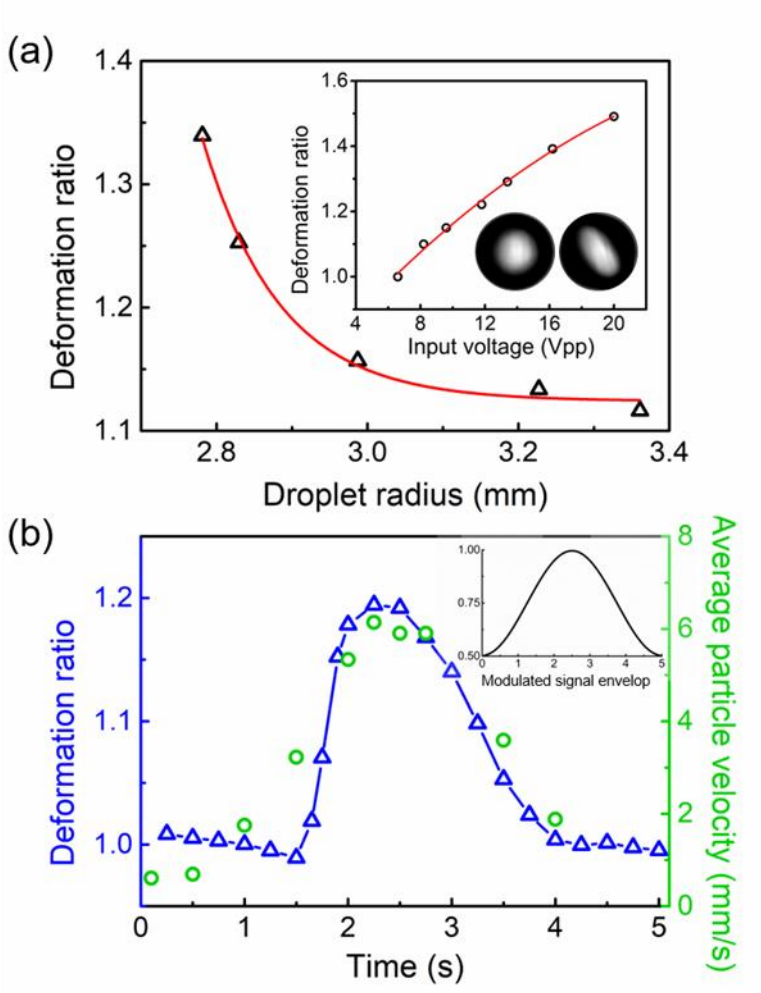

Figure 3.8: The droplet deformation ratio characterization. (a) The deformation ratio for different droplet radius. Inset: With the same radius, the relationship between deformation ratio and the input acoustic voltage. (b) The continuous deformation ratio and averaged particle velocity variation when an amplitude modulated signal serves as an input.

3.3.2 Particle motion in the spinning system

Various studies have shown that microparticles can be concentrated or separated based on the size in a SAW driven vortex streaming inside a droplet. Particles inside this

vortex streaming suffer from the drag force, acoustic radiation force, and shear-induced migration. Within an acoustic driven non-spinning droplet, particles follow the vortex shape trajectory due to the combined force (Figure 3.9 and Figure 3.10). While we have a similar experimental configuration, the droplet spinning in fact adds another factor that can influence the particle motion inside the drop. Unlike the curvilinear particle path, particles in the spinning droplet not only move along the vortex-shape streamline but also move along a small circle during the path, which in other words, follow a helical trajectory (Figure 3.11). This is similar to the Stokes drift effect while the difference from the common case is it is rotating. The spinning motion in fact causes the water wave at the liquid-air interface to propagate along the circular path and results in this rotating Stokes drift. This phenomenon also proves our aforementioned assumption: the spinning of the droplet is different from the rigid body spin, it is more like a continuous interface deformation and the droplet shape is continuously compressing and stretching along a circular path. We used the 1 μm particle to monitor the particle trajectory and analysis the flow field in a spinning frame. By using a fast camera and by analyzing the videos through particle tracking velocimetry, we can detect the helical-shaped trajectory while the particles generally travel along a larger vortex path with various small circular movements along the path (Figure 3.12). For 1 μm particle, they finally will be concentrated to the middle area of the droplet. It is also worth noting that the appearance frequency of the small

circular motion can fit the frequency of the bulk droplet spin, which in other words, one local small rotation corresponds to one large spin cycle of the droplet.

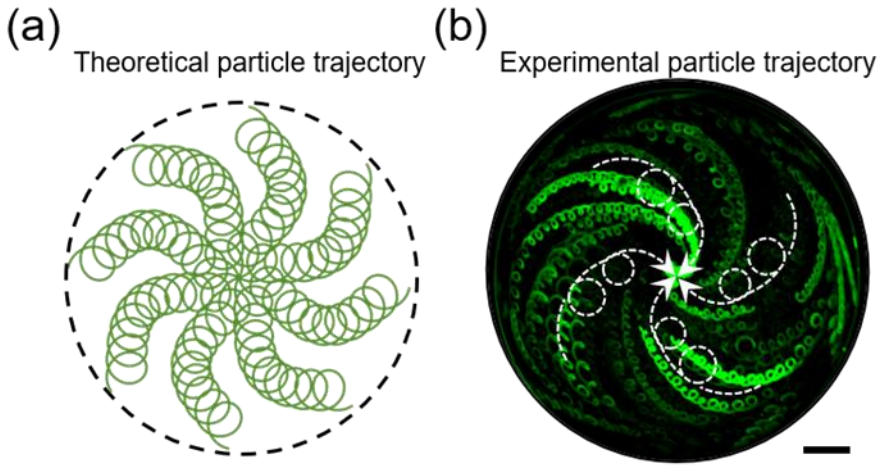

Figure 3.9: Microparticle trajectory inside a spinning droplet. (a) Theoretically calculated and (b) experimentally observed particle trajectories showing the dual rotation modes; particles trace a helical path as they approach the center of the droplet while also rotating around their local axes. Scale bar: 500 μm.

In the process of the exploration, before we have done any nanoparticles, we firstly tested the microparticles. It was found that the microparticles will be concentrated to the middle with an ultrafast speed and the concentration process can barely be observed using the common camera (Figure 3.13). Thus, we utilized the fast camera to capture the concentration process and characterized the velocity of the microparticle. It is found that the particle velocity can reach a very high value. For example, we tested the 10 μm particle within the 20 μL droplet that corresponding to a droplet radius of 2.39 mm and 2741±24

rpm spinning speed. The concentration time was observed to be ~0.12 seconds. This number is ~10 to 100 times faster than previously demonstrated acoustic particle concentration devices. There are two potential reasons for this speed improvement. 1. The input acoustic power. While for the classic sessile droplet system, if larger acoustic power is applied, the droplet will move on the substrate and break the original shape. In the spinning droplet system, the bottom of the droplet is covered by the PDMS ring, and the boundary is aligned with the ring boundary. This boundary alignment provides a larger contact angle and a better fix of the droplet position. Thus, larger acoustic power can be input, and stronger acoustic streaming can be generated. 2. The droplet spinning motion. The spinning can generate multiple effects for the particles inside. For example, during the spinning motion, the angular momentum may be transferred to the fluid and cause stronger streaming velocity. And this continuous interface deformation can generate a higher shear rate and secondary flow effect. During the experiment, we measured the velocity of 1 μm polystyrene particles using digital particle image velocimetry. When the acoustic power is on and gradually increases, the droplet at the beginning struggles to spin under the 15 Vpp (peak-to-peak voltage) excitation and the average particle velocity is measured around 15 mm/s. As the input power increasing, the droplet started to enter the stable spin mode and the acoustic streaming also becomes stronger. It can be observed that the particle velocity has a notable jump with an 18 Vpp excitation voltage which serves as the approximate voltage when the droplet fully enters the spin mode. As the

input voltage is increased to ~40 Vpp, the average particle velocity can reach nearly ~100 mm/s. This velocity is referred to the world coordinate system. While it is difficult to directly compare the particle velocity under the same input voltage between with and without the spin motion, we used the simulation to better understand the relationship of the input voltage and particle velocity for non-spin droplets. As shown in Figure 3.10, when the input voltage is restively low, the particle velocity difference between the spin (experimental results) and non-spin (simulation results) is very minor. However, when the higher voltage is applied, the velocity difference becomes significant and can reach ~80 mm/s. This result indicates the spin will have a positive effect on the streaming and particle velocity.

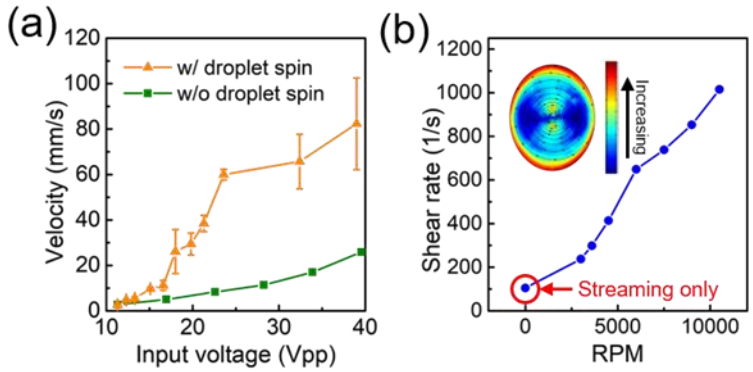

Figure 3.10: Characterization of the internal streaming and shear rate. (a) The streaming velocity with (experimental result) and without (simulation result) droplet spinning. (b) The plot of the calculated average shear rate inside the droplet versus speed. The shear rate increases with a higher spinning speed and rises to several times higher than the shear rate when there is no rotating droplet (streaming only).

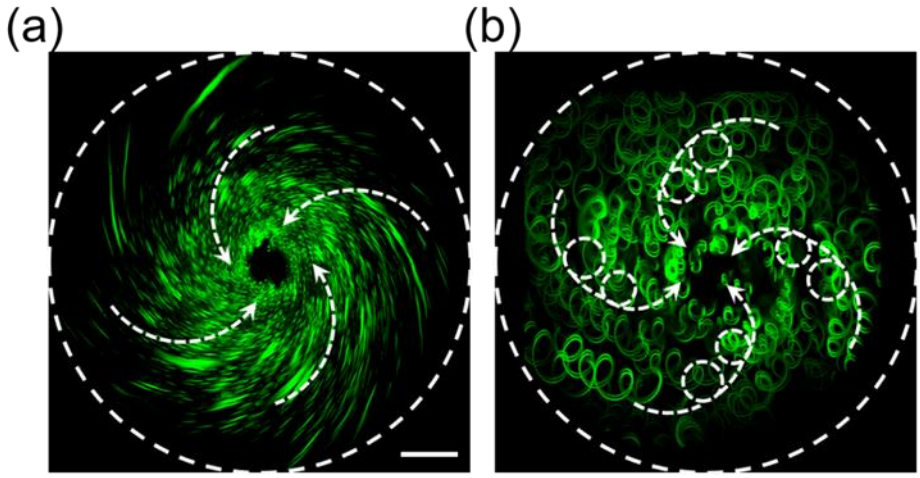

Figure 3.11: Experimentally observed particle trajectories within the droplet in an acoustofluidic centrifuge. Particle trajectories (a) without rotational motion of the droplet where particle motion is due to a small input voltage, and (b) within a stable spinning droplet.

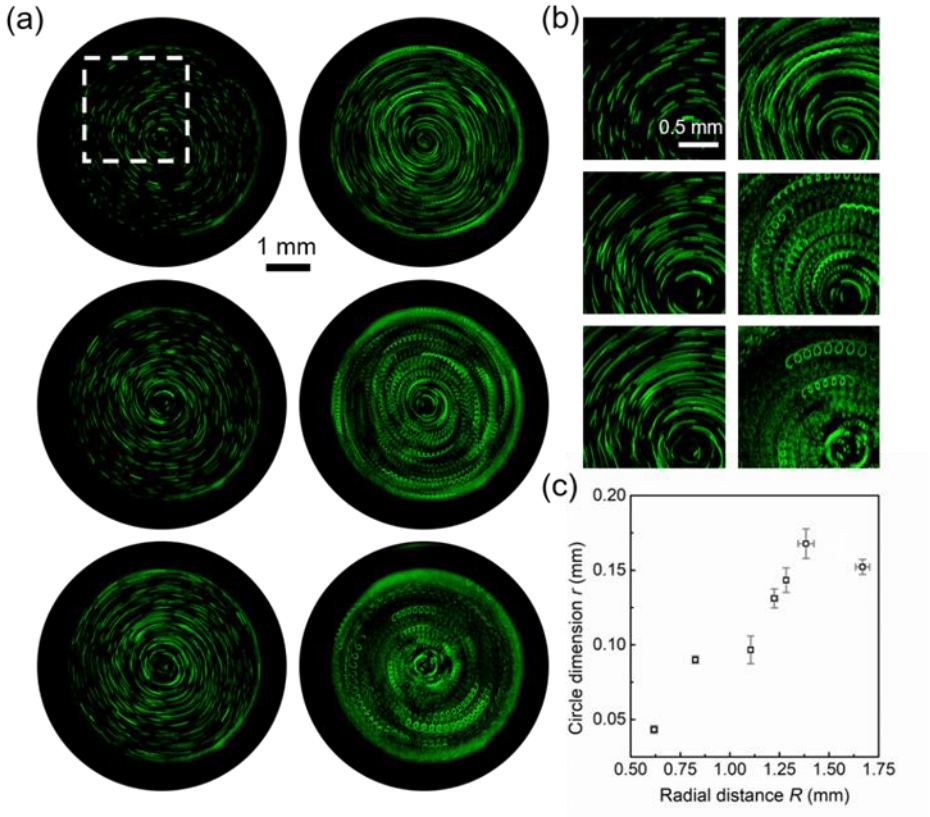

Figure 3.12: Particle trajectory changing with the input voltage increasing. (a) Particle trajectory under different input voltages, with the droplet starts to spin, the particle gradually forms the helical trajectory. (b) Zoomed-in image of the trajectory. (c) Following the helical trajectory, the small circle dimension characterization along with the radial position of the particle.

On the other hand, we found that the particles with a wide range of size from micrometer to nanometer can be concentrated to the middle. There are several potential reasons for this concentration. First, the acoustic radiation force and the shear-induced immigration can provide a portion of the radial force that can push the particles to the middle, and these forces mainly will work for the microscale particles as the magnitude

of the force is comparable to the drag force. It is found that the shear rate inside the spinning droplet can reach a much higher value than the non-spin droplet with pure vortex streaming inside. And the distribution of the high shear rate covers a larger portion of the droplet during the spinning, which may guide the microparticles distributed in the droplet towards the center. Meanwhile, for the nanoscale particles, the acoustic radiation will be far insufficient to directly push the nanoparticle to the center and the shear-induced migration will barely influence the particle motion either. Here the acoustic waves have the function more towards guiding the vortex streaming and drive the spinning motion of the droplet instead of providing radiation force directly on the nanoparticle. Through the simulation, the potential reason for the nanoparticle concentration will be the spinning and vortex streaming induced secondary flow that can lead to the radial movement of the nanoparticles. As the essence of the droplet spinning is the periodic liquid-air interface deformation along the radial axis, this continuous boundary deformation can consistently push the particle into the inner orbit of the vortex streaming and further propel the particle to the middle area. Although the particle displacement has a small oscillation along the radial direction due to the consistent compress and stretch of the droplet, the overall impact can lead to the inward movement of the particle. With this inward pushing effect accumulating, nanoparticles can be concentrated to the center of the droplet. In order to validate this effect, we performed the numerical simulation in a rectangular area whose boundary possesses a similar oscillation

to the droplet spinning (Figure 3.14). Through the particle tracing, the simulation results indicate the particles can be focused to the middle area purely based on the boundary oscillation induced flow. This potentially explains the reason for the nanoparticle concentration. As this effect is difficult to be directly characterized, we assume this secondary flow effect may also be one of the main reasons for the microscale particles.

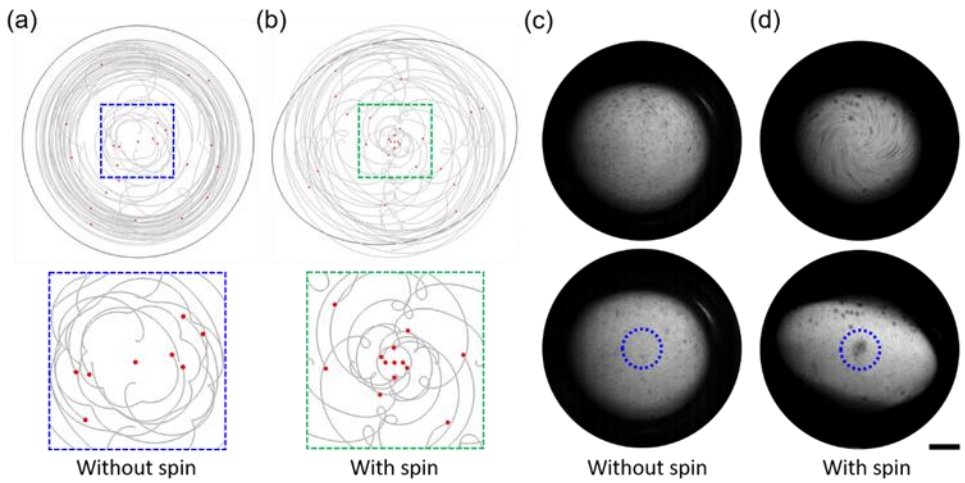

Figure 3.13: Particle motion comparison between non-spinning and spinning droplets. (a, b) Simulated particle trajectory (a) without and (b) with droplet spin. Particle trajectory shows stronger motion towards the droplet center when spinning. (c, d) Experimental particle trajectory (top) and status at 1 second (bottom) for the (c) without and (d) with droplet spinning conditions. Since droplet spin motion is driven by acoustic power, slight power differences are used for without (~5 Vpp) and with (~8 Vpp) droplet spin.

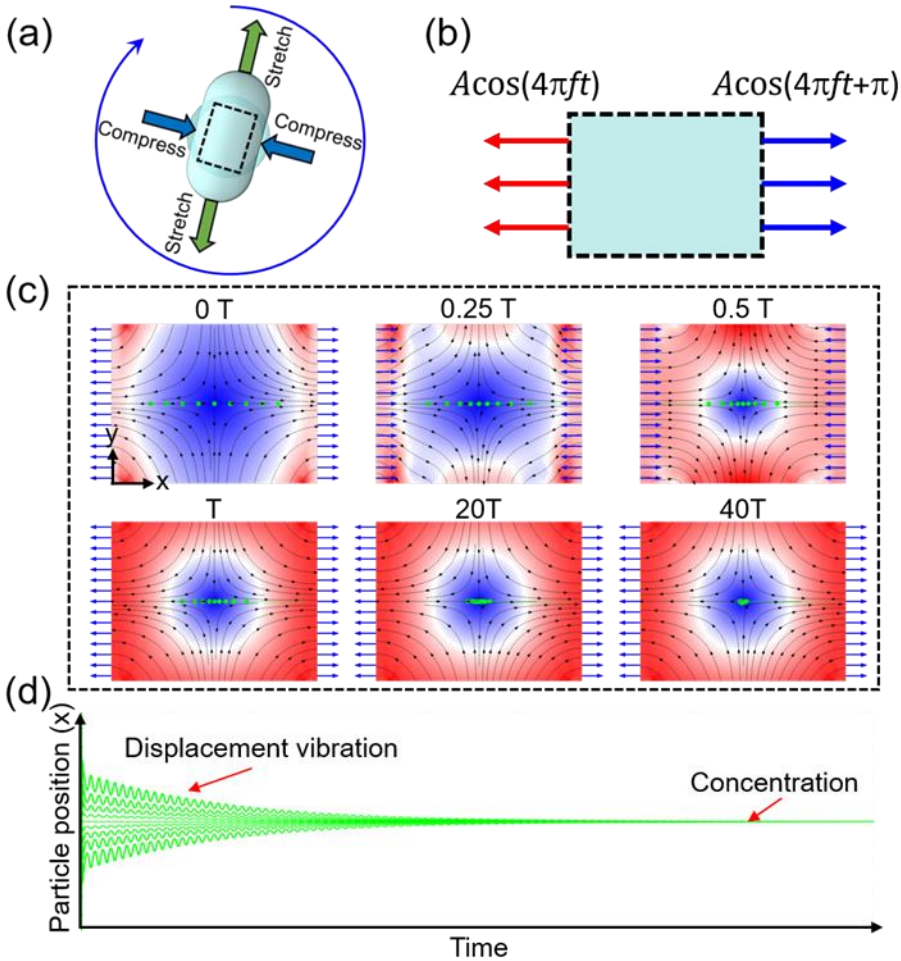

Figure 3.14: Simulation result showing the particle concentration due to the droplet spin and periodic boundary deformation. (a) Schematic of the droplet deformation during spin motion. (b) Boundary condition used for the simplified model simulation. A fluid region in the droplet is simulated with a velocity profile added to two sides of the region (*i.e.,* "velocity" boundary condition). On both sides, the normal outflow velocity is set to be periodic (*i.e.,* $\boldsymbol{Acos(4\pi ft)}$, where $\boldsymbol{A}$ is the velocity amplitude of the periodic deformation, $\boldsymbol{f}$ is the spin frequency which is the half of the deformation cycle along the radial direction) and inverted in order to simulate the flow field during the continuous compression and stretching. The other two sides are set as the "no pressure" boundary conditions. (c) The particle motion under different time frames; with certain spinning cycles, the particles will be focused to the middle of the droplet. (d) Particle position along the x-axis (aligned with the velocity direction) changes as the time varies. With a small displacement vibration, particles are gradually concentrated to the middle region.

More specifically, for the flow field characterization and particle movement, we have conducted various numerical simulations to explore the underlying mechanism. As the acoustic wave propagates into the droplet from its two flanks, bulk acoustic streaming is generated because of the closed volume of the droplet. Acoustic streaming is the time-averaged steady flow that is created as a result of Reynolds stress, where a gradient in the momentum flux forces fluids to flow in association with dissipation of acoustic energy flux. As the droplet spins, a single streaming vortex can be formed inside the droplet. The particle trajectory can be calculated *via* integration of the velocity, which combines the vortex streaming field and droplet spinning motion:

$$\mathrm{x}_{radial} = \int_0^t \mathrm{v}_{drop-radial} + \mathrm{v}_{vortex-radial} dt \tag{3.4a}$$

$$\mathrm{x}_{tangent} = \int_0^t \mathrm{v}_{drop-tangent} + \mathrm{v}_{vortex-tangent} dt \tag{3.4b}$$

And we can derive the droplet spinning velocity by:

$$\mathrm{v}_{drop-radial}(\varphi, \mathrm{t}) = \frac{\partial r(\varphi, t)}{\partial t} = \mathrm{a}[1 - \varepsilon_0 \sin(\omega_l t) \cos(\mathrm{l}\varphi + \varphi_0)] \tag{3.5a}$$

$$\mathrm{v}_{drop-tangent}(\varphi, \mathrm{t}) = \omega_l \mathrm{r}(\varphi, \mathrm{t}) \tag{3.5b}$$

The FEM-based software package, COMSOL Multiphysics 5.4 (the COMSOL group) can also be utilized to calculate the particle trajectory.

We will first discuss acoustic streaming, and introduce how the acoustic streaming and spinning motion influence the particle trajectory and the particle force analysis.

The internal acoustic streaming in the droplet confined by a PDMS ring is governed by equations (Alghane et al., 2010; Lighthill, 1978)

$$\rho_0 \nabla \cdot \boldsymbol{v} = 0 \tag{3.6}$$

$$\rho_0 (\boldsymbol{v} \cdot \nabla)\boldsymbol{v} = -\nabla p + \mu \nabla^2 \boldsymbol{v} + \left(\mu_b + \frac{1}{3}\mu\right) \nabla(\nabla \cdot \boldsymbol{v}) + \boldsymbol{F} \tag{3.7}$$

where the variables $\boldsymbol{v}$ and p are the streaming velocity and pressure in the liquid, and the parameters ρ_0, μ, and μ_b are the liquid density, shear viscosity, and bulk viscosity, respectively. The acoustic streaming is activated by a body force $\boldsymbol{F}$ induced by leaky SAW propagation which is relative to the acoustic particle velocity ($\boldsymbol{v}_1$) following (Alghane et al., 2010; Lighthill, 1978)

$$F_x = -\rho_0 \left(\frac{\partial \overline{u_1 u_1}}{\partial x} + \frac{\partial \overline{v_1 u_1}}{\partial y} + \frac{\partial \overline{w_1 u_1}}{\partial z}\right) \tag{3.8a}$$

$$F_y = -\rho_0 \left(\frac{\partial \overline{u_1 v_1}}{\partial x} + \frac{\partial \overline{v_1 v_1}}{\partial y} + \frac{\partial \overline{w_1 v_1}}{\partial z}\right) \tag{3.8b}$$

$$F_z = -\rho_0 \left(\frac{\partial \overline{u_1 w_1}}{\partial x} + \frac{\partial \overline{v_1 w_1}}{\partial y} + \frac{\partial \overline{w_1 w_1}}{\partial z}\right) \tag{3.8c}$$

The leaky SAW velocity of waves propagating in +y direction can be expressed by(Alghane et al., 2011)

$$u_1 = 0 \tag{3.9a}$$

$$v_1 = i\omega\left(A_m e^{i\omega t} e^{-ik_L y} e^{-\alpha k_L z}\right) \tag{3.9b}$$

$$w_1 = i\omega\left(-i\alpha A_m e^{i\omega t} e^{-ik_L y} e^{-\alpha k_L z}\right) \tag{3.9c}$$

where A_m is the amplitude of substrate vibration, k_L is the wave number of the leaky SAW, and α is the attenuation coefficient, respectively. By substituting Eqs. (3.9) into Eqs. (3.8), the streaming force can be express by

$$F_x = 0 \tag{3.10a}$$

$$F_y = -(1+\alpha_1^2)A_m^2\omega^2 k_i e^{[2(k_i y+\alpha_1 k_i z)]} \tag{3.10b}$$

$$F_z = -(1+\alpha_1^2)A_m^2\omega^2 k_i \alpha_1 e^{[2(k_i y+\alpha_1 k_i z)]} \tag{3.10c}$$

in which $\alpha = i\alpha_1$.

The FEM-based software package, COMSOL Multiphysics 5.4 (the COMSOL group), was employed to numerically solve Eqs. (3.6) and (3.7) which govern the acoustic streaming in the droplet. A predefined "laminar flow" interface was used to solve the equations. The body force in Eqs. (3.10) was applied by adding a "volume force" condition. The boundary conditions on the water-solid interfaces were set to "no slip" ($\boldsymbol{u} = \boldsymbol{0}$), which confines the velocity on the PDMS wall and substrate to be zero. And the boundary condition on the droplet-air interface was set to "slip" ($\boldsymbol{u}\cdot\boldsymbol{n} = 0$; $\boldsymbol{K_n} - (\boldsymbol{K_n}\cdot\boldsymbol{n})\boldsymbol{n} = \boldsymbol{0}$, where $\boldsymbol{K_n} = \mu(\nabla\boldsymbol{v} + (\nabla\boldsymbol{v})^T)\boldsymbol{n}$), which prescribes a no-penetration condition and assumes no viscous effects at the slip wall (COMSOL, 2018). The physics was solved *via* the COMSOL "stationary" solver. The value of some key parameters for the simulation are listed below.

Table 3.1: Detailed parameters for numerical simulations.

Parameter	Symbol	Value
Density of the liquid	ρ_0	997 kg/m^3
Shear viscosity of the	μ	1×10^{-3} Pa·s
Amplitude of substrate	A_m	1.5 nm
Frequency of the SAW	f	13 MHz, 21.7
Major semiaxis of the	R_a	1.5 mm
Minor semiaxis of the	R_b	1.2 mm
Radius of the circular	R	1.29 mm
Rotational velocity of the	f_r	0-55 1/s
Density of the PS particles	ρ_p	1050 kg/m^3
Diameter of the PS	d_p	28 nm, 100
Amplitude of the radial	F_m	0-1×10^{-10} N

For particle trajectory, 2D numerical models were solved using COMSOL Multiphysics 5.4(COMSOL, 2018) to investigate the flow field and particle movement on a horizontal cross-section (xy-plane) of the spinning droplet in an acoustofluidic centrifuge and to examine how the phenomenon responds to changes in parameters of interest (e.g., spin velocity, streaming velocity, shear rate, and particle size). The simulation domain was set to a quasi- ellipse with major semiaxis of R_a and minor semiaxis of R_b for droplets with deformation, or a circle with radius of R for droplets without deformation. The center of the domain was placed at spatial point (0, 0).

A predefined "Laminar Flow" interface was applied to the solution domain to solve the flow field in the domain governed by Eqs. (3.6) and (3.7). The "slip" ($\boldsymbol{u} \cdot \boldsymbol{n} = 0$) boundary, which confines the normal component of the velocity on the boundary to be zero, was applied to the profile of the quasi-ellipse (droplet-air interface). A "Volume Force" condition was added to apply the streaming force generated by two leaky SAW beams propagating in the +y and -y direction into the two flanks of the droplet. The streaming force follows the expression in Eq. (3.11a) and Eq. (3.11b) for +y and -y SAW propagation, respectively:

$$F_y = -(1 + \alpha_1^2) A_m^2 \omega^2 k_i e^{2k_i y} \tag{3.11a}$$

$$F_y = (1 + \alpha_1^2) A_m^2 \omega^2 k_i e^{2k_i (R_a - y)} \tag{3.11b}$$

where A_m is the amplitude of substrate vibration, k_L is the wave number of the leaky SAW, and α is the attenuation coefficient, respectively. The spin motion of the droplet was modeled by applying a "Rotating Domain" condition (under "Moving Mesh" interface). The simulation domain was defined to rotate at a constant speed of f_r revolutions per second. The value of f_r was set within the range of 0-55 according to the experimentally measured value in every single case. The "Laminar Flow" and the "Rotating Domain" interfaces were solved together in the time domain to simulate the flow field induced by leaky-SAWs propagation and spin of the droplet.

A "particle tracing for fluid flow" interface was applied to follow particle motion in the spinning droplet under the forces that might arise. The density and diameter of the

particles were set in the "Particle properties" condition. The density of the PS particles was set to 1,050 kg/m^3 and the diameter of the particles was set to either 28 nm, 100 nm, or 1 μm. The particles were released either randomly using a "Release" condition with setting the number of particles, or regularly using a "Release from Grid" condition with defining the initial coordinates of the particles. The velocity of the particles ($\boldsymbol{v}$) induced by external forces ($\boldsymbol{F_t}$) was governed by the equation $\frac{d(m_p \boldsymbol{v})}{dt} = \boldsymbol{F_t}$. The forces were applied to the particles suspended in the fluid domain. In this case, we mainly considered two external forces, which are the acoustic radiation force and secondary-flow drag force. A "Drag Force" condition was added to apply the component of drag force induced by the flow velocity induced by leaky-SAW propagation and spin of the droplet ($\boldsymbol{u}$). Since the acoustic radiation force and another component of drag force induced by droplet compression and expansion directed towards the center of the domain, a "Force" condition was applied to represent the combined effect of these radial force components. The value of this radial force was adjusted in the range from 0 N to 10^{-10} N for different cases. These physical systems were solved using a time-dependent solver simultaneously with a step of 0.0001 s for 1 μm particles, and 0.000005 s for 28 nm and 100 nm particles. The detailed parameters used in the simulation are listed in Table 3.1.

While for nanoparticles in the spinning droplet system, the dominant force will be the drag force as the flow velocity is large. The common Stokes drag force $F_H = 6\pi\eta r_p v$ is applicable for fluids with relatively low Reynolds numbers (Re < 1) (Karimi & Akdogan,

2012). In a single-droplet acoustofluidic centrifuge system, the fluid velocity is relatively large (in a rotating 30 μL droplet, the typical flow velocity is 40-80 mm/s), which yields a Reynolds number of $\mathrm{Re} = (\rho_{\mathrm{f}} v L)/\mu > 1$ (in a 30 μL droplet, Re is about 40, the maximum Re used in the experiments was ~135), where ρ_{f}, v, L, and μ are density of the fluid, flow velocity relative to the particle, characteristic linear dimension (droplet dimension), and dynamic viscosity, respectively.

Thus, we calculated the hydrodynamic force using the Schiller-Naumann model (Karimi & Akdogan, 2012; Yilmaz & Gundogdu, 2009), which is applicable when $\mathrm{Re} > 1$:

$$F_H = \frac{3\mu C_D Re_r m_p}{4\rho_p {d_p}^2} v \tag{3.12}$$

where $\mathrm{C}_D = \frac{24}{Re_r}(1 + 0.15{Re_r}^{0.687})$, $Re_r = \frac{\rho_f |v| d_p}{\mu}$, and ρ_p, d_p, m_p are density, diameter, and mass of the particle, respectively.

Table 3.2: Force characterization for particle motion in a spinning droplet.

Force	Force magnitude (N)*	Force direction	Formula(Gor'kov, n.d.; Karimi & Akdogan, 2012; Martel & Toner, 2014; Yilmaz & Gundogdu, 2009)
Drag force (vortex streaming)	~0-10^{-10}	Tangential	$\boldsymbol{F}_H = \frac{3\mu C_D Re_r m_p}{4\rho_p {d_p}^2}\boldsymbol{v_T}$
Secondary-flow drag force (droplet deformation)	~0-10^{-11}	Radial	$\boldsymbol{F}_H = \frac{3\mu C_D Re_r m_p}{4\rho_p {d_p}^2}\boldsymbol{v}_R$ $\boldsymbol{v}_R = \frac{\boldsymbol{dR}_{droplet}}{\boldsymbol{d}t}$ $\boldsymbol{R}_{droplet} = (R_{max} - R_{min})\sin(2\pi(2f_{spin})t) + R_{min}$
Pressure gradient force (tangential)	~0-10^{-17}	Tangential	$\boldsymbol{F}_p = \frac{1}{6}\pi d_p^3 \rho \frac{D\boldsymbol{u_T}}{Dt}$
Pressure gradient force (radial)	~0-10^{-17}	Radial	$\boldsymbol{F}_p = \frac{1}{6}\pi d_p^3 \rho \frac{D\boldsymbol{u_R}}{Dt}$
Acoustic radiation force	~0-10^{-15}	Partially radial	$\boldsymbol{F}_{rad} = -\nabla\{V_p[\frac{f_1}{2\rho_0 {c_0}^2} < {p_1}^2 > - \frac{3\rho_0 f_2}{4} < \boldsymbol{v_1} \cdot \boldsymbol{v_1} >]\}$

* The forces are calculated for 100 nm particle in a 10 μL droplet (1.29 mm radius and 55 fps spin speed). Acoustic radiation force is calculated with 21.7 MHz, 300-800 kPa pressure amplitude.

3.4 Single droplet spinning

As the aforementioned mechanism, due to the spinning induced secondary flow, a radial drag force component can gradually push the nanoparticles to the middle. During the experiment, we tested different polystyrene nanoparticle sizes and tried to explore the size limit for the concentration, e.g., 970 nm, 530 nm, 100 nm, 51 nm, and 28 nm. We found that with a different combination of the spinning speed and the acoustic voltage, these

nanoparticles can be concentrated in a relatively short period (Figure 3.15). This rapid concentration capability can lead to various biomedical applications, for example, fluorescence-based biospecimen detection. We further tested the DNA molecules in the spinning droplet system. We mixed the DNA with a fluorescent dye SYTOX that can enhance the fluorescence more than 500 fold when intercalated with the DNA. We prepared the sample with the DNA and SYTOX mixed and put it into the system. As the intercalation happens, the sample can initially express weak evenly distributed fluorescence in the droplet. After the concentration, we can observe a very obvious fluorescent signal in the middle of the droplet and gradually getting stronger as the spinning continuous (Figure 3.16). This result shows the potential of using the acoustofluidic centrifuge system to amplify the fluorescent signal detection for biosamples.

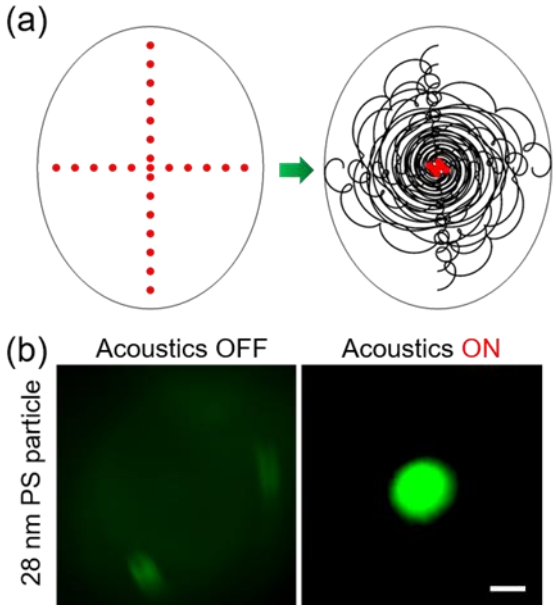

Figure 3.15: Rapid nanoparticle enrichment *via* acoustofluidic centrifuge. (a) Numerically simulated particle trajectory within a spinning droplet before acoustic is on (left) and off (right). (b) Fluorescent images of the 28 nm particle before (left) and after (right) the acoustic field is turned on. Scale bar: 50 μm.

In addition, as the experimental parameters for concentrating nanoparticles with different sizes vary, we are able to utilize this property to differentially concentrate the particles. Specifically, if a droplet containing nanoparticles of different sizes, we can selectively concentrate the nanoparticles with a relatively larger size. This is result from the interplay of the acoustic parameters (e.g., acoustic frequency, amplitude), and droplet spinning speed or radius. Although the nanoparticles may eventually be concentrated to the middle, the time scale and the migration velocity for the concentration will be different. This may result from the different forces that particles suffered in the spinning

droplet. Larger nanoparticles will experience larger acoustic radiation force (neglectable, to some extent), larger drag force, and weaker Brownian motion. For drag force specifically, it dominants the particle motion, and the nanoparticle inside a spinning droplet with vortex streaming, the particle velocity will eventually be accelerated to be the same with the flow velocity, and the larger particle will thus suffer from larger drag force. On the other hand, the secondary flow induced radial force has a similar effect on the particle: force is positive correlated with the particle size. We conducted the experiment and tried to validate this assumption. We prepared the sample with 100 nm and 28 nm particles mixed and put a 10 μL drop of the sample into the system. The droplet has a radius of 1.29 mm and a spinning speed of 3313±35, and the 100 nm particle was labeled as red fluorescent while 28 nm particle was labeled as green fluorescent. While the acoustic is on and the droplet starts to spin, we can observe the red fluorescence start to getting stronger in the middle which indicates the 100 nm nanoparticles are concentrated. On the other hand, the green fluorescence is still randomly distributed throughout the droplet (Figure 3.17). These results show the potential of the single droplet spinning system can perform rapid nanoparticle enrichment as well as the differential concentration when multiple sizes are involved. This may be utilized for biosample detection or specific components detection in a relatively more complex sample environment.

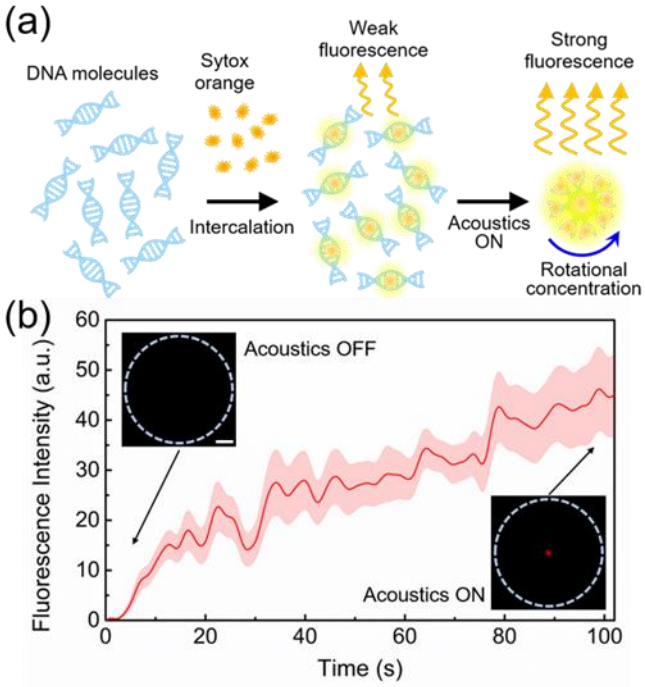

Figure 3.16: Demonstration of the DNA molecules concentration for fluorescence signal amplification. (a) Flow chart showing the process of DNA enrichment and fluorescent signal enhancement in a spinning droplet. (b) Plot of the measured DNA fluorescence intensity versus time in the spinning droplet. Insets: fluorescent images before and after signal enhancement. Scale bar: 50 μm.

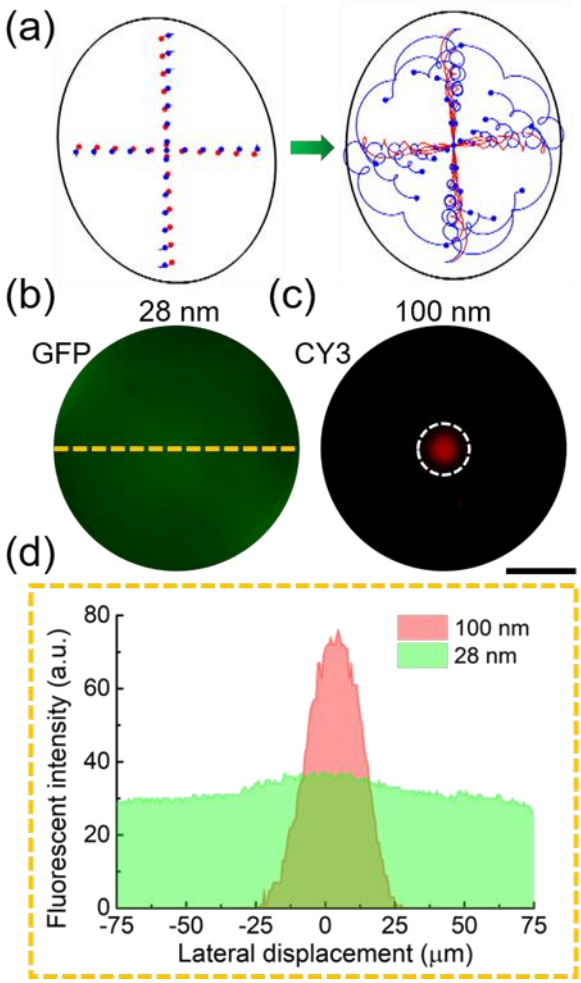

Figure 3.17: Differential nanoparticle concentration *via* acoustofluidic centrifuge. (a) Numerical simulation results showing the difference in nanoparticle trajectories for particles with sizes of 100 nm (Red) and 28 nm (Blue). (c) Microscope images showing the experimental result of the differentially concentration of 100 nm and 28 nm particles. Scale bar: 100 μm. (d) Fluorescent intensity along the axis of the droplet showing the concentration effect on the 100 nm particles.

3.5 Dual droplet spinning

The single spinning droplet may be utilized for the applications that are more toward the detection. In a single droplet, although nanoparticles with different sizes can

be differentially concentrated to the middle and create the spatial separation effect, the retrieval of the subsets of the nanoparticle sample will be difficult. For the applications that need to further conduct downstream analysis, with a single droplet acoustofluidic centrifuge system, it will unavoidably affect the purity of the targeted nanoparticle during the collection step. Thus, we had the motivation to further improve or develop the platform that can have an easier step for sample collection after the separation. In order to address this problem, the first instinct we had is trying to connect two droplets, so that we may separate and transfer the separated particles from one droplet to another. Thus, we have started to consider building a passage between two droplets (Figure 3.18). After the testing of different configurations, we developed a dual-droplet based acoustofluidic centrifuge system. In the system, two individual droplet units can be driven by acoustic waves. Here the benefit of the slanted IDTs becomes more significant: we can excite the IDT with multiple frequencies that spatially localized at different locations so that we can drive the droplet motion at the same time in a controllable manner. The two droplet units are connected with a microchannel in the middle that has sufficient length to avoid the droplet interaction after the spinning. By exciting the surface acoustic waves with four different frequencies, we can have two pairs of the beam that propagating along with opposite directions and drive the spinning of the droplet. These four acoustic beams can be excited with a pair of slanted IDTs with a frequency shift keying function. Basically, we utilized two function generators and amplifiers, and each pair of the equipment taking

charge of one slanted IDT. The frequencies were chosen as the spatial location of the beam entering the droplet can have a shift away from the center axis of the droplet. And two frequencies were shifting back and forth to provide the excitation of the droplet motion. One key part of this configuration is that the fluid motion (i.e., spin and vortex streaming) has a relaxation time to the response of the acoustic excitation. In another word, as long as the shifting frequency is high enough, this frequency shifting will not break the spinning and vortex streaming generation. We chose 100 kHz as the shifting frequency, which corresponding to a 10 μs time frame for each excitation period. And for the demonstration of the capability of the dual droplet acoustofluidic centrifuge system, we used two droplets with different volume (4 μL and 5 μL) that corresponds to the spinning speed of 6867 ± 160 and 5674 ± 98 rpm, respectively. When the acoustic is on, two droplets will spin at the same time but at a different speed. The particle samples with a mixture of different sizes are initially put as the right droplet which has a slower spinning speed. And the left droplet is a blank droplet with solely PBS. After the acoustic waves are turned on, similar to the single droplet system, particles with a larger size will be concentrated to the middle of the droplet and the smaller particle will stay randomly distributed. Then as the spinning velocity of the left and right droplets are different, we predict the fluid portion in the microchannel actually will have different pressure on each side. Thus, there will be an extra spinning velocity difference induced force that can lead the particles from the high spin velocity region towards the low spin velocity region in addition to the

convective flow. This mechanism can lead the smaller particle in the right droplet to be transported to the left droplet since the larger particles have been concentrated to the middle area where the force is neglectable and will not influence the motion. Additionally, it seems the acoustic radiation force and induced streaming near the entrance of the droplet can provide the assistant for particles to walk into the microchannel towards the left droplet. From the experiment, we can observe the two acoustic beams which is used to drive the right droplet spin can to some extent accelerate the particles and push them into the channel. Meanwhile, the acoustic waves that for the left droplet enter the left droplet from the path that is closer to the middle of the drop further accelerates the particles in the channel. We prepared the polystyrene nanoparticle sample with a mixture of 100 nm and 28 nm and tested using the dual droplet acoustofluidic centrifuge system. For each size of the particle, we have different fluorescent labels (100 nm: red fluorescent, 28 nm: green fluorescent) so that we can better observe the concentration, separation, and transport process. During the testing, we can observe the red fluorescent becomes stronger in the middle of the right droplet which indicates the concentration of the larger particles. And we can also observe the green fluorescence passing the microchannel and transport from the right droplet to the left (Figure 3.19). One interesting find is that when the smaller particles passed the channel and enter the left droplet, they can be further concentrated to some extent. While with the single droplet system, when two sizes of the particles in the same droplet, we can barely see the concentration of the smaller particle.

This may result from the fact that when the larger particles are firstly concentrated, they will form a large cluster in the middle which may reduce the size of the streaming vortex and influence the continuous concentration of the particle with the smaller size (Figure 3.20). As for now, we can separate the particles of different sizes into the different droplets, we are able to extract the sample and perform further analysis. Thus, we measured the particle size distribution in both droplets using Zetasizer in order to characterize the separation performance. With the measurement, it is indicated that the original sample has mainly two peaks showing 28 nm and 100 nm. And for after the separation, we can observe a clear peak difference indicating the left droplet has the majority of the 28 nm particle while the right droplet has the majority of 100 nm particles. This result proves that we are able to separate the smaller particles from the larger particles and transport them to another droplet. During the testing of different particle size combinations, we also found that for our current system, in order to have a clear separation with relatively high separation yield and purity, the size difference between two particles should be relatively large, ideally, the size ratio will be higher than 1.5 (e.g., 28 nm and 100 nm). In such a way, the difference of the force and concentration time scale can be large enough to create room for smaller particles to be separated and transport to another droplet.

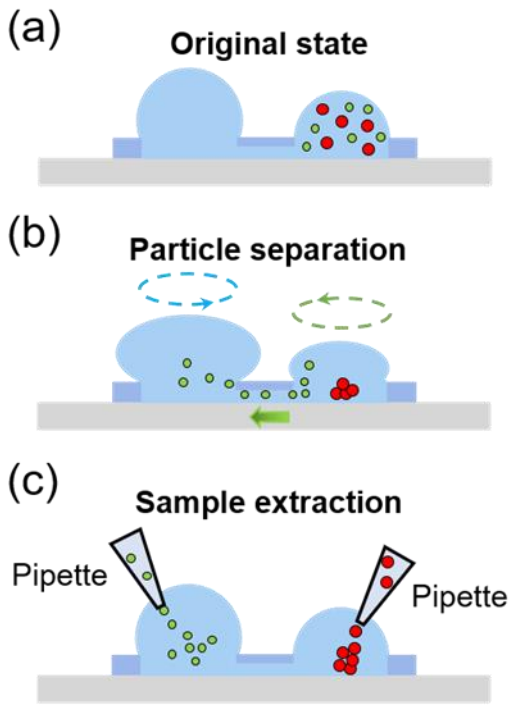

Figure 3.18: Schematic of the procedure of the particle transport and separation in dual-droplet acoustofluidic centrifuge. (a) The original system state contains one droplet (right) with the sample and one blank droplet (left). (b) With acoustic waves exciting, larger particles (red) are concentrated to the middle of the right droplet and the small particles (green) are gradually transferred to the left droplet. (c) After the separation and transport process, particles with different sizes are immersed in different droplets. Then two pipettes are used to extract the sample from droplets, respectively.

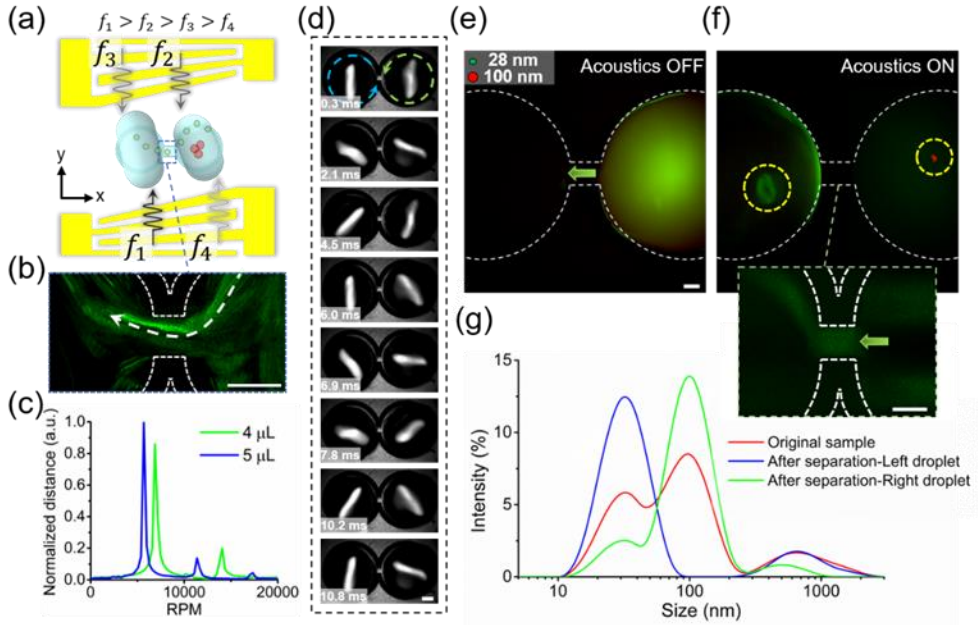

Figure 3.19: Particle separation and transport *via* a dual-droplet acoustofluidic centrifuge. (a) A schematic of the dual-droplet acoustofluidic centrifuge. (b) A composite image showing the particle trajectory through the center channel. (c) The frequency spectrum of the waveform plot of a fixed point on the droplet as it spins, indicating the spin frequency difference of the two droplets with different volumes. (d) Image sequence showing the top view of dual-droplet acoustofluidic centrifuge. Fluorescent images (e) before and (f) after the acoustic waves on, showing the nanoparticle separation and transport from one droplet to another. Inset: the fluorescent image of the middle channel showing the particle transport. (g) Particle size distribution comparison between the pre and post-separation samples. Scale bar: 200 μm.

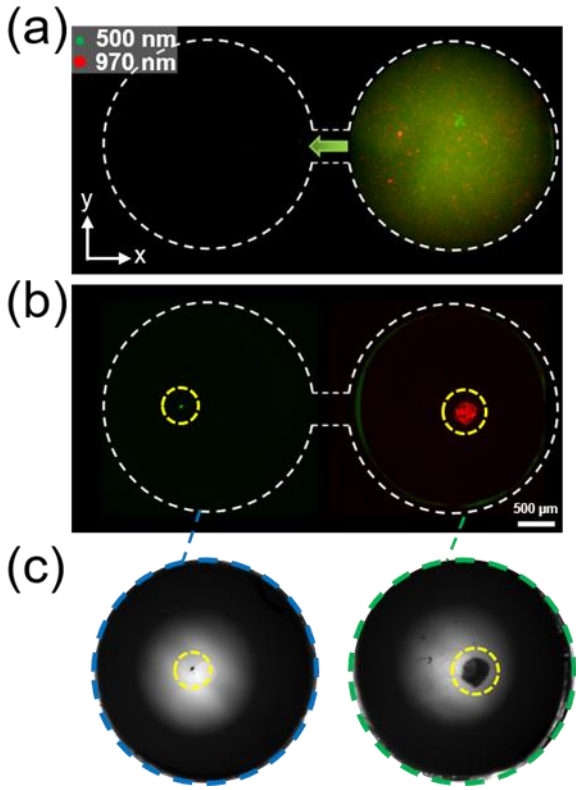

Figure 3.20: The separation and enrichment of particles with diameters of 500 nm and 970 nm *via* a dual-droplet acoustofluidic centrifuge. (a) Image showing the initial state before the acoustic field is turned on. The right droplet contains the particle samples and the left droplet is initially blank. (b) Image after the acoustic field is turned on; 500 nm particles are separated and transferred to the left droplet, and the 970 nm particles remain in the right droplet. After size-based separation, the respective particles are enriched in both droplets. Scale bar: 500 µm. (c) Bright-field image of the separated and enriched particles within the respective droplets. Both the left and right droplets show particle clusters at their centers.

After the proof-of-concept experiment using polystyrene particles, we further tested the exosome sample with our dual droplet acoustofluidic centrifuge system (Figure 3.21). Exosome is a well-knowing nanoscale extracellular vesicle that carries molecular cargo from the origin of the cells. It shows emerging potential for various biomedical

research , biomarker discovery, disease diagnostics, and health monitoring. The previous study has shown that exosomes have three subpopulations, namely: large exosomes (90-150 nm), small exosomes (60-80 nm), and exomeres (~35 nm). While the size difference is obvious, their biological properties also have a difference that can be significantly important for study. Exomeres, as the smallest subpopulation, is a non-membranous nanoparticle that has distinctive cargos compare to the other two subpopulations. The current optional methods for separating the exosome subpopulation includes the nano-DLD(Wunsch et al., 2016), ultrafiltration(Cheruvanky et al., 2007), and asymmetric flow field-flow fractionation (AF4)(H. Zhang et al., 2018), which needs either long duration (40 mins to several hours) or complex experiment system. As the spinning droplet shows the capability of concentrating and separating nanoparticles with the fine size difference, we tested the exosome sample derived from human plasma using the dual droplet spinning system. The experimental configuration and steps are the same as the aforementioned polystyrene nanoparticle separation. The nanoparticle size distribution from the original sample, left, and right droplet after the separation are tested using the nanoparticle tracking analysis (NTA) system. As shown in Figure 3.21, in the original sample, there are mainly three peaks under the 150 nm size range, which correlate to the reported three size range of subpopulations of the exosome respectively. After the separation and transport process, in the right droplet which contains the original sample at the beginning, there are mainly two size peaks remaining. Meanwhile, in the left droplet which contains the PBS

droplet at the beginning, the majority of the particles have a size below 60 nm. The TEM images of the three samples are captured, which correspond to the result of the NTA system. These results further support the exosome sample can be fractionated by our droplet spinning system based on the size difference. This result demonstrates the biological application that can be performed with our acoustofluidic centrifuge system. More functions may also be envisioned with multiple droplet arrays that potentially may result in the separation of the sample containing more complex components.

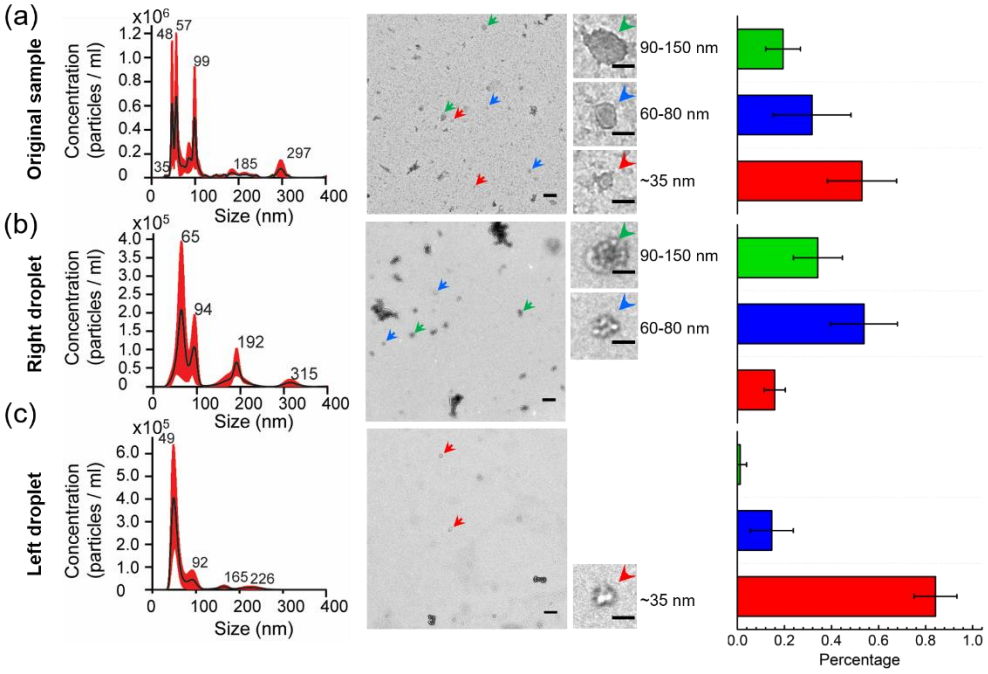

Figure 3.21: Exosome subpopulation separation and transport in an acoustofluidic centrifuge. The NTA analysis (left), TEM image (middle), and particle count (right) for the original exosome sample (a), right droplet after separation(b) and left droplet (c) after separation. Scale bar: TEM image: 200 nm. Insets: 50 nm.

3.6 Discussion and future work

In summary, we have developed an acoustofluidic centrifuge system that utilizes the acoustically driven spinning droplet and inner vortex streaming to enrich and separate the nanoparticles. The system includes a pair of slanted IDT and one or dual spinning droplet units. The surface acoustic waves can push the droplet out of its equilibrium shape and force it to spin along its vertical center axis. We have explored the factors that can influence the droplet spin. Specifically, the spinning speed is independent of the acoustic parameters (i.e., frequency, amplitude) but tightly connected to the droplet radius and the

surface tension of the liquid. It is also proved that this spinning motion can also be applied to the different organic fluids that are usually being used for biological applications (e.g., PBS, cell culture medium, and Bovine serum albumin). When the droplet starts to spin, there is a rotational Stokes drift phenomenon with which particles inside the droplet will follow the helical trajectory and be concentrated to the middle of the droplet. The observed effect is similar to the previous study which utilizes the mechanical vibration to create the liquid-interface metamaterials and particles can follow a 2D helical trajectory. While two systems share a similarity to some extent, the difference is significant as well. In the acoustofluidic centrifuge system, the particles follow a three-dimensional helical trajectory and the size of the small circle is gradually decreasing when the particle moves towards the center. Relying on the high frequency acoustic wave and the spinning motion, particle velocity can be remarkably increased by a factor of $\sim 10^2 \sim 10^3$. Meanwhile, we observed the spinning motion is in fact a continuous liquid-air interface deformation along the vertical center axis which can generate a strong secondary flow that indicates the underlying mechanism of the particle concentration. With this system, we are able to concentrate the nanoparticles with a size ranging from several nanometers (e.g., DNA molecules) to micrometers and can be used for biosample signal amplification and detection purpose. With the building of a dual droplet acoustofluidic centrifuge system, we can separate the nanoparticles and transport them from one droplet to another based on the concentration time scale difference between particles with multiple sizes. As

various bioparticles that possess important biological functions are within the size range from sub-micrometer to nanometer (e.g., DNA, virus, exosomes, proteins), the enrichment and separation are of great importance in biology, chemistry, and medicine. Our acoustofluidic centrifuge builds the bridge between acoustofluidic and nanoparticle manipulation. In the system, small sample can be processed, and rapid processing time also represents another advantage. Furthermore, the acoustofluidic centrifuge system is an open microfluidic system. This allows easy accessibility to the droplet via pipette, which eliminates the need for external fluid driving units (e.g., pump, valves, or other flow control devices). We believe that this platform can significantly simplify and speed up sample processing, detection, and reagent reactions in various applications such as point-of-care diagnostics, bioassays, and liquid biopsies.

Besides this proof-of-concept research, there are a lot more further studies that can be explored. In terms of the mechanism, although the force analysis of the particle is theoretically and numerically studied, the experimental measurement of the force is still a challenge. Since the drag force can be calculated by the particle velocity relate to the fluid, in a spinning system, it is difficult to directly measure this velocity. Meanwhile, the secondary flow generated radial force is also difficult to be directly measured. On the other hand, the particle being concentrated to the middle of the droplet is observed from the top view which only reflects the 2D information. The specific 3D location of the concentrated particle is unclear. This study may open up the new separation technique

that particles can be separated in the 3D spatial location and push the technique more towards the mini centrifuge that can have a much faster processing speed. In terms of the applications, one potential direction could be as aforementioned, to build a spinning droplet array and achieve the separation of the sample with more complex components. Another direction that may be valuable to pursue is the combination of the acoustofluidic centrifuge with other detection/characterization systems that can perform downstream analysis after the concentration and separation. This could potentially become an integrated system for biosample handling, processing, and analysis, which can be utilized for point-of-care applications.

Chapter 4: Acoustofluidic blood components separation for apheresis

Apheresis is a medical process that is crucial to blood donation and medical treatment. The studies of apheresis generally can be divided into different sub-directions with specific terminologies that can reflect the specific components of blood that are being separated. For example, plasmapheresis, plateletpheresis, leukapheresis, etc. In this chapter, we introduce several methods of acoustic based blood components, which would be a potential alternative for the common centrifugation technique or could be part of the apheresis equipment. Section 4.1 introduces the motivation of the study. Section 4.2 discussed the materials and methods used for acoustic based blood components separation. Section 4.3 detailed the theoretical model and working mechanism of different devices. Section 4.4 introduced the platelet separation using bulk acoustic waves. Then the next section (Section 4.5) discussed a prototype we built for small animal apheresis study. Finally, Section 4.6 is the discussion and proposed future work. Part of the work in this chapter is reported in Lab on a Chip.

4.1 Motivation

Blood, as a body fluid in humans and animals, is a significant medium that carries the necessary components to different organs/tissues and brings the metabolic waste derived from cells away. Generally, in vertebrates, blood contains blood cells including erythrocytes, leukocytes, and thrombocytes, suspended in plasma. Different blood components play various important roles in the blood and have gained significant

research attention for blood donation and therapy. Acoustic based separation, as an emerging separation technique, show great potential for blood components separation.

Among the blood components separation, platelet (thrombocytes) separation is an important medical procedure used in clinical medicine for platelet donation and treatment of essential thrombocytosis. Meanwhile, the platelet is a rich source of growth factors and is able to accelerate the recovery of human bones and soft tissues. The current standard protocol for platelet separation or plateletpheresis is using a centrifuge-based system that can continuously separate the blood into different components based on the density difference of different blood components. While it serves as a well-established method, there are still some remaining issues with this method, which includes long-duration and potential negative effect on platelet due to high speed rotation.

Currently, there are multiple alternative attempts being made at separating the platelets from the blood.(Aatonen et al., 2017; B??ing et al., 2014; Choi et al., 2007; Goetzl et al., 2016; Guldiken et al., 2012; Hou et al., 2011; Jiang et al., 2017; Z. Wang & Zhe, 2011) Most of these methods are based on microfluidic platforms which utilize external forces such as hydrophoretic,(Arifin et al., 2007; Choi et al., 2007, 2011; Di Carlo et al., 2008a; Hou et al., 2015; Y. Liu & Liu, 2006; Tay et al., 2017) dielectric,(Piacentini et al., 2011; Pommer et al., 2008) inertial focusing,(Di Carlo et al., 2008b; Hou et al., 2015; Tay et al., 2017) and acoustic forces,(Ahmed et al., 2016; Gedge & Hill, 2012; Ozcelik et al., 2018; Petersson et al., 2007; M. Wu, Ouyang, et al., 2017; S. P. Zhang et al., 2018) to substitute the centrifugal

force of the centrifugation method. With some of these platforms developed, the separation efficiency can reach a very high value. However, there is one common limit for these methods: The throughput is often insufficient (<<1 mL/min) to make them an ideal alternative for conventional platelet separation, particularly for clinical use. The capability of high throughput platelet isolation from whole blood can reduce blood-processing time, which may also protect the blood quality. On the other hand, researchers also developed several high throughput platelet separation platforms that can process the blood with a throughput of ~10 mL/min.(Adams et al., 2012; Y. Chen et al., 2016b) As a great research step forward, when dealing with clinical use, the device will also have the critical material requirement. The previously demonstrated methods usually require relatively high acoustic impedance channel materials, such as stainless steel or glass, which can form a thin resonator or half-wavelength resonator. These materials may generate certain issues as plasma proteins may quickly adhere to the surface of the channel, which can lead to the adhesion and activation of platelets.(Mrowietz et al., 2005) Furthermore, the material cost of stainless steel and glass is usually high which in fact may generate conflict with the common blood handling device need: disposable.

To bridge the connection between acoustic separation and clinical potential usage, we developed a plastic-based acoustic separation device enabling high-throughput and biocompatible platelet separation. Experiment results indicate this disposable acoustic device can separate platelets from whole blood with a platelet recovery rate (87.3%) and

a removal rate (88.9%) for red blood cells (RBCs) and white blood cells (WBCs) with a maximum throughput of 20 mL/min. Our device creates a resonator that is tailored for the plastic device, which is different from the existing plastic-based acoustofluidic devices that usually use an "in-plane" vibration mode. For the "in-plane" resonator, often utilize the half-wavelength channel width, and the channel will need to have relatively low channel height to avoid the blood sedimentation, thus microchannel formed in the device can only achieve a relatively low throughput (25–500 μL/min). (A. Mueller et al., 2013; Silva et al., 2017) We tested our device using human whole blood, and the results indicate that our plastic-based acoustofluidic device can achieve not only a high throughput (20 mL/min) but also over 85% for both the platelet recovery rate and the RBC/WBC removal rate. Besides the separation demonstration, we also evaluated the platelet function and integrity for the post-separation sample. These results indicate that the platelets separated from our plastic-based acoustic device possess similar or even better quality than those isolated using centrifugation. Thus, taken together, the advantages possessed in our device make it an excellent candidate to potentially serve as an alternative for the conventional platelet separation method.

Besides the platelet separation, plasma separation/plasmapheresis is widely used for various medical disorders, ranging from sickle cell diseases to treatment of rejection in organ transplantation. A major limitation to clinical investigations of plasmapheresis therapy is the size of current instruments which are designed for processing large volumes

of blood (5-7 liters) from adult humans. Lack of scalable apheresis instrumentation precludes not only treatment of neonates and infants with small blood volumes but also limits the development of suitable pre-clinical models for testing safety and therapeutic efficacy. On the other hand, for a broad range of biomedical research, the pilot studies usually have to be tested and validated on animal models before entering the clinical trials on human beings. Small mammalian animals, e.g., mice and rats, are commonly used as experimental models for clinical trials. As the small animals will be easier to feed, the body size determines that the mice will have much smaller blood volume for the specific study. However, the current apheresis equipment is mainly designed exclusively for healthy adult humans, which is difficult to be scaled down for small animal studies. Thus, a device that can separate the blood components with a small sample volume is needed to bridge the apheresis study and the small animal model. Acoustic separation, as a contactless, scalable, and biocompatible separation method is a suitable way to fit in this application, and can be significantly useful with a compact and integrated system.

Here, we have demonstrated an acoustic method that combines the microfluidic and tilted angle acoustic separation concept for plasma separation. Meanwhile, we have shown that the acoustic plasma separation technique can be easily scaled to fit different sample volumes. Centering from the microfluidic and tilted acoustic separation technique, we have demonstrated two configurations that can be applied for plasma separation, including the surface acoustic waves for small volume sample handling and

bulk acoustic wave for large volume sample handling. Finally, we have also developed an integrated prototype for small animal plasmapheresis. The system includes several units: the fluid driving unit with two peristaltic pumps, a cavity-based fluid stabilizer, a temperature controlling unit, and an acoustic separator. With this system, we have successfully demonstrated the mice plasma separation and tested the antibody level in order to characterize the separation effect. The in-vivo experiment was also tested for the acoustic plasmapheresis proof-of-concept study.

4.2 Materials and methods

4.2.1 Platelet separation device

The acoustic device consists mainly three plastic layers. The two PMMA sheets were machined by a CNC cutting machine as the top and bottom layers with the fluid channel, and the polyester film was fabricated using laser cutting as the divider and sandwiched between the top and bottom layers. Four plug-connectors were used as the inlets and outlets connecting with the tubing. A thin layer containing ultrasonic couplant was used between the device and acoustic transducer in order to make the acoustic waves effectively transmitted into the fluid channel. This couplant could be easily removed and cleaned, thus, enables the capability of reusing and recycling the acoustic transducer (Gu et al., 2019)(Figure 4.1).

In order to characterize the acoustic field in plastic device, a hydrophone (HNC0100, Onda Corporation, USA) was utilized along with an oscilloscope (DPO4104,

Tektronix, USA) to measure the acoustic field with acoustic wave propagate through the plastic layer. A homemade 3-D scanning platform controlled with the LabVIEW software (NI Corporation, USA) was used to control the movement of hydrophone and scan the field(Gu et al., 2019). The device was placed into a sink for measuring the acoustic field to identify the uniformity of the output transducer energy. The relationship between the driving voltage of the transducer and acoustic pressure was also measured with the hydrophone (Figure 4.2).

The blood sample and buffer solution were delivered into the acoustic device through a homemade peristaltic pump, which has four pumping channels and provides a range of flow rates from 1 to 50 mL/min(Gu et al., 2019). An RF signal generator (AFG 3011, Tektronic, USA) and a power amplifier (25A250A, Amplifier Research, USA) provided coherent AC signals to the acoustic transducer. The resonance frequency of the acoustic transducer after being bonded to the fluidic chamber was measured using a vector network analyzer (VNA 2180, Array Solutions, USA).

Whole blood sample (Zen-Bio, Inc.) was tested in the experiment. 10% sterile dextrose solution, which is commonly used for platelet storage and is biocompatible at this concentration,(Y. Chen et al., 2016a) was used as the buffer solution to tune the acoustic impedance of the medium.(Deshmukh et al., 2014) Sample before and after the separation was tested using Hematology analyzer (Ac·T diff2, Beckman Coulter, USA). The functionality and quality of platelets were evaluated by the expression level of CD

62P (P-selectin), morphology score, platelet aggregation activity, and the HSR(Y. Chen et al., 2016a; Gu et al., 2019).

4.2.2 Plasma separation device

The fabrication process of the surface acoustic wave based separation device is similar to the acoustofluidic centrifuge device mentioned in the last chapter. Basically, the electrodes of two IDTs (5-nm Cr and 50-nm Au) were fabricated on a 128° Y-cut lithium niobite (LiNbO3) wafer (Precision Micro-Optics, USA) by a standard photo lithography process, and then the process of electron beam evaporation and lift-off is followed to form the SAW device. Silver epoxy (MG Chemicals, USA) was used to connect wires to the IDT electrodes. The microchannels were fabricated by standard soft-lithography and a mold-replica procedure. After the fabrication of two main components, the substrate and PDMS channel were bonded together by oxygen plasma treatment. The PDMS channel was aligned with a tilted angle. Then the device was baked at 90 °C overnight for tightly bonding.

For the integrated system used for mice plasmapheresis, besides the SAW based separator, multiple other components were also combined. The system mainly includes peristaltic pumps for fluid driving (Instech Laboratories, Inc., Plymouth Meeting, Pennsylvania, USA), a cooling plate (TE Technology Inc., Traverse City, Michigan, USA), a PWM temperature controller (TE Technology Inc., Traverse City, Michigan, USA), a DC power supply (TE Technology Inc., Traverse City, Michigan, USA), a cavity-based fluid

stabilizer, and acoustic separator. The cavity based fluid stabilizer is formed with a four layer PDMS structure. Two layers with the fluidic channel and cavity were bonded together and sandwiched by another two plain PDSM layers.

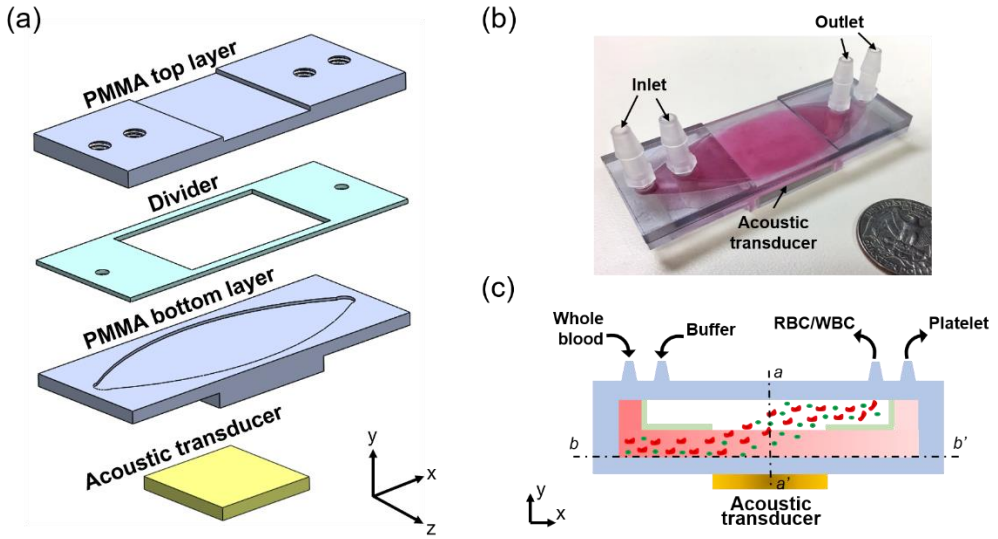

Figure 4.1: Schematic of the platelet separation device. (a-b) Illustration of the device components and (b) the photo of assembled device. (c) schematic of the acoustic platelet separation device.

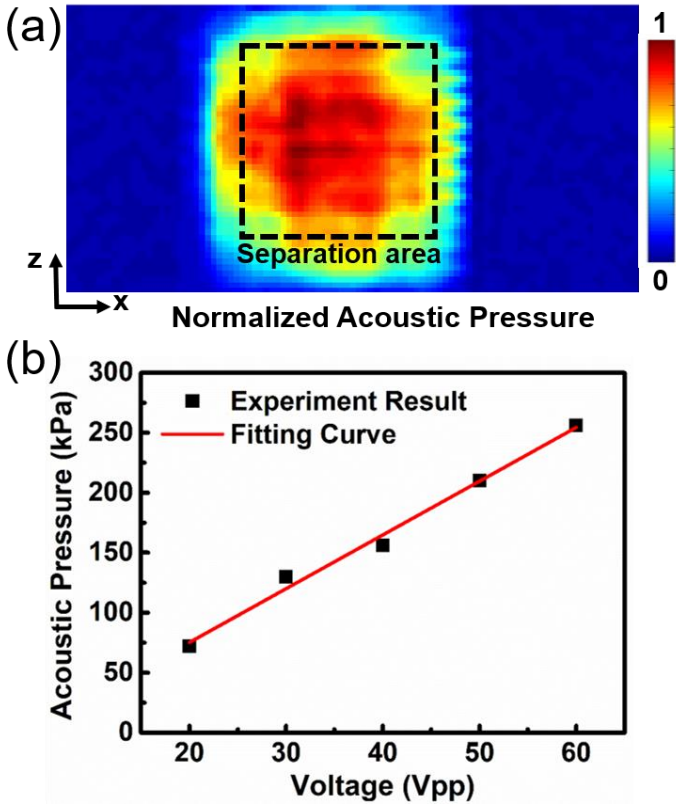

Figure 4.2: Acoustic field characterization. (a) The measured acoustic field of the corsssection plane. (b) The relationship between the acoustic pressure and the input voltage.

4.3 Theoretical model and working mechanism

The major mechanism of the acoustic separation device is based on the acoustic radiation force (F_R) and the drag force. These forces can be expressed as:

$$F_R = -\left(\frac{\pi p_0^2 V_p \beta_w}{2\lambda}\right)\Phi(\beta,\rho)sin(2ky) \tag{4.1}$$

$$\Phi(\beta,\rho) = \frac{5\rho_p - 2\rho_m}{2\rho_p + \rho_m} - \frac{\beta_p}{\beta_m} \tag{4.2}$$

$$F_d = -6\pi\mu a u_r \tag{4.3}$$

Where p_0, λ, V_p, ρ_m, ρ_p, β_m, β_p, μ, a, and u_r are the acoustic pressure, acoustic wavelength, the volume of the particle, density of the medium, density of the particle, compressibility of the medium, compressibility of the particle, viscosity of the medium, radius of the particle, and relative velocity of the particle, respectively. And y is the coordinate along the standing wave direction, and k is the wavenumber of the standing wave. Based on the equation, the acoustic radiation force on the specific particle is connected to the volume, density, compressibility, and power of the acoustic waves. Thus, the particles/cells with different aforementioned properties will experience different acoustic radiation forces and can be separated along with the fluid flow. Specifically, the acoustic standing wave provides the acoustic radiation force component with the direction perpendicular to the flow direction. Thus this perpendicular force component will enable the particle movement across the flow and being separated from the original sample flow. For the plane acoustic standing wave (i.e., the standing wave is strictly perpendicular to the flow direction), the acoustic radiation force acting on the particle provides all the forces for the cross flow movement. This configuration usually requires only one pressure nodes exist in the channel in order to provide a uniform force direction (from pressure antinode to pressure node) and separate the particle. The advantage of this configuration is it can provide a uniform stable force distribution through the fluid which will have a minor influence on the laminar flow condition. On the other hand, this

configuration will need a relatively critical channel dimension in order to fit with the specific frequency driving, thus has a relatively high fabrication requirement. For the tilted angle acoustic standing wave, part of the acoustic radiation force provides the cross flow movement. The advantage of this configuration is obvious, the separation effect is not tightly bonded with the specific channel dimension. In other words, the tilted angle can deflect the particles in a relatively wider range, which can potentially achieve high separation resolution and high throughput at the same time. The disadvantage of the tilted angle device will be beside the component of the acoustic radiation force benefitting the particle separation, the other parts of the acoustic radiation aligned with the flow direction will also act on the particles. This may influence the flow condition and sometimes cause particle aggregation inside the channel.

In order to better understand the acoustic field, fluid field, and particle displacement. We applied the numerical simulation using a finite-element-based software package, COMSOL Multiphysics® version 5.2a (COMSOL, USA). The "pressure Acoustics" module was used to solve the acoustic field for different configurations (plane standing wave, tilted standing wave) while the normal velocity was added to the boundary that the acoustic wave was propagating into. And a "Frequency Domain" model was set as the model solver at different frequencies. With this method, we can obtain the standing wave field distribution and further use it for acoustic radiation force calculation and particle trajectory calculation. For the fluid and particle, the "Laminar

Flow" and "Particle Tracing for Fluid Flow" modules were utilized for predicting the particle trajectory under the acoustic radiation force and the drag force at a different flow rate.

4.4 Platelet separation

The platelet separation device consists of a three-layer plastic structure and an acoustic transducer. The plastic structure has a polyester film sandwiched by two polymethyl methacrylate (PMMA) sheets with the carved channel. With the structure, a quarter-wavelength acoustic resonator is formed which has a pressure node near the top layer. The acoustic pressure distribution inside the channel can provide sufficient acoustic radiation force to push the blood cells from the original fluid to the buffer fluid. Meanwhile, the plastic device is usually used for the medical device due to the high biocompatibility and relatively convenient fabrication process. The bottom layer also has a rectangular chamber for the acoustic transducer insert. Here the quarter wavelength resonator is selected as the plastic material itself cannot provide efficient reflection and form the standing wave, thus the air boundary outside the plastic should also be considered in order to build a fully functional resonator. This resonator although needs a relatively critical fabrication requirement (separation performance is sensitive to the thickness of the layer), can provide sufficient throughput and ideal material usage. The polyester film in the middle serves as the function of a fluid divider so that the buffer fluid and sample will not contact each other before entering the separation area. With the

acoustic wave turning on, the wave will propagate through the plastic material and enter the fluid channel. The resonance will generate a monotonic pressure amplitude gradient inside the channel. When the blood sample and buffer flow into the channel, the blood components will experience the acoustic radiation force that provides the velocity across the flow, which has the force amplitude positively correlated to the size of the components. The red blood cells and white blood cells will suffer from larger force compare to the platelet due to the size difference. Thus, the red blood cells and white blood cells will be pushed into the buffer solution near the top layer while platelets remain to stay in the original flow near the bottom layer and thus are separated (Figure 4.3).

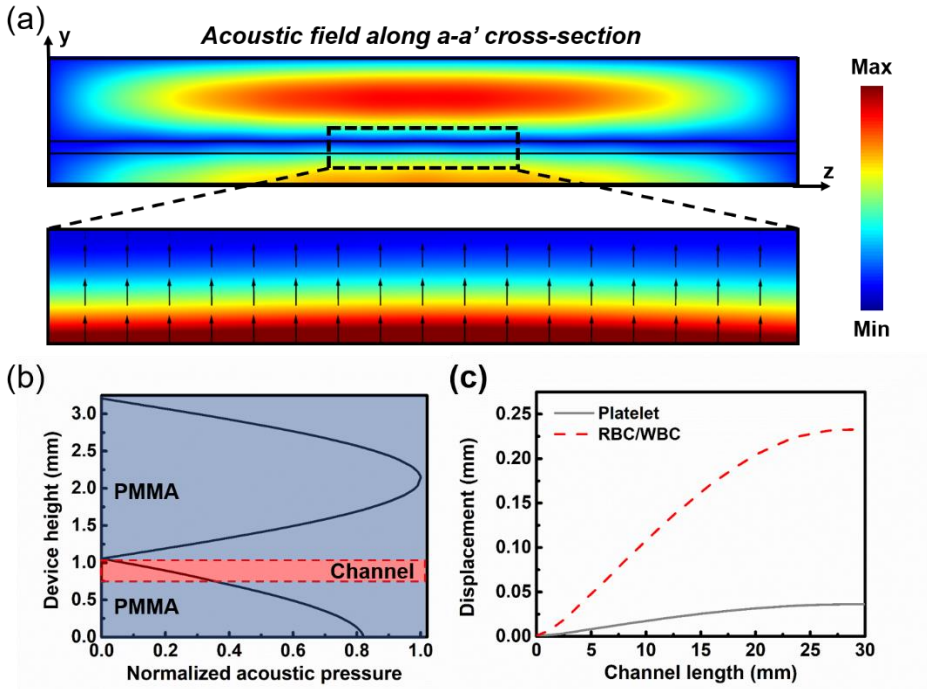

Figure 4.3: Acoustic radiation force and particle trajectory. (a) The simulate acoustic pressure distribution in the plastic channel. (b) The normalized acoustic pressure distribution along the middle line of the device. (c) The estimated particle trajectory under the acoustic radiation force and drag force.

We have tested the device with the human whole blood, and the buffer solution utilized the 10% sterile dextrose solution which was used as the impedance matching solution in previous studies. With the blood sample and buffer solution flowing through the channel without the acoustic energy turning on, from the outlet, we can observe the blood and buffer fluid flow out from different outlets with barely mixing. This indicates the laminar flow condition can be stably formed inside the channel. With the acoustic is on, we can directly observe the fluid color change in the tubing of the outlets as the red blood cells/white blood cells were pushed from the bottom fluid layer to the top fluid

layer (Figure 4.4). We also collected the sample, centrifuged it, and compared it with the original whole blood. It can be seen that although there is still a certain amount of red blood cells in the collected sample, a relatively large amount of red blood cells were removed from the blood. We have also tried different methods to characterize the separation performance. The hematology analyzer (Ac·T diff2, Beckman Coulter, USA) and flow cytometry were used to compare the platelet numbers before and after the separation (Figure 4.5). The results indicate that the device can achieve over 85% red blood cells/white blood cells removal rate and platelet recovery rate. Meanwhile, we have evaluated how the flow rate and driving voltage will influence the platelet separation performance. We quantitatively characterized the red blood cell/white blood cell removal rate and platelet recovery rate as the functions of the flow rate and the voltage (Figure 4.6). The removal rate is calculated by comparing the ratio of red blood cells/white blood cells from the cell collection outlets to the cells introduced from the inlet. And the recovery rate is calculated by comparing the ratio between the collected platelet from another outlet to the introduced platelet. As the experiment measurement, when the voltage is fixed and the flow rate changes, the red blood cells/white blood cells removal rate was obviously decreased, and the platelet recovery rate was barely influenced. This is mainly due to the faster flow, the time of the blood cells experiencing the acoustic effect is reduced, which will also induce the cell deflection length and the removal rate. Meanwhile, when the flow rate is fixed and the voltage is increased, the blood cell removal rate can be improved

while the platelet recovery rate will be decreased. This effect results from the fact that higher power will generate higher acoustic radiation force, which may push more cells and platelets across the flow to another fluid layer. Another potential reason is that the higher power will also bring more streaming and the thermal effect that may influence the bottom fluid layer. With an optimized flow rate and driving voltage (7 mL/min and ~45 Vpp), the blood cell removal rate and the platelet recovery rate can be improved to over 90%.

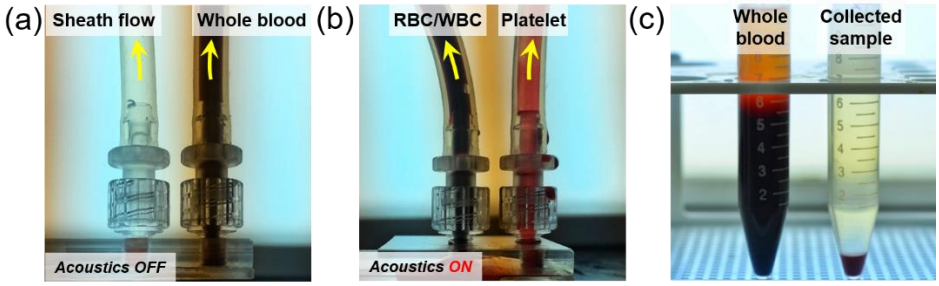

Figure 4.4: Platelet separation performance. (a) Initial flow condition when acoustic waves is off; (b) The photo of the outlets during the acoustic separation process. (c) The comparison of whole blood (left) and collected platelet sample (right).

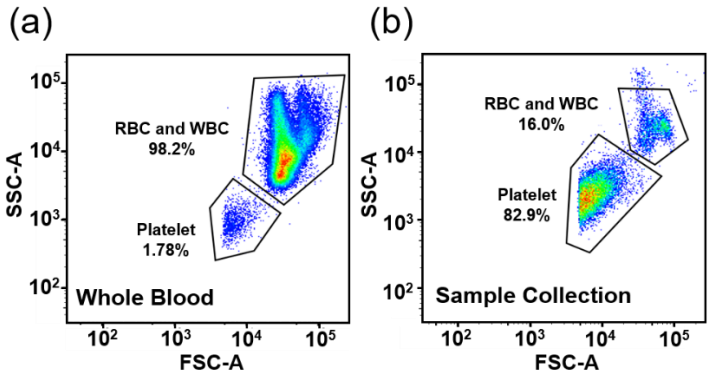

Figure 4.5: The flow cytometry results comparing (a) the whole blood and (b) collected sample.

The quality of the isolated platelets was evaluated using the following parameters: P-selectin, morphology score, platelet aggregation activity, and HSR (Figure 4.7). The characterization of the platelet quality shows that compared to centrifugation,(Anitua et al., 2016; Chandler, 2012; Perez et al., 2014) the acoustic platelet separation technology will have less damage to the platelets. Platelets were collected using centrifugation as positive control group, where 10 mL blood sample was centrifuged for 12 min at 200 g, then obtain and centrifuge the top and middle layers for 5 min at 1200 g for the platelet-rich plasma. (Dhurat & Sukesh, 2014; Perez et al., 2014) The expression level of CD 62P (P-selectin) was used to compare the activation levels for the platelets isolated by both acoustic and centrifduge methods, and the untreated platelets in the original whole blood serve as the negative control group. The results indicate that, comparing to the negative control, the platelet activation level increased by 13.3% using acoustic method while is lower than the

24% for centrifuged sample. Moreover, the acoustic separation also had a higher morphology score, which indicates that the discoid platelets were of greater integrity after acoustic separation than centrifugation.(Germing et al., 2007) In terms of the platelet aggregation activity, 5 μM adenosine diphosphate (ADP) was used as the agonist, and the corresponding platelet-poor plasma was utilized as control and transmission standardization. The collected platelets using acoustic technology show a higher aggregation ratios that implies a better platelet functionality. Finally, the acoustic spearated platelets had a higher HSR, thus, indicates a higher viability.(Kececi et al., 2014) Results were obtained from using three independent blood samples and analyzed using a one-way ANOVA post hoc test. Through the statistical analysis, we concluded that the quality of platelets isolated using our acoustic method can reach better value compare to those isolated using the centrifugation method. These results indicate that the acoustic separation can obtain the platelet with better quality and integraity compare to the centrifuge method.

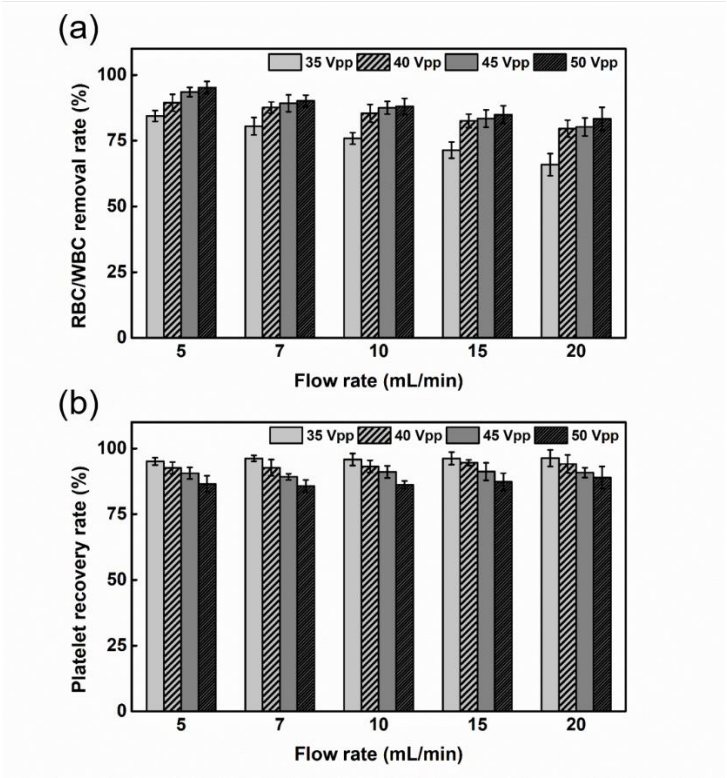

Figure 4.6: Device performance under different parameters. (a) The relationship of the RBC/WBC removal rate and (b) platelet recovery rate with the input voltage and flow rate. The data represent three independent experiments as average ± standard deviation.

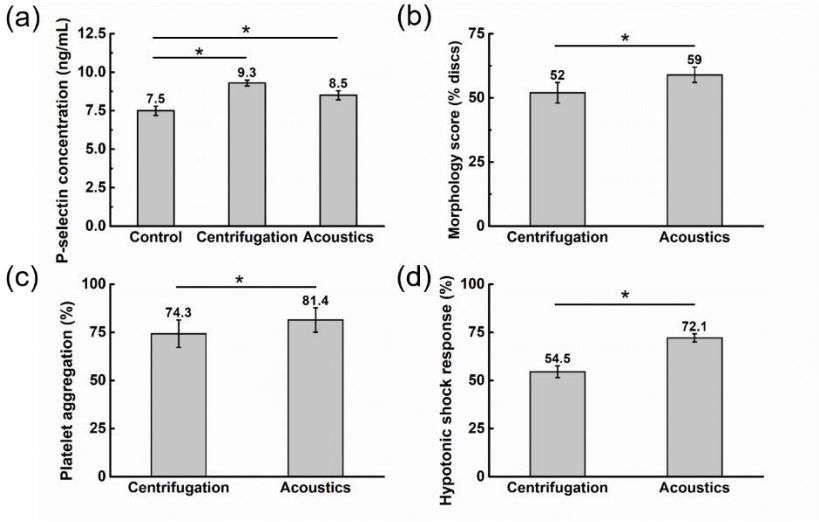

Figure 4.7: Evaluation of the quality of the isolated platelets by acoustic platelet separation technique and the centrifugation: (a) P-selectin characterization, (b) morphology score quantification, (c) platelet aggregation activity measurement, and (d) hypotonic shock response analysis. Data represents average ± standard deviation from three independent experiments (*$p < 0.05$).

Current plateletpheresis and apheresis instruments for clinical use developed along with the blood separation technique in the 1940's in order to provide blood fractions to patients. Thus these equipment usually target at a relatively large blood volume and high throughput mainly for adults. With the development of research specifically for children or small animals, the device that can handle small sample volumes are also needed to facilitate research. Due to the size of current equipment, research applications involving centrifugal-based devices have been usually utilized for human subjects, or large animals weighing >10 kg. Thus, the exploration of the smaller equipment that with

small sample volume input becomes valuable as well for performing research in smaller animals.

In this project, we describe a methodology that is capable of separating cells in a fluid medium with flexbile volume input using acoustic waves. This technique provides an ideal way for label-free separation of a variety of cellular and sub-cellular particles for both therapeutic, diagnostic, and research applications. Its versatility makes it flexibly suitable for platelet separation for the animals with different size from human beings, to small animals (e.g., mice).

Our plastic-based acoustic device can provide an efficient platelet separation with a 88.9% for the RBC/WBC removal rate, and 87.3% for the platelet recovery rate, and 20 mL/min for the throughput. The RBC/WBC removal rate and the platelet recovery rate can be improved to over 90% by optimizing the device's design and operation parameters. In our acoustic device, a relatrively low-power-intensity acoustic field is applied to the blood components for several seconds. The operational parameters of our device are comparable to the power and intensity used in ultrasonic imaging, which is regarded as a biocompatible method(Gu et al., 2019). The gold-standard platelet separation approach, centrifugation, on the other hand, typically lasts minutes to several hours; the components are exposed to strong forces for a much longer time. Thus, the gentle process used in our acoustic device expressed a less negative effect on the isolated platelets and provide a higher quality sample.

Our acoustofluidic devices still have some drawbacks. Its throughput is still lower than those of high-end plateletpheresis devices (up to 80 mL/min), thus, to some extent, limit the practical usage. In addition, the traditional plateletpheresis equipment can have better separation capability, for example, separate platelets from plasma to obtain platelet samples that have no contaminants such as cell-free DNA and cytokines, while our device has not yet demonstrated this feature. Nevertheless, our acoustic device possesses some unique advantages including high biocompatibility, low cost, and ease of preparation and operation. With these advantages, it can be an alternative not only for platelet separation but also for label-free separation of many other cellulars and sub-cellular particles.

4.5 Plasma separation

The surface acoustic wave has been utilized for different bioparticle separation in the continuous flow, e.g., platelet, bacteria, exosome. It possesses various unique advantages, for example, small device, high separation efficiency, biocompatible. It can be used as an ideal candidate for small animal apheresis study and the whole system can be compact. Thus, we have built an integrated acoustofluidic apheresis system for small animal blood separation. The key component of the integrated system is a tilted angle acoustic separator (Figure 4.8). The configuration is similar to our previous study. Basically, the acoustic separator consisted of a pair of the interdigital transducer and one microchannel on the piezoelectric substrate. The microchannel has three inlets and two outlets. When the blood sample flowing through the channel, the laminar flow condition

is formed with two sheath flow positioned on both sides. Without the acoustic wave, the blood will flow out from one outlet. After acoustic waves are turned on, the standing wave can be formed with periodic distributed pressure nodes and antinodes. The standing wave is tilted compared to the flow direction, thus can provide a tilted cross flow velocity on the particles in the blood. Therefore, the blood cells (i.e., red blood cells and white blood cells) and platelets will be deflected from the blood sample to one of the sheath flow and flow out from another outlet. By adding the fluorescence dye to the original blood sample and performing the separation experiment, we can confirm the plasma can be separated from the blood cells and platelets. Since the fluorescence dye is distributed in the plasma and cannot be pushed by the acoustic waves, it can serve as an indicator of the plasma flow direction. Meanwhile, the buffer solution does not contain the fluorescence, thus when the separation is performed, we can observe the separation phenomenon by observing both the bright field and fluorescent field (Figure 4.9). With our previous test, our acoustic separator can achieve a ~95% removal rate for blood cells (i.e., red blood cells and white blood cells) and ~90% platelet removal rate.

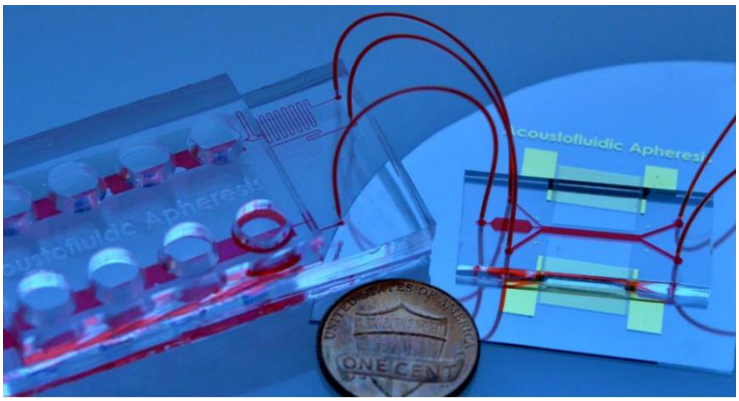

Figure 4.8: A photograph of acoutofluidic apheresis chip. The two components: the fluid controller and acoustophoresis separator, are connected. (Figure credit: Mengxi Wu)

Centering from the acoustic separator, we have built an integrated prototype in order to perform acoustofluidic apheresis for the small animal. In the system, there is a fluid stabilizer sitting on an acrylic platform while two peristaltic pumps and a power supply are placed under the platform. The acoustic separator is placed on top of a colling plate in order to keep the temperature being consistent during the experiment (Figure 4.10). With this integrated prototype, we have conducted a series of experiments to study the potential of utilizing it for small animal apheresis. In order to identify the plasma portion in the experiment, we chose to measure the antibody level in the separated sample. Since the antibody is usually very small (~10 nm), the acoustic radiation force acting on the antibody will be extremely limited, thus, it can serve as an indicator of the plasma and be further analyzed for potential separation efficiency and identify the fluid condition. We started the experiment by firstly identifying the plasma separation effect

with ex-vivo setup. We added monoclonal antibody (anti-CD3mAb) to non-reaching whole blood to mimic highly sensitized patients. And the monoclonal antibody did not show any cross activity to rat T cells. After we ran the whole blood sample with unbound antibodies with our system, we collected the sample in both outlets (cell portion outlet and plasma portion outlet). By measuring the antibody level, we confirmed the antibody exists in the plasma portion outlet while no antibody was detected in the cell portion outlet. This confirms the capability of our system separating the antibody from the blood cells and platelets. Then, in order to evaluate the feasibility of in vivo usage of our system, we performed plasmapheresis with the sensitized mouse. Animals were sensitized with skin transplantation. In the experiment, we drew the blood directly from the mouse with the peristaltic pump while the PBS was used as the sheath flow. The blood sample and buffer then went through the fluid stabilizer in order to form a more stable fluid condition and remove the microbubble that may be generated from the blood draw. After that, the sample and buffer will enter the acoustic separator and perform the separation. With the comparison between the acoustic on and off, the blood cells were identified obviously separated from the blood by color changing. 500 μL of circulating blood was running through the system via vena cava with a throughput of 10 μL/min. We compared donor-specific antibody (DSA) levels in the serum before and after plasmapheresis together with cell and plasma portion. Pre- and post-serum samples were collected via cheek bleeding from animals. The result shows an obvious reduction of the DSA level for proof-of-

concept testing. As an ongoing project, various things can be further improved. One is the residual volume of the system. Since our device for plasma separation is an integrated system that consisting of multiple units that connected using tubing, there will be a residual volume that is difficult to be collected. The residual volume of the whole system was measured for ~100 μL, including the volume in the tubing (connect to a peristaltic pump and between microfluidic channels) and microfluidic channels. Another is the device performance during the long time running. During the experiment, the input voltage was set as 30 Vpp, and the temperature was set as 20 °C. And it was found that during the long time running, there will be a liquid droplet generated on top of the acoustic separator device, which may cause unstable working performance. Thus, the tubing shortening and moisture controlling will be considered for further prototype development.

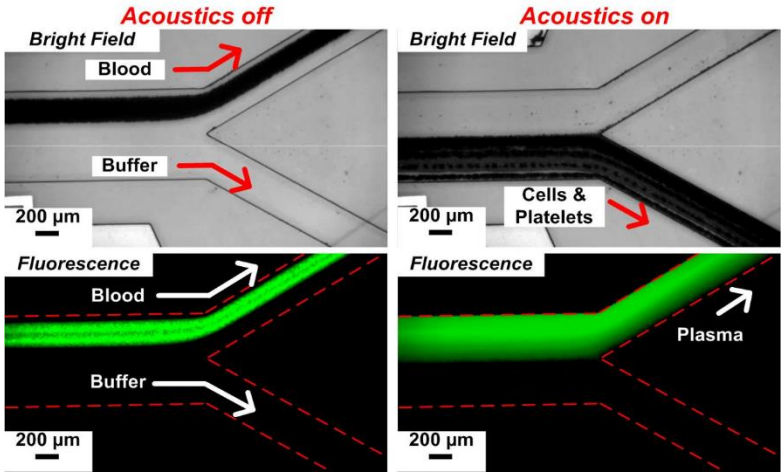

Figure 4.9: Separation of blood cells and plasma by acoustophoresis. Blood cells and platelets appear to be dark while green fluorescence indicates plasma. The acoustic waves transfer blood cells out from plasma to the buffer solution(M. Wu, 2018). (Figure credit: Mengxi Wu)

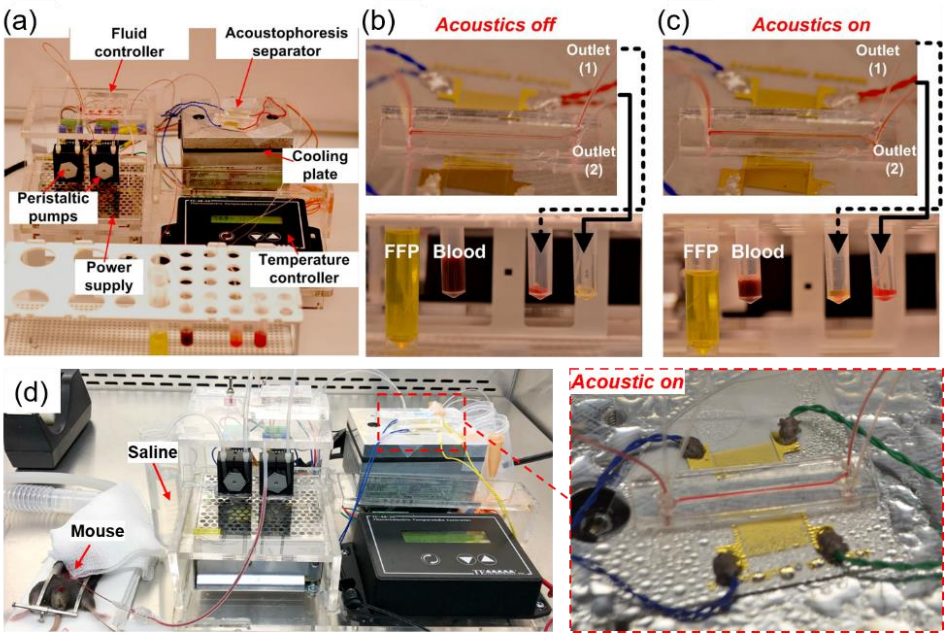

Figure 4.10: Plasma separation with the acoustofluidic apheresis system. (a) A prototype of acoustofluidic apheresis apparatus is working. (b) Blood and frozen fresh plasma (FFP) are sucked into the apheresis device and returned to other tubes. (c) Blood components are separated by using acoustics. Cells are filtered out from the original plasma and transferred to FFP(M. Wu, 2018). (Figure credit: a-c, Mengxi Wu), (d) In-vivo demonstration of plasma separation with mice. Inset: zoomed-in image of the working device.

4.6 Discussion and future work

In this chapter, we have discussed two configurations for blood components separation and the potential usage of the system for small animal studies. Apheresis or blood components separation studies have revealed broad study interests and can be utilized for various applications for therapy. While the centrifugation system already expressed powerful capability to meet different demands and becomes to be a gold-standard, the more diversified user-defined needs are coming forth and pushing the

technology development. Under this circumstance, acoustic based separation method shows a strong capability that can provide an efficient separation in a biocompatible, flexible scaling, contact-free, and non-invasive manner. Meanwhile, the acoustic device is compact, which leads to being an ideal separator and can be combined with different units to perform a systematic analysis or to serve as a therapeutic tool. Under the basis of standing wave mechanism, the acoustic device also possesses the features of simple operation and stable performance, which shows the great potential of being widely used for biological applications. In our study, we have demonstrated one plastic-based platelet separation device that can remove the red blood cells and white blood cells in a high-throughput and biocompatible way. Meanwhile, the plastic material makes the device ideal for disposable clinical use. On the other hand, we have developed an integrated prototype that can separate the plasma/antibody from the whole blood. Centering from the acoustic separator device, we have built a system including multiple accessories to enhance the overall workflow that can be applied to small animals, e.g., mice, rats, or rabbits. With the proof-of-concept demonstration, we proved that the system can function well when connecting with the mouse model. Further development is conducting to better optimize the system. With the development of the system, more functions can also be envisioned. For example, in-vivo plasma exchange or blood cell exchange with parallel experimental configuration.

On the other hand, there are multiple problems that will need to be addressed before the acoustic separation can be utilized for a real biomedical purpose. One is the thermal effect, as the acoustic wave is a mechanical wave when it propagates through different material, the acoustic energy absorption is unavoidable, which will be transferred to the thermal effect. This influence can be minimized when the throughput is relatively high (e.g., high throughput platelet separation study), the fast blood flow can bring the extra thermal energy away and avoid overheating on the specific location. However, this could influence the performance and the blood component quality when dealing with smaller throughput. The current method for dealing with this problem is to add a cooling plate to keep the temperature consistent. This diminished the overheating problem while also introduced another energy term that may induce the humid environment. Thus the further moisture control would also need to be considered. Another potential solution would be utilizing the circulating flow system to cool down the device. As the circulating flow is enclosed in the channel, the moisture control could potentially be removed. Another problem that was identified in our study is the plastic device. As aforementioned, the plastic device is ideal for the clinical disposable device and can be engineered to a different channel with a modern fabrication method. However, since the plastic material cannot provide an efficient reflection of the acoustic wave, a specific resonator should be utilized in order to form the standing wave environment. This will lead to the requirement of high resolution fabrication which to some extent

conflicted with the capability of the current fabrication technique. Furthermore, when acoustic wave interacts with the plastic device, both in-plane and out-of-plane vibration could be excited which could serve as a double-edged sword, and detailed optimization of the device and further exploration of the mechanism are needed.

Overall, acoustic methods expressed great potential for particle/cell separation, their contactless and biocompatibility features make them the specific benefit to the biomedical applications. With the further development of the technique and system, more pioneering research and emerging therapy could be implemented on small animals or even human beings.

Chapter 5: Conclusion

5.1 Summary

In this dissertation, we first went through a brief history of acoustic manipulation and how the synergetic effect can be achieved between the acoustic wave and fluid dynamics. Specifically, we believe the interplay of the acoustic waves and fluid motion is an important step towards applying acoustic manipulation to practical applications. Since in the majority of the biomedical applications, the native environment of the target particle is the liquid, the fluid dynamics is of great importance for the particle movement. Inspired and motivated by this concept, the main goal of our effort is to develop the next-generation acoustic manipulation platform. This aim can be divided into two parts: a) Break the current size limit of the targets that can be manipulated using sound waves. b) Increase the degree of freedom of acoustic manipulation. During the technical exploration, along with the acoustic wave modulation, we have proven that we can significantly leverage fluid dynamics in the process, which has traditionally been viewed as an adverse effect for the control of underwater objects. Through these studies, we have demonstrated several new capabilities of acoustic manipulation: 1. Acoustofluidic holography for micro- to nanoscale manipulation. 2. Acoustic driven droplet spinning (acoustofluidic centrifuge) system for nanoparticle enrichment and separation. 3. Acoustofluidic apheresis system. These three studies also correspond to three classic fluid systems: bulk fluid, droplet, and continuous flow. These three works are summarized as below:

1. Acoustofluidic holography for particle manipulation in the bulk fluid

The ability to construct two-dimensional (2D) and three-dimensional (3D) cell structures that closely resemble their native microenvironment is critical to the development of improved models for biomedical research and the fabrication of biomimetic tissues. However, it remains a significant challenge to produce the microstructural complexity required to achieve physiologically relevant functions. To this end, we have developed an acoustofluidic holography system for the 2D and 3D alignment of cells into prescribed arbitrarily shaped patterns using acoustic waves and fluid dynamics. With this technique, the cells can be patterned in the predesigned shape and then fixed by the cross-linking of the hydrogel. The basic experimental setup includes an acoustic transducer and a holographic acoustic lens. Cell patterning can be performed directly in a petri dish, which provides high compatibility with the workflows of biological laboratories. As the holographic acoustic lens serves as a key component, we have designed and implemented multiple holography algorithms (e.g., arbitrary phase/pressure design, frequency-multiplexing hologram, binary hologram) that are well suited for various applications. Moreover, we built a simulation model of acoustic streaming and air-liquid interface deformation, which serves to further elucidate the mechanisms behind cell patterning with this technique.

2. Acoustofluidic centrifuge for nanoparticle manipulation in a spinning droplet

While acoustic waves are generally utilized for micro-scale particle manipulation, our understanding of the interaction between acoustics and nanoparticles is remained limited. The acoustofluidic centrifuge system is originated from a new physical finding that surface acoustic waves can drive the spinning of a sessile fluid droplet. On the basis of this finding, we built theoretical and numerical models to analyze this phenomenon and further explored the capability of this system. The basic components consist of a pair of slanted interdigitated transducers (IDTs) and a circular polydimethyl-siloxane (PDMS) containment ring to encapsulate a portion of the droplet and define its shape. When two traveling SAWs propagate along the substrate from two opposing directions and enter the two flanks of the droplet, the droplet will spin along its central axis. Meanwhile, the particles inside the spinning droplet follow a helical trajectory and can be rapidly concentrated to the center. Based on this principle, we have tested different samples with the system and achieved the concentration and fluorescent signal amplification of polystyrene nanoparticles and DNA segments. Moreover, we have developed a dual-droplet system that can separate and transport the nanoparticles from one spinning droplet to another. Exosome subpopulation separation was successfully demonstrated as a practical application. The construction of this platform can potentially simplify and speed up sample processing, detection, and reagent reactions in various applications such as point-of-care diagnostics, bioassays, and liquid biopsies.

3. Acoustic blood components separation in continuous flow

Separation of blood components is a significant medical procedure used in clinical medicine. To this end, we have developed several techniques with different working mechanisms for multiple blood separation projects. These projects include platelet separation using a bulk acoustic resonator, plasma separation using tilted angle bulk acoustic waves, and surface acoustic wave (SAW) based plasma separation. Through these projects, we have detailed the process of the fabrication of plastic/PDMS devices, the development of acoustic resonators, and methods of characterization of blood components (e.g., hemocytometer, flow cytometry, and ELISA). In addition to the development of innovative acoustic based blood separation techniques, we have also designed an integrated device for use in animal experiments. We have developed a fully functional prototype that includes the peristaltic pump, cooling plate, fluid stabilizer, and acoustic separator, and we have successfully performed proof-of-concept plasma apheresis experiments for mice.

5.2 Future works

Acoustofluidics (i.e., the fusion of acoustics and microfluidics) particle manipulation is an emerging research topic that involves multidisciplinary studies, including physics, engineering, material science, and biology. As the underlying mechanism has been consistently unraveled, more innovations are conducted in both the device design and practical applications, which reversely keeps promoting the revealing of the new mechanism. As a wave based technique, acoustic wave possesses several significant

advantages: Contact-free, non-invasive, and label-free. These features make the acoustic method specifically ideal for life science applications, for example, acoustic imaging has already been widely applied for non-invasive in-vivo imaging of the human body. Meanwhile, acoustic tweezer, after years of development, have also revealed its potential for in-vivo manipulation. In terms of acoustic manipulation, although the technique is developing in a fast path, there are several key problems that need to be dealt with before it can be applied to practical biomedical applications. One is the acoustic wave absorption and reflection, especially when applying to the human body with a complex material environment. This will lead to some detailed problems, for example, the distortion of the acoustic field, insufficient acoustic energy at the target position, extra thermal effect, and manipulation resolution. At the same time, the acoustic wave is, to some extent, environment-sensitive. The acoustic configuration will need to be consistently optimized for different models (e.g., small animal model, human model, or different parts of the animal body). To deal with this obstacle, a more precise and flexible acoustic wave modulation method may be a tendency as a specific research topic. While some of the current studies demonstrated, the transducer array development cooperated with the time-reversal optimization would be an ideal option for this purpose. With more information that acoustic waves can carry on, better acoustic manipulation performance can be envisioned. Meanwhile, acoustic wave modulation should also be aligned well with the material properties. When dealing with more complex materials and

environments, the capability of controlling wave propagation is a key aspect. This will potentially require a deeper understanding of the material design and material analysis. For material design for acoustic wave modulation, metamaterial study can be explored and potentially provides an efficient way to control wave propagation (e.g., complementary metamaterial for wave transmission). On the other hand, the complex material analysis will require a large dataset that may benefit from the machine learning technique. This could potentially provide guidance for the acoustic configuration for the different working environments. Furthermore, as aforementioned, this is a multidisciplinary field that will need the collaboration of researchers from different study fields in order to push forward the development. The system simplification and working stability also is of great importance so that researchers from different fields can bring up more insights during the practical testing of the methods.

Moreover, the acoustic wave also shows great potential in terms of cell patterning. As we introduced in our study, acoustic waves can pattern the cells into complex 2D/3D shapes while providing a high localized cell density and complexity. This can potentially be utilized to build the functional tissues or organs if certain technical problems are addressed. One direction that can be envisioned in short term is utilizing the acoustic wave to form the arbitrary shaped 3D cell pattern in one step. As the acoustic holography technique has been developed, arbitrary acoustic fields can be formed in a cost-efficient way. The remaining issue will be since the current arbitrary shape is visualized as the

shape of the acoustic pressure antinode. However, the majority of the bioparticles (cells) possess the property of positive contrast factor, which means they can only move to the pressure nodes in the common liquid environment (e.g., PBS or cell culture medium). Although the contrast factor can be tuned by changing the liquid medium, this potentially may cause a relatively critical environment that may harm the cells. Thus, other innovations will be needed to form the 3D cell pattern in their native environment. For long term study, when acoustic waves can form the arbitrary shape cell pattern and build certain models, the higher requirement for acoustic based cell pattern will be of interest. For example, for the functional tissue or organ, a heterogenous cell pattern will be needed. While acoustic wave features for its label-free property, this could be a difficult point for this function and will need further development and exploration of the acoustic pattern technique.

Besides the acoustic mechanism exploration, some future directions that leaning towards practical applications can also be envisioned. One is system integration. While multiple acoustic based techniques already demonstrate the capability of handling clinical samples with a relatively simple device design (e.g., cell separation, cell sorter), during the practical usage, the device needs various support of other equipment (e.g., pump, function generator, amplifier). This will limit the acoustic device being utilized in the research lab environment. Thus, the further development and integration of the fluid driving unit, electrical unit, and microscopy will be needed to fully realize the clinical

potential of the acoustic devices. Furthermore, besides the therapeutic applications, one of the important values of the microfluidic device is to provide the information for the point-of-care application. This value can also be suitable for the acoustofluidic device. Thus, the further integration between the acoustofluidic device and the downstream analysis unit can also be envisioned which may possess great potential for human health monitoring.

Bibliography

Aatonen, M., Valkonen, S., Böing, A., Yuana, Y., Nieuwland, R., & Siljander, P. (2017). Isolation of platelet-derived extracellular vesicles. In *Methods in Molecular Biology* (Vol. 1545, pp. 177–188).

Adams, J. D., Ebbesen, C. L., Barnkob, R., Yang, A. H. J., Soh, H. T., & Bruus, H. (2012). High-throughput, temperature-controlled microchannel acoustophoresis device made with rapid prototyping. *Journal of Micromechanics and Microengineering*, *22*(7), 075017.

Ahmed, D., Ozcelik, A., Bojanala, N., Nama, N., Upadhyay, A., Chen, Y., Hanna-Rose, W., & Huang, T. J. (2016). Rotational manipulation of single cells and organisms using acoustic waves. *Nature Communications*, *7*, 11085.

Ai, Y., Sanders, C. K., & Marrone, B. L. (2013). Separation of escherichia coli bacteria from peripheral blood mononuclear cells using standing surface acoustic waves. *Analytical Chemistry*, *85*(19), 9126–9134.

Alghane, M., Chen, B. X., Fu, Y. Q., Li, Y., Luo, J. K., & Walton, A. J. (2010). Experimental and numerical investigation of acoustic streaming excited by using a surface acoustic wave device on a 128° YX-LiNbO3 substrate. *Journal of Micromechanics and Microengineering*, *21*(1), 15005.

Alghane, M., Chen, B. X., Fu, Y. Q., Li, Y., Luo, J. K., & Walton, A. J. (2011). Experimental and numerical investigation of acoustic streaming excited by using a surface acoustic wave device on a 128° YX-LiNbO3 substrate. *Journal of Micromechanics and Microengineering*, *21*(1), 15005.

Anitua, E., Pino, A., & Orive, G. (2016). Plasma rich in growth factors promotes dermal fibroblast proliferation, migration and biosynthetic activity. *Journal of Wound Care*, *25*(11), 680–687.

Antfolk, M., Muller, P. B., Augustsson, P., Bruus, H., & Laurell, T. (2014). Focusing of sub-micrometer particles and bacteria enabled by two-dimensional acoustophoresis. *Lab on a Chip*, *14*(15), 2791.

Arifin, D. R., Yeo, L. Y., & Friend, J. R. (2007). Microfluidic blood plasma separation via bulk electrohydrodynamic flows. *Biomicrofluidics*, *1*(1), 14103.

Armstrong, J. P. K., Puetzer, J. L., Serio, A., Guex, A. G., Kapnisi, M., Breant, A., Zong, Y., Assal, V., Skaalure, S. C., King, O., Murty, T., Meinert, C., Franklin, A. C.,

Bassindale, P. G., Nichols, M. K., Terracciano, C. M., Hutmacher, D. W., Drinkwater, B. W., Klein, T. J., … Stevens, M. M. (2018). Engineering Anisotropic Muscle Tissue using Acoustic Cell Patterning. *Advanced Materials*, *30*(43), 1–7.

Ashkin, A. (1999). Optical Trapping and Manipulation of Neutral Particles Using Lasers. *Optics and Photonics News*, *10*(5), 41.

B??ing, A. N., van der Pol, E., Grootemaat, A. E., Coumans, F. A. W., Sturk, A., & Nieuwland, R. (2014). Single-step isolation of extracellular vesicles by size-exclusion chromatography. *Journal of Extracellular Vesicles*, *3*(1).

Baresch, D., Thomas, J.-L., & Marchiano, R. (2016). Observation of a Single-Beam Gradient Force Acoustical Trap for Elastic Particles: Acoustical Tweezers. *Physical Review Letters*, *116*(2), 024301.

Barnkob, R., Augustsson, P., Laurell, T., & Bruus, H. (2012). Acoustic radiation-and streaming-induced microparticle velocities determined by microparticle image velocimetry in an ultrasound symmetry plane. *Physical Review E*, *86*(5), 56307.

Batchelor, C. K., & Batchelor, G. K. (2000). *An introduction to fluid dynamics*. Cambridge university press.

Baudoin, M, & Thomas, J.-L. (2020). *Annual Review of Fluid Mechanics Acoustic Tweezers for Particle and Fluid Micromanipulation*. 205–234.

Baudoin, Michael, Brunet, P., Matar, O. B., & Herth, E. (2012). Low power sessile droplets actuation via modulated surface acoustic waves. *Applied Physics Letters*, *100*(15), 1–5.

Bekdemir, A., & Stellacci, F. (2016). A centrifugation-based physicochemical characterization method for the interaction between proteins and nanoparticles. *Nature Communications*, *7*(1), 13121.

Bertin, N., Chraïbi, H., Wunenburger, R., Delville, J. P., & Brasselet, E. (2012). Universal Morphologies of fluid interfaces deformed by the radiation pressure of acoustic or electromagnetic waves. *Physical Review Letters*, *109*(24), 1–5.

Bourquin, Y., Reboud, J., Wilson, R., & Cooper, J. M. (2010). Tuneable surface acoustic waves for fluid and particle manipulations on disposable chips. *Lab on a Chip*, *10*(15), 1898.

Bourquin, Y., Syed, A., Reboud, J., Ranford-Cartwright, L. C., Barrett, M. P., & Cooper, J.

M. (2014). Rare-Cell Enrichment by a Rapid, Label-Free, Ultrasonic Isopycnic Technique for Medical Diagnostics. *Angewandte Chemie International Edition*, *53*(22), 5587–5590.

Brown, M., Cox, B., & Treeby, B. (2017). Design of multi-frequency acoustic kinoforms. *IEEE International Ultrasonics Symposium, IUS*, *244101*(2017).

Brown, M. D. (2019). Phase and amplitude modulation with acoustic holograms. *Applied Physics Letters*, *115*(5), 53701.

Brown, M. D., Allen, T. J., Cox, B. T., & Treeby, B. E. (2014). Control of optically generated ultrasound fields using binary amplitude holograms. *2014 IEEE International Ultrasonics Symposium*, 1037–1040.

Brown, M. D., Cox, B. T., & Treeby, B. E. (2017). Design of multi-frequency acoustic kinoforms. *Applied Physics Letters*, *111*(24), 244101.

Brown, M. D., Jaros, J., Cox, B. T., & Treeby, B. E. (2016). Control of broadband optically generated ultrasound pulses using binary amplitude holograms. *The Journal of the Acoustical Society of America*, *139*(4), 1637–1647.

Brunet, P., Baudoin, M., Matar, O. B., & Zoueshtiagh, F. (2010). Droplet displacements and oscillations induced by ultrasonic surface acoustic waves: A quantitative study. *Physical Review E - Statistical, Nonlinear, and Soft Matter Physics*, *81*(3), 1–8.

Bruus, H. (2012). Acoustofluidics 7: The acoustic radiation force on small particles. *Lab on a Chip*, *12*(6), 1014.

Chandler, W. L. (2012). Microparticle counts in platelet-rich and platelet-free plasma, effect of centrifugation and sample-processing protocols. *Blood Coagulation & Fibrinolysis*, 1.

Chen, C., Gu, Y., Philippe, J., Zhang, P., Bachman, H., Zhang, J., Mai, J., Rufo, J., Rawls, J. F., & Davis, E. E. (2021). Acoustofluidic rotational tweezing enables high-speed contactless morphological phenotyping of zebrafish larvae. *Nature Communications*, *12*(1), 1–13.

Chen, C., Zhang, S. P., Mao, Z., Nama, N., Gu, Y., Huang, P.-H., Jing, Y., Guo, X., Costanzo, F., & Huang, T. J. (2018). Three-dimensional numerical simulation and experimental investigation of boundary-driven streaming in surface acoustic wave microfluidics. *Lab on a Chip*, *18*(23), 3645–3654.

Chen, Y., Wu, M., Ren, L., Liu, J., Whitley, P. H., Wang, L., & Huang, T. J. (2016a). High-throughput acoustic separation of platelets from whole blood. *Lab Chip*, *16*(18), 3466–3472.

Chen, Y., Wu, M., Ren, L., Liu, J., Whitley, P. H., Wang, L., & Huang, T. J. (2016b). High-throughput acoustic separation of platelets from whole blood. *Lab Chip*, *16*(18), 3466–3472.

Cheruvanky, A., Zhou, H., Pisitkun, T., Kopp, J. B., Knepper, M. A., Yuen, P. S. T., & Star, R. A. (2007). Rapid isolation of urinary exosomal biomarkers using a nanomembrane ultrafiltration concentrator. *American Journal of Physiology-Renal Physiology*, *292*(5), F1657–F1661.

Chiou, P. Y., Ohta, A. T., & Wu, M. C. (2005). Massively parallel manipulation of single cells and microparticles using optical images. *Nature*, *436*(7049), 370–372.

Choi, S., Ku, T., Song, S., Choi, C., & Park, J.-K. (2011). Hydrophoretic high-throughput selection of platelets in physiological shear-stress range. *Lab Chip*, *11*(3), 413–418.

Choi, S., Song, S., Choi, C., & Park, J.-K. (2007). Continuous blood cell separation by hydrophoretic filtration. *Lab on a Chip*, *7*(11), 1532.

Collins, D. J., Alan, T., & Neild, A. (2014). Particle separation using virtual deterministic lateral displacement (vDLD). *Lab on a Chip*, *14*(9), 1595–1603.

Collins, D. J., Devendran, C., Ma, Z., Ng, J. W., Neild, A., & Ai, Y. (2016). Acoustic tweezers via sub – time-of-flight regime surface acoustic waves. *Science Advances*, *2*(7), 1–9.

Collins, D. J., Ma, Z., & Ai, Y. (2016). Highly Localized Acoustic Streaming and Size-Selective Submicrometer Particle Concentration Using High Frequency Microscale Focused Acoustic Fields. *Analytical Chemistry*, *88*(10), 5513–5522.

Collins, D. J., Ma, Z., Han, J., & Ai, Y. (2017). Continuous micro-vortex-based nanoparticle manipulation via focused surface acoustic waves. *Lab Chip*, *17*(1), 91–103.

Collins, D. J., Morahan, B., Garcia-Bustos, J., Doerig, C., Plebanski, M., & Neild, A. (2015). Two-dimensional single-cell patterning with one cell per well driven by surface acoustic waves. *Nature Communications*, *6*, 8686.

COMSOL, A. B. (2018). Comsol multiphysics® v. 5.4, Stockholm, Sweden. *COMSOL AB*.

Cummer, S. A., Christensen, J., & Alù, A. (2016). Controlling sound with acoustic metamaterials. *Nature Reviews Materials*, *1*(3), 16001.

Davis, J. A., Cottrell, D. M., Campos, J., Yzuel, M. J., & Moreno, I. (1999). Encoding amplitude information onto phase-only filters. *Applied Optics*, *38*(23), 5004.

Deshmukh, S., Brzozka, Z., Laurell, T., & Augustsson, P. (2014). Acoustic radiation forces at liquid interfaces impact the performance of acoustophoresis. *Lab Chip*, *14*(17), 3394–3400.

Destgeer, G., Cho, H., Ha, B. H., Jung, J. H., Park, J., & Sung, H. J. (2016). Acoustofluidic particle manipulation inside a sessile droplet: Four distinct regimes of particle concentration. *Lab on a Chip*, *16*(4), 660–667.

Destgeer, G., Ha, B. H., Jung, J. H., & Sung, H. J. (2014). Submicron separation of microspheres via travelling surface acoustic waves. *Lab Chip*, *14*(24), 4665–4672.

Destgeer, G., Jung, J. H., Park, J., Ahmed, H., & Sung, H. J. (2017). Particle Separation inside a Sessile Droplet with Variable Contact Angle Using Surface Acoustic Waves. *Analytical Chemistry*, *89*(1), 736–744.

Destgeer, G., & Sung, H. J. (2015). Recent advances in microfluidic actuation and micro-object manipulation via surface acoustic waves. *Lab on a Chip*, *15*(13), 2722–2738.

Dhurat, R., & Sukesh, M. (2014). Principles and methods of preparation of platelet-rich plasma: A review and author's perspective. *Journal of Cutaneous and Aesthetic Surgery*, *7*(4), 189.

Di Carlo, D., Edd, J. F., Irimia, D., Tompkins, R. G., & Toner, M. (2008a). Equilibrium separation and filtration of particles using differential inertial focusing. *Analytical Chemistry*, *80*(6), 2204–2211.

Di Carlo, D., Edd, J. F., Irimia, D., Tompkins, R. G., & Toner, M. (2008b). Equilibrium separation and filtration of particles using differential inertial focusing. *Analytical Chemistry*, *80*(6), 2204–2211.

Ding, X., Shi, J., Lin, S.-C. S., Yazdi, S., Kiraly, B., & Huang, T. J. (2012). Tunable patterning of microparticles and cells using standing surface acoustic waves. *Lab on a Chip*, *12*(14), 2491.

Dobson, C. M. (2003). Protein folding and misfolding. In *Nature* (Vol. 426, Issue 6968, pp. 884–890).

Drinkwater, B. W. (2016). Dynamic-field devices for the ultrasonic manipulation of microparticles. *Lab Chip*, *16*(13), 2360–2375.

Fan, K., Cao, C., Pan, Y., Lu, D., Yang, D., Feng, J., Song, L., Liang, M., & Yan, X. (2012). Magnetoferritin nanoparticles for targeting and visualizing tumour tissues. *Nature Nanotechnology*, *7*(7), 459–464.

Foresti, D., & Poulikakos, D. (2014). Acoustophoretic Contactless Elevation, Orbital Transport and Spinning of Matter in Air. *Physical Review Letters*, *112*(2), 024301.

Friend, J., & Yeo, L. Y. (2011). Microscale acoustofluidics: Microfluidics driven via acoustics and ultrasonics. *Reviews of Modern Physics*, *83*(2), 647–704.

Fuhrmann, D. A., Thon, S. M., Kim, H., Bouwmeester, D., Petroff, P. M., Wixforth, A., & Krenner, H. J. (2011). Dynamic modulation of photonic crystal nanocavities using gigahertz acoustic phonons. *Nature Photonics*, *5*(10), 605.

Gabor, D. (1961). IV light and information. In *Progress in optics* (Vol. 1, pp. 109–153). Elsevier.

Gaebel, R., Ma, N., Liu, J., Guan, J., Koch, L., Klopsch, C., Gruene, M., Toelk, A., Wang, W., & Mark, P. (2011). Patterning human stem cells and endothelial cells with laser printing for cardiac regeneration. *Biomaterials*, *32*(35), 9218–9230.

Gedge, M., & Hill, M. (2012). Acoustofluidics 17: Theory and applications of surface acoustic wave devices for particle manipulation. *Lab on a Chip*, *12*(17), 2998.

Germing, U., Platzbecker, U., Giagounidis, A., & Aul, C. (2007). Platelet morphology, platelet mass, platelet count and prognosis in patients with myelodysplastic syndromes [3]. In *British Journal of Haematology* (Vol. 138, Issue 3, pp. 399–400).

Ghanem, M. A., Maxwell, A. D., Wang, Y., Cunitz, B. W., & Khokhlova, V. A. (2020). *Noninvasive acoustic manipulation of objects in a living body*.

Glynne-Jones, P., Boltryk, R. J., & Hill, M. (2012). Acoustofluidics 9: Modelling and applications of planar resonant devices for acoustic particle manipulation. *Lab on a Chip*, *12*(8), 1417.

Goetzl, E. J., Goetzl, L., Karliner, J. S., Tang, N., & Pulliam, L. (2016). Human plasma platelet-derived exosomes: Effects of aspirin. *FASEB Journal*, *30*(5), 2058–2063.

Gor'kov, L. (n.d.). On the forces acting on a small particle in an acoustic field in an ideal

fluid, 1962. *Sov. Phys. Dokl*, *6*, 773.

Gor'kov, L. P. (1962). On the forces acting on a small particle in an acoustical field in an ideal fluid. *Sov. Phys. Dokl.*, *6*, 773–775.

Grier, D. G. (2003). A revolution in optical manipulation. *Nature*, *424*(6950), 810–816.

Gu, Y., Chen, C., Mao, Z., Bachman, H., Becker, R., Rufo, J., Wang, Z., Zhang, P., Mai, J., Yang, S., Zhang, J., Zhao, S., Ouyang, Y., Wong, D. T. W., Sadovsky, Y., & Huang, T. J. (2021). Acoustofluidic centrifuge for nanoparticle enrichment and separation. *Science Advances*, *7*(1), eabc0467.

Gu, Y., Chen, C., Rufo, J., Shen, C., Wang, Z., Huang, P.-H., Fu, H., Zhang, P., Cummer, S. A., & Tian, Z. (2020). Acoustofluidic Holography for Micro-to Nanoscale Particle Manipulation. *ACS Nano*.

Gu, Y., Chen, C., Wang, Z., Huang, P. H., Fu, H., Wang, L., Wu, M., Chen, Y., Gao, T., Gong, J., Kwun, J., Arepallyg, G. M., & Huang, T. J. (2019). Plastic-based acoustofluidic devices for high-throughput, biocompatible platelet separation. *Lab on a Chip*, *19*(3), 394–402.

Guldiken, R., Jo, M. C., Gallant, N. D., Demirci, U., & Zhe, J. (2012). Sheathless size-based acoustic particle separation. *Sensors*, *12*(1), 905–922.

Guo, F., Mao, Z., Chen, Y., Xie, Z., Lata, J. P., Li, P., Ren, L., Liu, J., Yang, J., & Dao, M. (2016). Three-dimensional manipulation of single cells using surface acoustic waves. *Proceedings of the National Academy of Sciences*, *113*(6), 1522–1527.

Hammarström, B., Laurell, T., & Nilsson, J. (2012). Seed particle-enabled acoustic trapping of bacteria and nanoparticles in continuous flow systems. *Lab on a Chip*, *12*(21), 4296.

Hou, H. W., Bhagat, A. A. S., Lee, W. C., Huang, S., Han, J., & Lim, C. T. (2011). Microfluidic devices for blood fractionation. *Micromachines*, *2*(3), 319–343.

Hou, H. W., Bhattacharyya, R. P., Hung, D. T., & Han, J. (2015). Direct detection and drug-resistance profiling of bacteremias using inertial microfluidics. *Lab on a Chip*, *15*(10), 2297–2307.

Hsueh, C. K., & Sawchuk, A. A. (1978). *Computer-generated double-phase holograms*. *1*.

Huang, X., & El-Sayed, M. A. (2010). Gold nanoparticles: Optical properties and

implementations in cancer diagnosis and photothermal therapy. *Journal of Advanced Research*, *1*(1), 13–28.

Jiang, X., Wong, K. H. K., Khankhel, A. H., Zeinali, M., Reategui, E., Phillips, M. J., Luo, X., Aceto, N., Fachin, F., Hoang, A. N., Kim, W., Jensen, A. E., Sequist, L. V., Maheswaran, S., Haber, D. A., Stott, S. L., & Toner, M. (2017). Microfluidic isolation of platelet-covered circulating tumor cells. *Lab Chip*, *17*(20), 3498–3503.

Jim, S. (2019). *Holograms to focus arbitrary ultrasonic fields through the skull*.

Johnson, K. A., Vormohr, H. R., Doinikov, A. A., Bouakaz, A., Shields IV, C. W., López, G. P., & Dayton, P. A. (2016). Experimental verification of theoretical equations for acoustic radiation force on compressible spherical particles in traveling waves. *Physical Review E*, *93*(5), 53109.

Kang, B., Shin, J., Park, H.-J., Rhyou, C., Kang, D., Lee, S.-J., Yoon, Y., Cho, S.-W., & Lee, H. (2018). High-resolution acoustophoretic 3D cell patterning to construct functional collateral cylindroids for ischemia therapy. *Nature Communications*, *9*(1), 5402.

Kang, J. H., Miettinen, T. P., Chen, L., Olcum, S., Katsikis, G., Doyle, P. S., & Manalis, S. R. (2019). Noninvasive monitoring of single-cell mechanics by acoustic scattering. *Nature Methods*, *16*(3), 263–269.

Karimi, M., & Akdogan, G. (2012). Comparison of different drag coefficient correlations in the CFD modelling of a Laboratory-Scale Rushton-Turbine Flotation Tank. *The Ninth International ….*

Kececi, Y., Ozsu, S., & Bilgir, O. (2014). A cost-effective method for obtaining standard platelet-rich plasma. *Wounds : A Compendium of Clinical Research and Practice*, *26*(8), 232–238.

King, L. V. (1934). On the acoustic radiation pressure on spheres. *Proceedings of the Royal Society of London. Series A-Mathematical and Physical Sciences*, *147*(861), 212–240.

Kinsler, L. E., Frey, A. R., Coppens, A. B., & Sanders, J. V. (1999). *Fundamentals of acoustics*. John wiley & sons.

Kunze, A., Tseng, P., Godzich, C., Murray, C., Caputo, A., Schweizer, F. E., & Di Carlo, D. (2015). Engineering cortical neuron polarity with nanomagnets on a chip. *ACS Nano*, *9*(4), 3664–3676.

Lamb, H. (1993). *Hydrodynamics*. Cambridge university press.

Lee, H., Lytton-Jean, A. K. R., Chen, Y., Love, K. T., Park, A. I., Karagiannis, E. D., Sehgal, A., Querbes, W., Zurenko, C. S., Jayaraman, M., Peng, C. G., Charisse, K., Borodovsky, A., Manoharan, M., Donahoe, J. S., Truelove, J., Nahrendorf, M., Langer, R., & Anderson, D. G. (2012). Molecularly self-assembled nucleic acid nanoparticles for targeted in vivo siRNA delivery. *Nature Nanotechnology*, *7*(6), 389–393.

Lee, J., Teh, S. Y., Lee, A., Kim, H. H., Lee, C., & Shung, K. K. (2010). Transverse Acoustic Trapping Using a Gaussian Focused Ultrasound. *Ultrasound in Medicine and Biology*, *36*(2), 350–355.

Lee, Y.-H., & Peng, C.-A. (2005). Enhanced retroviral gene delivery in ultrasonic standing wave fields. *Gene Therapy*, *12*(7), 625–633.

Lenshof, A., Ahmad-Tajudin, A., Jarås, K., Sward-Nilsson, A.-M., Åberg, L., Marko-Varga, G., Malm, J., Lilja, H., & Laurell, T. (2009). Acoustic whole blood plasmapheresis chip for prostate specific antigen microarray diagnostics. *Analytical Chemistry*, *81*(15), 6030–6037.

Lenshof, A., Magnusson, C., & Laurell, T. (2012). Acoustofluidics 8: Applications of acoustophoresis in continuous flow microsystems. *Lab on a Chip*, *12*(7), 1210.

Leportier, T., Park, M. C., Kim, Y. S., & Kim, T. (2015). Converting optical scanning holograms of real objects to binary Fourier holograms using an iterative direct binary search algorithm. *Optics Express*, *23*(3), 3403.

Li, H., Friend, J. R., & Yeo, L. Y. (2007). Surface acoustic wave concentration of particle and bioparticle suspensions. *Biomedical Microdevices*, *9*(5), 647–656.

Li, P., Mao, Z., Peng, Z., Zhou, L., Chen, Y., Huang, P.-H., Truica, C. I., Drabick, J. J., El-Deiry, W. S., Dao, M., Suresh, S., & Huang, T. J. (2015). Acoustic separation of circulating tumor cells. *Proceedings of the National Academy of Sciences*, *112*(16), 4970–4975.

Lighthill, J. (1978). Acoustic streaming. *Journal of Sound and Vibration*, *61*(3), 391–418.

Limaye, M. S., Hawkes, J. J., & Coakley, W. T. (1996). Ultrasonic standing wave removal of microorganisms from suspension in small batch systems. *Journal of Microbiological Methods*, *27*(2–3), 211–220.

Lipfert, J., Wiggin, M., Kerssemakers, J. W. J., Pedaci, F., & Dekker, N. H. (2011). Freely orbiting magnetic tweezers to directly monitor changes in the twist of nucleic acids. *Nature Communications*, *2*(1), 11782–11786.

Liu, J.-P., Yu, C.-Q., & Tsang, P. W. M. (2019). Enhanced direct binary search algorithm for binary computer-generated Fresnel holograms. *Applied Optics*, *58*(14), 3735.

Liu, S., Yuzvinsky, T. D., & Schmidt, H. (2013). Effect of fabrication-dependent shape and composition of solid-state nanopores on single nanoparticle detection. *ACS Nano*, *7*(6), 5621–5627.

Liu, Y., & Liu, W. K. (2006). Rheology of red blood cell aggregation by computer simulation. *Journal of Computational Physics*, *220*(1), 139–154.

Manor, O., Dentry, M., Friend, J. R., & Yeo, L. Y. (2011). Substrate dependent drop deformation and wetting under high frequency vibration. *Soft Matter*, *7*(18), 7976–7979.

Mao, Z., Li, P., Wu, M., Bachman, H., Mesyngier, N., Guo, X., Liu, S., Costanzo, F., & Huang, T. J. (2017). Enriching Nanoparticles via Acoustofluidics. *ACS Nano*, *11*(1), 603–612.

Martel, J. M., & Toner, M. (2014). Inertial focusing in microfluidics. *Annual Review of Biomedical Engineering*, *16*, 371–396.

Marzo, A., & Drinkwater, B. W. (2018). Holographic acoustic tweezers. *Proceedings of the National Academy of Sciences*, 201813047.

Marzo, A., Seah, S. A., Drinkwater, B. W., Sahoo, D. R., Long, B., & Subramanian, S. (2015a). Holographic acoustic elements for manipulation of levitated objects. *Nature Communications*, *6*(May), 1–7.

Marzo, A., Seah, S. A., Drinkwater, B. W., Sahoo, D. R., Long, B., & Subramanian, S. (2015b). Holographic acoustic elements for manipulation of levitated objects. *Nature Communications*, *6*, 8661.

Melde, K., Choi, E., Wu, Z., Palagi, S., Qiu, T., & Fischer, P. (2018). Acoustic Fabrication via the Assembly and Fusion of Particles. *Advanced Materials*, *30*(3), 1–5.

Melde, K., Mark, A. G., Qiu, T., & Fischer, P. (2016a). Holograms for acoustics. *Nature*, *537*(7621), 518–522.

Melde, K., Mark, A. G., Qiu, T., & Fischer, P. (2016b). Holograms for acoustics. *Nature*, *537*(7621), 518–522.

Mellin, S., & Nordin, G. (2001). Limits of scalar diffraction theory and an iterative angular spectrum algorithm for finite aperture diffractive optical element design. *Optics Express*, *8*(13), 705.

Memoli, G., Caleap, M., Asakawa, M., Sahoo, D. R., Drinkwater, B. W., & Subramanian, S. (2017). Metamaterial bricks and quantization of meta-surfaces. *Nature Communications*, *8*, 14608.

Meng, L., Cai, F., Li, F., Zhou, W., Niu, L., & Zheng, H. (2019). Acoustic tweezers. *Journal of Physics D: Applied Physics*, *52*(27), 273001.

Metherell, A. F., El-Sum, H. M. A., & Larmore, L. (1969). *Acoustical holography* (Vol. 1). Springer.

Mrowietz, C., Franke, R. P., Seyfert, U. T., Park, J. W., & Jung, F. (2005). Haemocompatibility of polymer-coated stainless steel stents as compared to uncoated stents. *Clinical Hemorheology and Microcirculation*, *32*(2), 89–103.

Mueller, A., Lever, A., Nguyen, T. V, Comolli, J., & Fiering, J. (2013). Continuous acoustic separation in a thermoplastic microchannel. *Journal of Micromechanics and Microengineering*, *23*(12), 125006.

Mueller, R. K. (1971). Acoustic holography. *Proceedings of the IEEE*, *59*(4), 2269–2276.

Nam, J., Lim, H., Kim, D., & Shin, S. (2011). Separation of platelets from whole blood using standing surface acoustic waves in a microchannel. *Lab on a Chip*, *11*(19), 3361.

Naseer, S. M., Manbachi, A., Samandari, M., Walch, P., Gao, Y., Zhang, Y. S., Davoudi, F., Wang, W., Abrinia, K., & Cooper, J. M. (2017). Surface acoustic waves induced micropatterning of cells in gelatin methacryloyl (GelMA) hydrogels. *Biofabrication*, *9*(1), 15020.

Nash, M. A., Waitumbi, J. N., Hoffman, A. S., Yager, P., & Stayton, P. S. (2012). Multiplexed enrichment and detection of malarial biomarkers using a stimuli-responsive iron oxide and gold nanoparticle reagent system. *ACS Nano*, *6*(8), 6776–6785.

Newman, C. M. H., & Bettinger, T. (2007). Gene therapy progress and prospects: Ultrasound for gene transfer. *Gene Therapy*, *14*(6), 465–475.

Ozcelik, A., Rufo, J., Guo, F., Gu, Y., Li, P., Lata, J., & Huang, T. J. (2018). Acoustic tweezers for the life sciences. *Nature Methods*, *15*(12), 1021–1028.

Patel, M. V., Tovar, A. R., & Lee, A. P. (2012). Lateral cavity acoustic transducer as an on-chip cell/particle microfluidic switch. *Lab Chip*, *12*(1), 139–145.

Perez, A. G. M., Lana, J. F. S. D., Rodrigues, A. A., Luzo, A. C. M., Belangero, W. D., & Santana, M. H. A. (2014). Relevant Aspects of Centrifugation Step in the Preparation of Platelet-Rich Plasma. *ISRN Hematology*, *2014*, 1–8.

Petersson, F., Åberg, L., Swärd-Nilsson, A. M., & Laurell, T. (2007). Free flow acoustophoresis: Microfluidic-based mode of particle and cell separation. *Analytical Chemistry*, *79*(14), 5117–5123.

Petersson, F., Nilsson, A., Jönsson, H., & Laurell, T. (2005). Carrier medium exchange through ultrasonic particle switching in microfluidic channels. *Analytical Chemistry*, *77*(5), 1216–1221.

Piacentini, N., Mernier, G., Tornay, R., & Renaud, P. (2011). Separation of platelets from other blood cells in continuous-flow by dielectrophoresis field-flow-fractionation. *Biomicrofluidics*, *5*(3).

Pommer, M. S., Zhang, Y., Keerthi, N., Chen, D., Thomson, J. A., Meinhart, C. D., & Soh, H. T. (2008). Dielectrophoretic separation of platelets from diluted whole blood in microfluidic channels. *Electrophoresis*, *29*(6), 1213–1218.

Prieto, G., Zečević, J., Friedrich, H., De Jong, K. P., & De Jongh, P. E. (2013). Towards stable catalysts by controlling collective properties of supported metal nanoparticles. *Nature Materials*, *12*(1), 34–39.

Rasmussen, M. B., Oddershede, L. B., & Siegumfeldt, H. (2008). Optical tweezers cause physiological damage to Escherichia coli and Listeria bacteria. *Applied and Environmental Microbiology*, *74*(8), 2441–2446.

Rayleigh, Lord. (1879). On the capillary phenomena of jets. *Proc. R. Soc. London*, *29*(196–199), 71–97.

Reboud, J., Bourquin, Y., Wilson, R., Pall, G. S., Jiwaji, M., Pitt, A. R., Graham, A., Waters, A. P., & Cooper, J. M. (2012). Shaping acoustic fields as a toolset for microfluidic manipulations in diagnostic technologies. *Proceedings of the National Academy of Sciences*, *109*(38), 15162–15167.

Rezk, A. R., Manor, O., Friend, J. R., & Yeo, L. Y. (n.d.). *Acoustowetting : Film Spreading , Fingering Instabilities and Soliton-Like Wave Propagation*. *2*, 3–5.

Roxworthy, B. J., Ko, K. D., Kumar, A., Fung, K. H., Chow, E. K. C., Liu, G. L., Fang, N. X., & Toussaint Jr, K. C. (2012). Application of plasmonic bowtie nanoantenna arrays for optical trapping, stacking, and sorting. *Nano Letters*, *12*(2), 796–801.

Sapozhnikov, O. A., Tsysar, S. A., Khokhlova, V. A., & Kreider, W. (2015). Acoustic holography as a metrological tool for characterizing medical ultrasound sources and fields. *The Journal of the Acoustical Society of America*, *138*(3), 1515–1532.

Schmid, L., Weitz, D. A., & Franke, T. (2014). Sorting drops and cells with acoustics: acoustic microfluidic fluorescence-activated cell sorter. *Lab on a Chip*, *14*(19), 3710–3718.

Settnes, M., & Bruus, H. (2012). Forces acting on a small particle in an acoustical field in a viscous fluid. *Physical Review E*, *85*(1), 16327.

Shen, C. L., Xie, W. J., & Wei, B. (2010). Parametrically excited sectorial oscillation of liquid drops floating in ultrasound. *Physical Review E - Statistical, Nonlinear, and Soft Matter Physics*, *81*(4), 1–6.

Sheppard, C. J. R., Lin, J., & Kou, S. S. (2013). Rayleigh–Sommerfeld diffraction formula in k space. *Journal of the Optical Society of America A*, *30*(6), 1180.

Shilton, R., Tan, M. K., Yeo, L. Y., & Friend, J. R. (2008). Particle concentration and mixing in microdrops driven by focused surface acoustic waves. *Journal of Applied Physics*, *104*(1).

Silva, R., Dow, P., Dubay, R., Lissandrello, C., Holder, J., Densmore, D., & Fiering, J. (2017). Rapid prototyping and parametric optimization of plastic acoustofluidic devices for blood–bacteria separation. *Biomedical Microdevices*, *19*(3), 70.

Skowronek, V., Rambach, R. W., Schmid, L., Haase, K., & Franke, T. (2013). Particle Deflection in a Poly(dimethylsiloxane) Microchannel Using a Propagating Surface Acoustic Wave: Size and Frequency Dependence. *Analytical Chemistry*, *85*(20), 9955–9959.

Spalding, G. C., Courtial, J., & Leonardo, R. Di. (2011). Holographic optical tweezers. *Physics*, *11*(7), 1196–1205.

Stratakis, M., & Garcia, H. (2012). Catalysis by supported gold nanoparticles: beyond

aerobic oxidative processes. *Chemical Reviews*, *112*(8), 4469–4506.

Stuart, D., Barter, O., & Kuhn, A. (2014). *Fast algorithms for generating binary holograms*. *211001*(2008), 24837–24846.

Sun, J., Xianyu, Y., & Jiang, X. (2014). Point-of-care biochemical assays using gold nanoparticle-implemented microfluidics. *Chemical Society Reviews*, *43*(17), 6239–6253.

Svoboda, K., Mitra, P., & Block, S. (1994). Fluctuation analysis of motor protein movement and single enzyme kinetics. *Proceedings of the National Academy of Sciences*, *91*(December), 11782–11786.

Tan, M. K., Friend, J. R., Matar, O. K., & Yeo, L. Y. (2010). Capillary wave motion excited by high frequency surface acoustic waves. *Physics of Fluids*, *22*(11).

Tay, H. M., Kharel, S., Dalan, R., Chen, Z. J., Tan, K. K., Boehm, B. O., Loo, S. C. J., & Hou, H. W. (2017). Rapid purification of sub-micrometer particles for enhanced drug release and microvesicles isolation. *NPG Asia Materials*, *9*(9), e434.

Teo, T., & Reid, J. M. (1986). Multifrequency Holography Using Backpropagation. *Ultrasonic Imaging*, *8*, 213–224.

Thielicke, W., & Stamhuis, E. (2014). PIVlab–towards user-friendly, affordable and accurate digital particle image velocimetry in MATLAB. *Journal of Open Research Software*, *2*(1), e30.

Veronesi, W. A., & Maynard, J. D. (1987). Nearfield acoustic holography (NAH) II. Holographic reconstruction algorithms and computer implementation. *The Journal of the Acoustical Society of America*, *81*(5), 1307–1322.

Wang, K., Schonbrun, E., Steinvurzel, P., & Crozier, K. B. (2011). Trapping and rotating nanoparticles using a plasmonic nano-tweezer with an integrated heat sink. *Nature Communications*, *2*, 469.

Wang, Y., Ma, M., Wang, J., Zhang, W., Lu, W., Gao, Y., Zhang, B., & Guo, Y. (2018). Development of a photo-crosslinking, biodegradable GelMA/PEGDA hydrogel for guided bone regeneration materials. *Materials*, *11*(8), 1345.

Wang, Z., & Zhe, J. (2011). Recent advances in particle and droplet manipulation for lab-on-a-chip devices based on surface acoustic waves. *Lab on a Chip*, *11*(7), 1280.

Wikipedia contributors. (2020). *Acoustic wave --- {Wikipedia}{,} The Free Encyclopedia*.

Wiklund, M., Green, R., & Ohlin, M. (2012a). Acoustofluidics 14: Applications of acoustic streaming in microfluidic devices. *Lab on a Chip*, *12*(14), 2438.

Wiklund, M., Green, R., & Ohlin, M. (2012b). Acoustofluidics 14: Applications of acoustic streaming in microfluidic devices. *Lab on a Chip*, *12*(14), 2438.

Wu, J. R. (1991). Acoustical tweezers. *The Journal of the Acoustical Society of America*, *89*(5), 2140–2143.

Wu, M. (2018). ACOUSTOFLUIDIC SEPARATION TECHNOLOGY FOR ADVANCING HEALTH CARE. *PennState Electronic Theses and Dissertations for Graduate School*, *August*.

Wu, M., Huang, P., Zhang, R., Mao, Z., Chen, C., Kemeny, G., Li, P., Lee, A. V, Gyanchandani, R., & Armstrong, A. J. (2018). Circulating Tumor Cell Phenotyping via High-Throughput Acoustic Separation. *Small*, *14*(32), 1801131.

Wu, M., Mao, Z., Chen, K., Bachman, H., Chen, Y., Rufo, J., Ren, L., Li, P., Wang, L., & Huang, T. J. (2017). Acoustic Separation of Nanoparticles in Continuous Flow. *Advanced Functional Materials*, *27*(14), 1606039.

Wu, M., Ouyang, Y., Wang, Z., Zhang, R., Huang, P.-H., Chen, C., Li, H., Li, P., Quinn, D., Dao, M., Suresh, S., Sadovsky, Y., & Huang, T. J. (2017). Isolation of exosomes from whole blood by integrating acoustics and microfluidics. *Proceedings of the National Academy of Sciences*, *114*(40), 10584–10589.

Wu, M., Ozcelik, A., Rufo, J., Wang, Z., Fang, R., & Huang, T. J. (2019). Acoustofluidic separation of cells and particles. *Microsystems & Nanoengineering*, *5*(1), 32.

Wunsch, B. H., Smith, J. T., Gifford, S. M., Wang, C., Brink, M., Bruce, R. L., Austin, R. H., Stolovitzky, G., & Astier, Y. (2016). Nanoscale lateral displacement arrays for the separation of exosomes and colloids down to 20nm. *Nature Nanotechnology*, *11*(11), 936–940.

Xie, Y., Shen, C., Wang, W., Li, J., Suo, D., Popa, B.-I., Jing, Y., & Cummer, S. A. (2016). Acoustic Holographic Rendering with Two-dimensional Metamaterial-based Passive Phased Array. *Scientific Reports*, *6*, 35437.

Xu, J., Kwak, K. J., Lee, J. L., & Agarwal, G. (2010). Lifting and sorting of charged Au nanoparticles by electrostatic forces in atomic force microscopy. *Small*, *6*(19), 2105–

2108.

Yang, A. H. J., Moore, S. D., Schmidt, B. S., Klug, M., Lipson, M., & Erickson, D. (2009). Optical manipulation of nanoparticles and biomolecules in sub-wavelength slot waveguides. *Nature*, *457*(7225), 71–75.

Yang, Y., Ma, T., Li, S., Zhang, Q., Huang, J., Liu, Y., Zhuang, J., Li, Y., Du, X., Niu, L., Xiao, Y., Wang, C., Cai, F., & Zheng, H. (2021). *Self-Navigated 3D Acoustic Tweezers in Complex Media Based on Time Reversal*. *2021*.

Yasuda, K., & Kamakura, T. (1997). Acoustic radiation force on micrometer-size particles. *Applied Physics Letters*, *71*(13), 1771.

Yilmaz, F., & Gundogdu, M. Y. (2009). Analysis of conventional drag and lift models for multiphase CFD modeling of blood flow. *Korea-Australia Rheology Journal*, *21*(3), 161–173.

Zeng, X., & McGough, R. J. (2008). Evaluation of the angular spectrum approach for simulations of near-field pressures. *The Journal of the Acoustical Society of America*, *123*(1), 68–76.

Zhang, H., Freitas, D., Kim, H. S., Fabijanic, K., Li, Z., Chen, H., Mark, M. T., Molina, H., Martin, A. B., Bojmar, L., Fang, J., Rampersaud, S., Hoshino, A., Matei, I., Kenific, C. M., Nakajima, M., Mutvei, A. P., Sansone, P., Buehring, W., … Lyden, D. (2018). Identification of distinct nanoparticles and subsets of extracellular vesicles by asymmetric flow field-flow fractionation. *Nature Cell Biology*, *20*(3), 332–343.

Zhang, J., Tian, Y., Cheng, Y., & Liu, X. (2020). Acoustic holography using composite metasurfaces. *Applied Physics Letters*, *116*(3), 30501.

Zhang, N., Zuniga-Hertz, J. P., Zhang, E. Y., Gopesh, T., Fannon, M. J., Wang, J., Wen, Y., Patel, H. H., & Friend, J. (2021). Microliter ultrafast centrifuge platform for size-based particle and cell separation and extraction using novel omnidirectional spiral surface acoustic waves. *Lab on a Chip*.

Zhang, S. P., Lata, J., Chen, C., Mai, J., Guo, F., Tian, Z., Ren, L., Mao, Z., Huang, P. H., Li, P., Yang, S., & Huang, T. J. (2018). Digital acoustofluidics enables contactless and programmable liquid handling. *Nature Communications*, *9*(1), 2928.

Zhao, H., Sen, S., Udayabhaskararao, T., Sawczyk, M., Kucanda, K., Manna, D., Kundu, P. K., Lee, J. W., Král, P., & Klajn, R. (2016). Reversible trapping and reaction acceleration within dynamically self-assembling nanoflasks. *Nature Nanotechnology*,

11(1), 82–88.

Zhu, X., Wu, J., Shan, W., Tao, W., Zhao, L., Lim, J., D'Ortenzio, M., Karnik, R., Huang, Y., & Shi, J. (2016). Polymeric nanoparticles amenable to simultaneous installation of exterior targeting and interior therapeutic proteins. *Angewandte Chemie International Edition*, *55*(10), 3309–3312.

Biography

Yuyang Gu attended Nanjing University, Jiangsu, China from 2009 to 2013, where he earned his bachelor's degree in science. In 2016, he obtained his master's degree of science in physics from Nanjing University. In the same year, Yuyang joined the Acoustofluidic Lab at the Department of Mechanical Engineering and Materials Science, Duke University. Following is a list of his publications:

C. Chen, **Y. Gu**, J. Philippe, P. Zhang, H. Bachman, J. Zhang, J. Mai, J. Rufo, J. Rawls, E. Davis, N. Katsanis, and T. J. Huang, "Acoustofluidic rotational tweezing enables high-speed contactless morphological phenotyping of zebrafish larvae", *Nature Communications*, 12(1), 1-13.

H. Zhu, P. Zhang, Z. Zhong, J. Xia, J. Rich, J. Mai, X. Su, Z. Tian, H. Bachman, J. Rufo, **Y. Gu**, P. Kang, K. Chakrabarty, T. P. Witelski, and T. J. Huang, "Acoustohydrodynamic tweezers via spatial arrangement of streaming vortices", *Science Advances*, Vol. 7, No. 2, eabc7885, 2021.

Y. Gu, C. Chen, Z. Mao, H. Bachman, R. Becker, J. Rufo, Z. Wang, P. Zhang, J. Mai, S. Yang, J. Zhang, S. Zhao, Y. Ouyang, D. T. W. Wong, Y. Sadovsky, and T. J. Huang, "Acoustofluidic centrifuge for nanoparticle enrichment and separation", *Science Advances*, Vol. 7, No. 1, eabc0467, 2021.

Z. Tian, Z. Wang, P. Zhang, T. D. Naquin, J. Mai, Y. Wu, S. Yang, **Y. Gu**, H. Bachman, Y. Liang, Z. Yu, and T. J. Huang, "Generating multifunctional acoustic tweezers in petri dishes for contactless, precise manipulation of bioparticles", *Science Advances*, Vol. 6, No. 37, eabb0494, 2020.

P. Zhang, C. Chen, X. Su, J. Mai, **Y. Gu**, Z. Tian, H. Zhu, Z. Zhong, H. Fu, S. Yang, K. Chakrabarty, and T. J. Huang, "Acoustic streaming vortices enable contactless, digital control of droplets", *Science Advances*, Vol 6, No. 24, eaba0606, 2020.

Y. Gu, C. Chen, J. Rufo, C. Shen, Z. Wang, P. H. Huang, H. Fu, P. Zhang, S. A. Cummer, Z. Tian, and T. J. Huang, "Acoustofluidic holography for micro- to nano- scale particle manipulation", *ACS Nano*, Vol. 14, pp. 14635-14645, 2020.

S. Zhao, M. Wu, S. Yang, Y. Wu, **Y. Gu**, C. Chen, J. Ye, Z. Xie, Z. Tian, H. Bachman, P. H. Huang, J. Xia, S. P. Zhang, H. Zhang, and T. J. Huang, "A disposable acoustofluidic chip

for nano/micro particle separation using unidirectional acoustic transducers", *Lab on a Chip*, Vol 20, pp. 1298-1308, 2020.

H. Bachman, **Y. Gu**, J. Rufo, S. Yang, Z. Tian, P. H. Huang, L. Yu, and T. J. Huang, "Low-frequency flexural wave based microparticle manipulation", *Lab on a Chip*, Vol. 20, pp. 1281-1289, 2020.

Z. Tian*, S. Yang*, P. H. Huang, Z. Wang, P. Zhang, **Y. Gu**, H. Bachman, C. Chen, M. Wu, Y. Xie and T. J. Huang, "Wavenumber-spiral acoustic tweezers for dynamic and reconfigurable manipulation of particles and cells", *Science Advances*, Vol. 5, No. 5, eaau6062, 2019.

S. Zhao, W. He, Z. Ma, P. Liu, P. H. Huang, H. Bachman, L. Wang, S. Yang, Z. Tian, Z. Wang, **Y. Gu**, Z. Xie, and T. J. Huang, "On-Chip stool liquefaction via acoustofluidics", *Lab on a Chip*, Vol. 19, pp. 941-947, 2019.

Z. Tian, C. Shen, J. Li, E. Reit, **Y. Gu**, H. Fu, S. A. Cummer, T. J. Huang, "Programmable Acoustic Metasurfaces", *Advanced Functional Materials*, Vol. 29, pp. 1808489, 2019.

P. Zhang, C. Chen, F. Guo, J. Philippec, **Y. Gu**, Z. Tian, H. Bachman, L. Ren, S. Yang, Z. Zhong, P. H. Huang, N. Katsanis, K. Chakrabarty, and T. J. Huang, "Contactless, programmable acoustofluidic manipulation of objects on water", *Lab on a Chip*, Vol. 19, pp. 3397-3404, 2019.

Y. Gu, C. Chen, Z. Wang, P. H. Huang, H. Fu, L. Wang, M. Wu, Y. Chen, T. Gao, J. Gong, J. Kwun, G. M. Arepally, and T. J. Huang, "Plastic-based acoustofluidic devices for high-throughput, biocompatible platelet separation", *Lab on a Chip*, Vol. 19, pp. 394-402, 2019.

A. Ozcelik, J. Rufo, F. Guo, **Y. Gu**, P. Li, J. Lata, and T. J. Huang, "Acoustic tweezers for the life sciences", *Nature Methods*, Vol. 15, pp. 1021-1028, 2018.

C. Chen, S. P. Zhang, Z. Mao, N. Nama, **Y. Gu**, P. H. Huang, Y. Jing, X. Guo, F. Costanzo and T. J. Huang, "Three-dimensional numerical simulation and experimental investigation of boundary-driven streaming in surface acoustic wave microfluidics", *Lab on a Chip*, Vol. 18, pp. 3645-3654, 2018.

S. Liu, J. Wu, **Y. Gu**, X. Guo, J. Tu, D. Xu, and D. Zhang, "Ambient pressure evaluation through sub-harmonic response of chirp-sonicated microbubbles", *Ultrasound in medicine & biology*, Vol. 43, pp. 332-340, 2017.

C. Chen, **Y. Gu**, J. Tu, X. Guo, and D. Zhang, "Microbubble oscillating in a microvessel filled with viscous fluid: A finite element modeling study", *Ultrasonics*, Vol. 66, pp. 54-64, 2016.

Y. Gu, C. Chen, J. Tu, X. Guo, H. Wu, and D. Zhang, "Harmonic responses and cavitation activity of encapsulated microbubbles coupled with magnetic nanoparticles", *Ultrasonics Sonochemistry*, Vol. 29, pp. 309-316, 2016.